Efficiency and Performance Analysis of AC and DC Grid Based Wind Farms Connected to a High Voltage DC Transmission Line

Jonathan Robinson

B.A.Sc Electrical Engineering, University of Waterloo, Canada

Department of Electrical & Computer Engineering
McGill University
Montréal, Canada

January 2010

A thesis submitted to McGill University in partial fulfillment of the requirements for the degree of Master of Engineering.

Abstract

A trans-Canadian grid could lead to increased ability to integrate wind energy by increasing capacity, improving reliability, and reducing effects of non-dispatchable generation by integrating renewable energy sources over a wide geographical area. Use of HVDC technology in the trans-Canadian grid would result in lower losses for the long transmission lines required and also would provide other benefits, such as lower right-of-way requirements, high reliability, and fault isolation. However, there are no current installations connecting a tapped connection to an HVDC line; all HVDC lines are operated using two terminals. This thesis proposes two methods of connecting a wind farm to an HVDC line. Techniques using an AC grid based wind farm and a DC grid based wind farm are analyzed based on their efficiency and component requirements, as well as their ability to operate during normal and fault conditions. The advantages and disadvantages of both solutions are compared, and while the best overall efficiency can be obtained using an AC system, high efficiencies can also be obtained for the DC system when combined with wind turbines with a MV output voltage. Preliminary simulation analysis shows that the DC grid design provides superior isolation of the HVDC line from faults on the wind farm grid, but both the AC and DC grids have potential issues implementing fault ride through, depending on the location of the fault.

Résumé

Un réseau trans-canadien peut aider à intégrer l'énergie éolienne, qui s'étend sur une vaste zone géographique, en augmentant la capacité de transfert de puissance des lignes de transport et en réduisant les effets non-contrôlables des sources d'énergie renouvelable. L'utilisation de la technologie 'HVDC' peut réduire les coûts des longues lignes de transmission et aussi offrir d'autres avantages comme la réduction de l'empreinte géographique, une meilleure fiabilité, et la localisation des défauts. Toutefois, il n'y a pas de raccordements multi-terminaux HVDC en opération. Cette thèse propose deux méthodes de connexion d'un parc éolien à une ligne HVDC, utilisant des réseaux c.a. et c.c. Le rendement, les composantes requises et la performance transitoire des deux méthodes de connexion sont présentés. Une meilleure efficacité peut être obtenue avec le réseau c.a., mais en intégrant les éoliennes MT, l'efficacité du réseau c.c. est améliorée. Des études préliminaires démontrent que le réseau c.c. aide à une meilleure isolation d'un court-circuit dans le parc éolien qui pourrait se transmettre aux lignes HVDC. Les deux réseaux sont capables de réduire les effets d'un court-circuit, mais peuvent avoir des problèmes à demeurer en service sans déclenchement pour un défaut transitoire.

Acknowledgments

I would like to acknowledge the contributions of my supervisor Prof. Géza Joós, Profs. Dragan Jovcic and Boon-Teck Ooi, and graduate students Ali Jahanbani, Amir Kalantari, Bassam Frem, Carlos Martinez, Catalina Gomez-Quilles, Chad Abbey, Hamed Golestani Far, Hugo Gil, Jean Morneau, Jose Restrepo, Kelvin Lee, Michael Ross, Mohamed El Chehaly, Mustafa Momen, Quanrui Hao, Rodrigo Hidalgo, Sameh El Khatib, Wei Li, and Yongzheng Zhang.

TABLE OF CONTENTS

CHAPTER 1: INTRODUCTION

Canadian wind energy capacity grew by 25% in 2007 and further growth is expected in the future. Wind energy, along with other renewable technologies such as solar and marine energy, is non-dispatchable and high penetrations could reduce the reliability of the provincial electricity grids, leading to local power quality problems and increasing the risk of a cascading blackout. The construction of a Trans-Canadian grid has been proposed as a method to overcome some of the technical challenges associated with generation from renewable energy sources. In addition to possible benefits such as increased reliability and reduced capital and operational costs, a Trans-Canadian grid could be used to integrate wind generation over a large geographical area and help to reduce the effects of wind fluctuations.

HVDC will be considered for the Trans-Canadian grid since it has lower transmission losses, requires less right-of-way, and has been used successfully for long transmission projects in Manitoba and Québec. One issue with using HVDC is the difficulty in operating multi-terminal lines, as only two have been constructed and both are only operated as two-terminal lines. There are no current installations of a tapped terminal on an HVDC line, which could make it difficult to connect a remote wind farm that is not located near a line end terminal. The design of a tap to connect a wind farm to an HVDC line must be economic, operate efficiently and reliably, should allow fast reconnection of the wind farm after transient faults on the HVDC line, and should not allow faults in the wind farm to propagate to the HVDC line where they would cause a major disturbance.

This thesis considers a number of types of converters that could be used to connect a large wind farm to an HVDC grid and proposes two designs:

1. An AC grid based wind farm connected to the HVDC line using a Voltage-Source Converter (VSC) HVDC converter.
2. A DC grid based wind farm connected to the HVDC line using resonant DC-DC converters.

AC and DC grid designs are compared on the basis of their estimated efficiency, component requirements, and their performance during normal wind conditions and faults.

1.1 Wind Farm Technology

The power engineering technology aspects of wind farm integration are related to energy conversion, energy collection and transmission, and grid integration.

Figure 1: Power engineering related areas in wind energy technology.

Research areas related to wind energy conversion include:

- *Generator design*—common generator types include induction generators, synchronous generators, permanent magnet synchronous generators (PMSG), and doubly-fed induction generators/doubly fed asynchronous generators (DFIG/DFAG). Both fixed speed and variable speed generator designs have been installed, and the rotor speed can vary depending on whether a gearbox is used and the size of the gearbox. The generators generally operate at voltages less than 1000 V, although some have been built to operate at MV levels to reduce losses [1].
- *Power converter design*—generators may be designed to operate at the grid frequency and be directly connected, connected through a full power converter, or using a smaller power converter to control the rotor excitation (for a DFIG). Converter designs include two and three-level, as well as multi-module designs [2,3].

Research areas related to energy collection include:

- *High order harmonics*—low order harmonics can be eliminated using selected harmonic elimination and higher switching frequencies.
- *Wind farm grids*—generators operating at LV levels often include a transformer at the base of the turbine to increase the voltage to MV levels before connecting to a common collection bus. All current collection methods use an AC grid, although use

of a DC grid has been proposed and may have some advantages for offshore wind farms (see Section 1.2.4). Studies of offshore AC grid designs include [4,5].

- *Transmission voltage*—if the wind farm is installed in a remote location or offshore, then the power may need to be connected to an HV transmission line, using either a HV AC transformer, or a HVDC converter. Studies of connecting offshore wind using HVDC analyze frequency control, fault ride through, and control during varying wind conditions (more details on HVDC technology is given in Section 1.2).

Research areas related to grid integration are generally based on local grid code requirements. These include:

- *High order harmonics*—low order harmonics can be eliminated using selected harmonic elimination and higher switching frequencies.
- *Power quality*—this includes restrictions on harmonics and flicker. Power quality measurement for wind turbines is outlined in IEC 61400-21: *Measurement and assessment of power quality characteristics of grid connected wind turbines*.
- *Reducing effects of wind variability*—methods of improving integration of non-dispatchable sources of generation include changes to market planning strategies and demand side management, improved forecasting, wind curtailment, and energy storage [6].
- *Unintentional islanding*—a grid operation or grid fault could lead to unintentional islanding of the wind farm, possibly leading to safety or electrical problems. Various methods to detect islanding are currently available [7].
- *Low Voltage Ride Through (LVRT)*—many utilities require LVRT protection to limit the number of wind turbines tripping during grid side faults [8].

1.2 HVDC Status

HVDC technology offers a number of major advantages for a Trans-Canadian grid, including [9,10]:

- *Isolation*—HVDC will isolate the areas that are connected by it, preventing faults from propagating. This was apparent in Québec during the August 2003 blackout, where power was maintained despite a cascading blackout that resulted in the loss of power to neighbouring states and provinces. Any Trans-Canadian grid will need to include some HVDC connections to maintain the existing isolation between the West and East, and Québec.

- *Low line losses*—HVDC has typically been installed in situations with long lines where savings from lower line losses will overcome the high costs of the converters. This advantage is important given the distances required in a Trans-Canadian grid.
- *Power capacity*—HVDC allows higher power capacity, especially for very long lines. This can be seen in Figure 2, where two 3000 MW HVDC lines connecting the Three Gorges Hydroelectric Power Plant in China would have required over three times as much space if HVAC lines of an equivalent voltage were used.

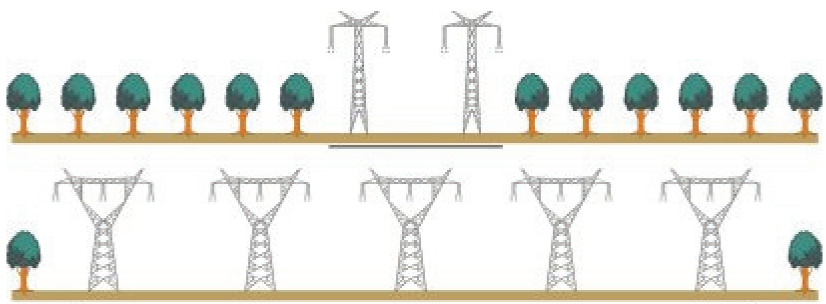

Figure 2: Right-of-way requirement comparison for 500 kV HVDC and 500 kV AC (source ABB)

The two HVDC technologies currently available are VSC HVDC which uses forced commutated IGBTs and Line Commutated Converter (LCC) HVDC which uses self-commutated thyristors. Most studies related to the use of these technologies for wind connections have been for connecting offshore wind farms [11-14], where long cables and high power necessitate the use of HVDC.

1.2.1 Line Commutated Converter HVDC

LCC HVDC technology has been used for many years and has low converter losses (estimated at around 0.8% [9]) and high power rating (up to 6 GW at 800 kV has been proposed). The most common technology uses two six-pulse bridges connected to the AC grid through separate transformers that are displaced by 30°. This allows a reduction in the harmonics produced by the converter (5th and 7th harmonics on the AC side and the 6th harmonic on the DC side [10]).

Issues with the use of LCC HVDC for wind farm applications include:

- *Harmonics*—LCC HVDC converters injects 11th, 13th, 23rd, and 25th harmonics, which are lower frequencies than those produced by VSC HVDC converters (ABB's HVDC Light only requires filters of the 32nd and 60th harmonics).
- *Reactive power support*—the converters consume reactive power during rectification and inversion, which can exceed 60% of the active power of the converter. The reactive power varies depending on the active power and therefore an adjustable power factor correction system is required [9].
- *Weak grid connections*—a weak grid voltage could lead to commutation failure in the thyristors of the converter, resulting in a large disturbance of the DC line. It is recommended that the grid short circuit capability be at least twice the converter rating [10].
- *Cable stress*—a polarity reversal can put significantly more stress on the cable insulation (if underground or undersea cabling is required). During overvoltage situations, the cable dielectric can accumulate a significant amount of space-charge, leading to breakdown if the polarity is reversed. The decay time of the charge will depend on the insulation and is longer for polymeric insulation such as XLPE [15].
- *Transformer reliability*—the transformer for LCC HVDC must be capable of withstanding normal stress from the grid and additional harmonics and insulation stress from the operation LCC HVDC converter [16]. This can result in lower transformer reliability.

Other general issues include the impact of transient and permanent outages of very large power blocks on the AC system, and insulation levels and pollution [17].

1.2.2 Voltage Source Converter HVDC

VSC HVDC uses forced commutated switches and has the following advantages over LCC HVDC that relate to wind applications:

- *Active and reactive power control*—the fast and flexibility control of VSC HVDC allows the converter to provide more support during faults or other transient conditions. The reactive power range will be limited by the voltage rating of the switch [10].

- *Smaller filter and space requirements*—use of pulse-width modulation (PWM) only generates high order harmonics which can be easily filtered. This reduces the cost and size of the filters, and therefore the converter station will require a smaller area (which is especially advantageous for offshore installations).
- *Connection to weak networks and blackstarts*—since the force commutated switches do not require an AC voltage for commutation then VSC converters can connect to weak networks or even passive systems that have no external power source. This can be important when connected to a wind farm that requires external excitation.
- *Power reversal does not change the voltage polarity*—this can lead to an easier implementation of multi-terminal HVDC and smaller cable requirements, allowing use of solid XLPE insulated cables [4]. Current XLPE cables are usually rated for less than 300 kV, although higher ratings are under development [15,18].

Although the maximum power rating of current VSC HVDC technology is less than LCC HVDC, recent advances in switch design will allow power ratings of around 1000 MW [19,20]. The main commercial technologies are ABB's HVDC LIGHT, which uses 2 or 3-level converters and pulse width modulation (PWM) control, and Siemens HVDC PLUS, which uses a multi-module converter. Characteristics of PWM based designs include:

- *Higher switching losses*—these can vary from 1-5% depending on the switching frequency and the type of switches [9].
- *High order harmonics*—low order harmonics can be eliminated using selected harmonic elimination and higher switching frequencies.
- *Loss of control during DC faults*—DC faults effectively short circuit the AC terminals through the free-wheeling diode and also short circuit the DC capacitors. The current into the converter cannot be controlled by the switches and the free-wheeling diodes could be damaged by the fault current [21]. Protecting the converter switches may even require the use of fuses [9]. At this time, VSC HVDC has been used mostly in cable installations, where any fault on the system is likely to be permanent.

The multi-module technology employed by Siemens has the potential to solve some of the difficulties with the 2 and 3-level converters. The design proposed in [21,23,22] is shown in Figure 3.

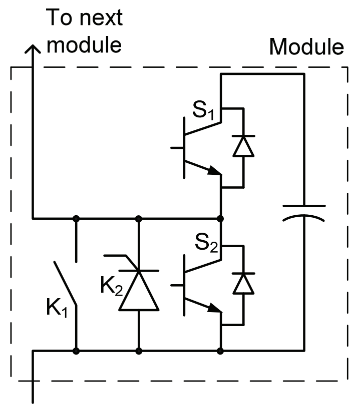

Figure 3: Multi-module converter module

The charge on the capacitor is controlled by two IGBTs for each module. During a DC fault, the thyristor K_2 is switched on to limit the current through the free wheeling diode of the IGBTs. The fault will be finally cleared by operation of an AC circuit breaker. The protective switch K_1 in Figure 3 will allow isolation of the module in case of a failure. In addition, series inductances could be added to limit the AC current during a DC fault [22]. With this multi-module design, switching losses should also be reduced since the operating frequency is around 3x the fundamental frequency.

Other research areas related to VSC HVDC and the Trans-Canadian grid include:

- *Parallel connections of VSC HVDC and HVAC*—construction of a Trans-Canadian HVDC grid will result in areas that have parallel HVDC and HVAC lines and study of control strategies to maximize the stability benefits are required. Similar studies for LCC HVDC have been performed in [24,25].
- *Blackout prevention*—VSC HVDC has been proposed for use in increasing grid segmentation and preventing cascading outages [26].
- *Hybrid VSC/LCC HVDC*—hybrid HVDC converters combine LCC and VSC converters to achieve the benefits from both technologies. These can be combined in parallel or series combinations [12,27].

1.2.3 Multi-terminal HVDC

Multi-terminal lines have been proposed for both LCC and VSC HVDC lines, as well as hybrid lines using both technologies [28-30].

Multi-terminal lines using conventional LCC HVDC technology have the following challenges:

- changing the power flow direction requires the HVDC line to change polarity,
- HVDC circuit breakers are difficult to construct to be able to isolate faults on the system.

Although LCC based multi-terminal lines have been constructed in Italy and New England, they do not operate as multi-terminal lines.

At present there are no VSC multi-terminal HVDC installations although there have been a number of applications that have been proposed. These include:

- *Urban systems* [29]—the paper tests various fault situations but the main advantage noted is an improvement to the power quality.
- *Premium quality power park*—use of a multi-terminal VSC HVDC network to connect industrial companies and users with sensitive loads. This type of grid could eliminate voltage dips and swells, transients, harmonics, flicker, voltage unbalance, and frequency deviation [31].
- *Offshore wind farms*—since offshore wind farms may use long undersea cables, HVDC may be required to avoid the capacitive effects associated with AC cables. Currently the only VSC HVDC wind farm connection installed is a 7.2 MW VSC HVDC line operating in parallel with an AC feeder which connects a 6 MW wind farm in Western Denmark. The first offshore wind farm to be connected by a VSC HVDC line will be located off the coast of Germany using ABB's HVDC Light technology and is expected to be completed in 2009. The wind farm will consist of 80x5 MW wind turbines and will be connected to the grid using two 195 km DC cables rated at ±150 kV [32].

Areas that have been researched include:

- *Isolating multi-terminal HVDC faults*—[33] describes a method of isolating the fault and reclosing the healthy lines without communication.
- *DC overvoltage control* [34]—loss of a converter could lead to an overvoltage on the DC bus if it was in inverting mode. It is proposed that simultaneous response from the

healthy converters decrease the DC voltage to prevent exceeding the rating of the switches. There may be some issues with the response time since the converters are required to respond in less than 3 ms.

- *Multi-terminal VSC models for power flow analysis*—two mathematical models of a VSC HVDC line are derived and power flow is simulated for different control strategies and different systems [35]. In this paper the models and results are only compared in terms of the number of iterations in order to converge.

Other research areas include:

- *Hybrid multi-terminal line with tapped connections*—tapped connections on multi-terminal lines would allow remote load and generation sources to be able to connect to the HVDC line.
- *HVDC breakers*—currently most HVDC lines are tripped with AC breakers outside the converters; however HVDC breakers would allow faster fault isolation and increase system reliability.

1.2.4 High Power DC-DC Converters

DC-DC converters have been studied for connecting solar energy, energy storage systems, and lower powered wind turbines [36,37]; however, the use of high power DC-DC converters in higher power applications, such as in a large wind farm, requires further research. DC based wind farm designs have shown the potential to reduce costs and losses for offshore wind farms, depending on the efficiency of the converter and size of the wind farm [38]. Designs that have been studied for wind applications include multiple boost converters, full-bridge single active bridge converters with a high frequency transformer, and series and parallel resonant converters [39-41]. A boost converter combined with a full bridge converter was used in [42], where the boost converter was used to adjust the voltage and the full bridge converter to transform the voltage (but could not control the transferred power). Disadvantages of this topology include the complexity of the two converters, efficiency for varying power output, and some problems isolating faults.

In order for this concept to succeed, the DC-DC converter must be able to transform the voltage as efficiently as possible (from Section 3.2 it is calculated that an AC transformer operates at over 99% efficiency). Many DC-DC converters have low efficiencies when operated at high powers and high voltage gains. Detailed analysis of the efficiency of three different converters (a single active bridge, a full bridge, and a series-parallel resonant converter) was performed in [40], where converter losses were calculated to be 2-4%. The wind farm considered in [40] is rated for 25 MW and connected to a line rated for 75 kV.

A possible converter that has been proposed for MW size DC-DC converter applications and may be suitable for a wind farm was proposed in [43,44]. This converter is similar to a parallel loaded resonant converter, but the resonant inductors are located on the LV and HV DC sides of the converter (for a bi-directional converter). This topology has a number of advantages over the parallel resonant converter (compared in Appendix C.2). In order to determine the suitability of this converter in wind applications, a detailed analysis of the efficiency and design of this converter is developed in Section 4.1. In addition, a 3-phase variation of this design for minimizing switching losses in high powered applications is studied in Section 4.2. The overall performance of the single phase converter used in a DC grid application for a tapped connection of a wind farm to an HVDC line is studied in Chapter 5 and compared to an AC grid application using 3-level VSC converters.

1.3 Thesis Contributions

This thesis proposes DC and AC grid based methods of connecting a wind farm to an HVDC line. Different voltage source converters and DC-DC converters are compared based on the efficiency, component requirements and performance during normal operation and faults.

The main contributions of this thesis are:

(a) *Efficiency calculations of an AC based wind farm grid*—detailed calculations of the losses in the 3-level NPC converter switches and transformers are derived. This can be used to optimize the component selection to minimize costs over the wind farm lifetime.

(b) *Development of a 3-phase resonant converter*—a 3-phase resonant converter is proposed to reduce switching losses. The main equations for modelling the converter are derived and a design procedure is developed for component selection based on the system requirements and loss minimization.

(c) *Efficiency calculations of DC-DC resonant converters*—detailed calculations of the switch losses and passive component losses are derived for both the single phase and 3-

phase resonant converters. This information is used to help optimize the design procedures of both converters.

(d) *DC-DC converter model and controller design for a DC grid based wind farm*—a simplified converter model and controller design is proposed for the DC-DC converters that minimizes the effects of faults in the wind farm grid or HVDC line. Preliminary simulation analysis is performed for various faults.

(e) *Comparison of efficiency and cost analysis for amorphous core and silicon steel core transformers for wind applications*—amorphous cores have been used successfully in distribution applications and the cost benefits for wind turbine applications are shown.

1.4 Thesis Outline

Chapter 2 overviews the wind farm design components related to connecting a wind farm to an HVDC line. A description is given of the wind turbine generator that is used for both the AC and DC based grid models.

Chapter 3 details the design of an AC grid using 2 and 3-level voltage source converters. The converter efficiency and the overall AC system efficiency are calculated, and component requirements are determined for different MV grid voltage levels. Detailed information on the efficiency calculations and magnetic component design is in Appendices A and B.

Chapter 4 details the design of a DC grid using single and 3-phase resonant converters. The efficiency and component requirements are determined for different MV DC grid voltage levels. A comparison of DC and AC cable requirements in a wind farm is shown. Detailed derivations of the resonant converter designs are given in Appendices C and D.

Chapter 5 outlines the integration issues and control requirements of the converters, and shows the performance of an AC grid and DC grid under normal wind conditions and during faults. Preliminary analysis of methods of reducing the effects of faults is developed.

Chapter 6 summarizes and compares the AC and DC grid designs based on the efficiency, component requirements, and performance and integration issues.

Chapter 7 summarizes the thesis, lists the major conclusions, and reviews areas of future research.

CHAPTER 2: WIND FARM DESIGN OVERVIEW

Design areas for a tap connection of a wind farm to an HVDC line include:

- the type of wind turbine generator,
- the connection between the individual turbines and a MV grid,
- the design of the MV grid,
- the connection between the MV grid and the HVDC line.

2.1 Wind Turbine Generator Type

There are currently a number of different types of wind turbine generator topologies, each having different advantages and disadvantages. Comparisons of different topologies based on cost, efficiency, and structural factors (size, weight, robustness) can be found in [45].

Many potential Canadian wind farms locations are in remote areas where access may be difficult and environmental conditions are extreme. This thesis considers the use of variable speed synchronous generators that will interface to the grid using full converters. Advantages of this type of generator topology include:

- *Better reactive power capability*—the full converter allows decoupled control of the active and reactive power, allowing the wind turbine to help support the grid voltage or vary the reactive power as required.

- *Reduced size gearbox*—in many wind turbine designs, the gearbox is often a source of maintenance problems and noise. The Areva Multibrid M5000, GE 2.5XL, and Gamesa G10x use permanent magnet synchronous generators (PMSG) that have a gearbox to operate at medium generator shaft speeds. Manufacturers that use direct drive generators that allow them to eliminate the gearbox entirely include Vensys and Siemens, which use direct drive PMSGs, and Enercon, which uses separately excited salient pole synchronous generators [46].

- *Large power output*—many of the high power wind turbines use synchronous machines. The largest installation is by Enercon, which has built a wind turbine that exceeds 6 MW power output.

- *Converter power control*—meeting grid requirements such as LVRT and power quality requirements can be easier due to the control flexibility offered by the full power converter.

- *Slow generator rotation*—although this will result in a larger and heavier generator construction (with increased copper due to higher numbers of poles and increased core sizing to prevent overexcitation), the slower generator rotation could help increase the reliability. A comparison of generator rotations of an Enercon E-70 2.3 MW direct drive wind turbine with conventional induction generator based turbine is shown in Figure 4.

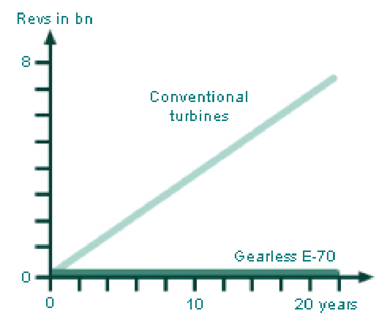

Figure 4: Comparison of generator rotations over the wind turbine lifetime (Source: Enercon).

- *High efficiency at wide power range*—this topology allows a wide speed range that improves the overall electrical yield [1].

The disadvantages of synchronous generators include a more complex and costly generator design, larger size and weight, installation difficulties due to the large size of the nacelle, and the cost of a full power converter.

2.1.1 Synchronous Generator Characteristics

The synchronous generator will convert energy from the mechanical rotation of the wind turbine into electrical energy. The rms armature voltage of a synchronous machine is:

$$E_a = \sqrt{2}\pi K_w f N_a \Phi_p \tag{1}$$

where K_w is a machine constant, f is the frequency (in Hz), N_a is the number of turns in an armature phase, and Φ_p is the magnetic flux, given by:

$$\Phi_p = 2Blr \tag{2}$$

where B is the flux density of the magnetic field, r is the radius of the stator coil and l is the coil length. For externally excited synchronous machines, the flux density will be given by:

$$B = \frac{2\mu_0 N_f I_f}{\pi g} \tag{3}$$

where N_f is the number of turns of a field pole, I_f is the field current, and g is the air gap length. For a PMSG, the magnetic flux will be constant and therefore the flux will be [47]:

$$\Phi_{PM} = 2B_{g1}l_e r_s \tag{4}$$

where B_{g1} is the fundamental harmonic of the air-gap flux density due to the magnets, L_e is the equivalent core length, and r_s is the stator radius. The output voltage of the stator (V_s) can be obtained from an equivalent circuit of the synchronous generator, shown in Figure 5.

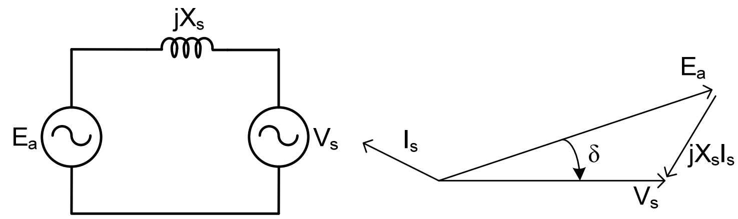

Figure 5: Synchronous generator equivalent circuit.

In Figure 5, the vector diagram shows the generator with an overexcited field winding and leading power factor. If the field winding is underexcited then the stator current will be in the fourth quadrant and the power factor will be lagging. The armature resistance is assumed to be small. From Figure 5, the stator voltage is given by:

$$V_s = E_a + jX_s I_s \tag{5}$$

With a PMSG, the flux from the field winding is fixed and therefore the armature voltage (E_a) will depend on the rotational frequency of the wind turbine. In a separately excited synchronous generator then E_a is also dependent on the current in the field winding (I_f).

The generator efficiency depends on losses in the stator winding, stator core, rotor core, as well as eddy currents and rotational losses.

2.1.2 Generator Control

The control for a synchronous generator based wind turbine has the following objectives:

1. Maximize the power output for various wind speeds.
2. Maintain the operation within rated current, voltage, and V/Hz.

When the turbine is above the rated speed then the wind turbine speed is normally fixed by adjusting the blade pitch angle. At speeds below the rated speed, the maximum power is determined by the characteristics of the blade (described in [48]). The wind power is:

$$P = \frac{1}{2} A \rho C_p v_w^3 \quad (6)$$

where A is the area swept by the blade, ϱ is the air density, C_p is the turbine power coefficient, and v_w is the wind velocity. Operating at the maximum power point requires operating at maximum C_p, which will depend on the blade, the pitch angle, and the ratio of the blade tip speed to the wind speed (λ), given by:

$$\lambda = \frac{\omega R}{v_w} \quad (7)$$

Figure 6 shows the value of C_p for various tip speed ratios using the blade dimensions of a Danwin wind turbine, obtained using an iterative process outlined in [48].

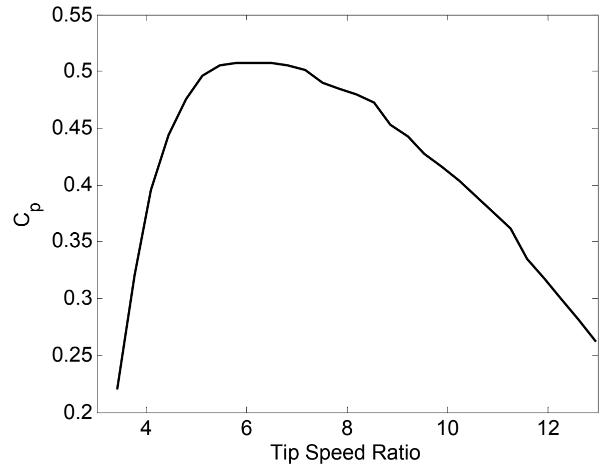

Figure 6: Power coefficient value for various tip speed rations.

Operating at maximum power below rated wind speeds is achieved by controlling the rotor speed depending on the speed of the wind and matching it to a calculated rotor speed (from a lookup table). Smaller adjustments to obtain the optimal power can be performed using a perturb-and-observe (PAO) method similar to that used for solar arrays. This control will depend on the type of rectifier connected to the wind turbine. Possible options for the rectifier include an IGBT based converter, and a diode rectifier and boost converter, shown in Figure 7.

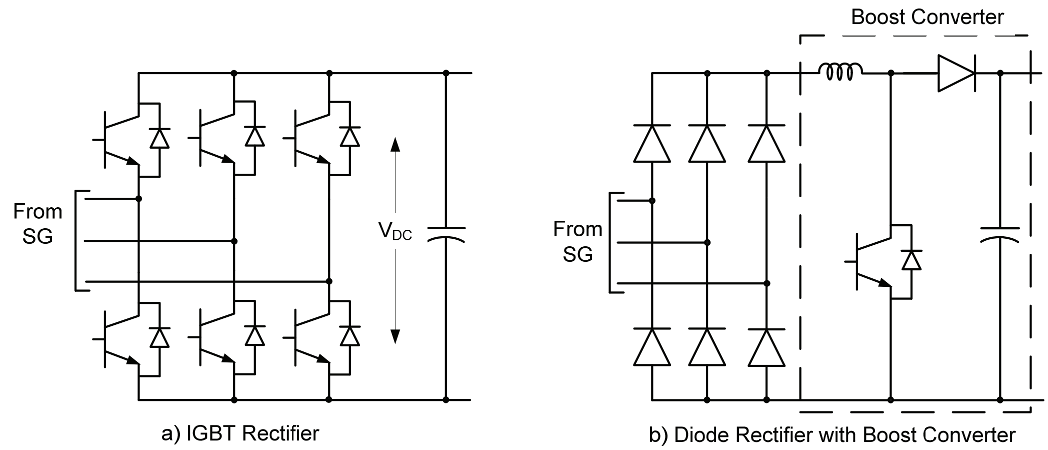

Figure 7: Generator side converter topologies.

In topology (b), the turbine speed can be controlled to maximize the generated power by varying the DC voltage by changing the duty cycle of the boost converter [49]. This topology has been proposed for small scale wind turbines since larger wind turbines would require multiple boost converters, increasing the complexity and number of switches [39]. In addition, the generator efficiency in topology (b) may be reduced due to lack of control of the generator power factor and harmonics from the diode rectifier [50].

Topology (a) offers more flexibility and can be more easily applied to larger turbines. Control strategies for controlling the speed, current, and voltage using decoupled *dq* components are outlined in [50,51]. Unlike in topology (b), in normal operation, the DC voltage will be fixed by controlling the inverter current to match the power injected by the rectifier.

Multilevel converters have also been proposed for wind turbine converters, including the Flying Capacitor (FC) converter and the Neutral Point Clamped (NPC) converter. These converters require increased number of switching elements, but have lower switching losses, allow the converter to operate at lower frequencies, and reduce the size of filter component requirements [52,53].

Filters on the generator side may be required to reduce harmonics from the rectifier that will result in extra losses in the generator windings. DC filters are also required depending on the type of rectifier and control method, and will allow the control of the rectifier and inverter of a full converter to be decoupled. Figure 8 shows the full converter of a PMSG that could connect to an AC grid, showing a PWM based inverter and rectifier and DC capacitor.

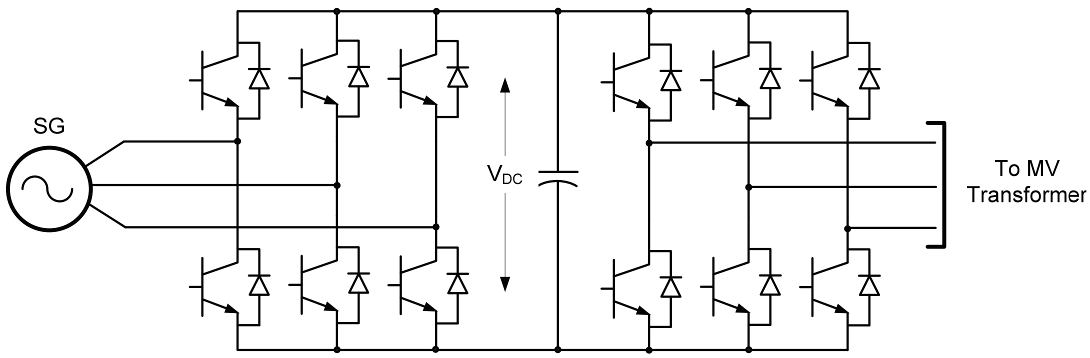

Figure 8: 2-level IGBT converter.

Press-pack IGBT switches are common in VSC HVDC applications due to straightforward series connections, low gate currents, and the ability to conduct after failing [54]. IGBTs can be paralleled to obtain a higher current rating, but should be derated by a derating factor [55]:

$$\delta = 1 - \frac{I_T}{n_p I_m} \tag{8}$$

where I_T is the total current in the paralleled switches, n_p is the number of paralleled switches, and I_m is the maximum current for a single switch.

2.2 Wind Farm Grid Design

Two options will be considered for connecting the wind turbines to the MV grid:

1. *AC Grid Connection*—the full converter will change the voltage from AC-DC and then DC to 60 Hz AC to be transformed and connected to a MV AC grid.

2. *DC Grid Connection*—the full converter will change the voltage to DC and then use a DC-DC converter to increase the voltage to MV DC to be connected to a MV DC grid.

The design requirements of the AC and DC grids are different and will be developed separately in Chapters 3 and 4.

CHAPTER 3: AC GRID DESIGN

Design issues for an AC grid connection of synchronous generator based wind turbines using full converters will depend on the type of inverter, the size and topology of the wind farm, and the local grid and connection regulations (if applicable).

A number of different types of wind farm AC grid topologies have been proposed for connection to an HVDC line [38]. These include:

- *Star connected*—generators are connected to MV transformers at the base of the turbine and then connected together at a MV bus before being connected to a HV transformer and VSC HVDC converter.
- *Cluster connected*—groups of generators are connected together at a lower voltage before transforming the voltage to MV levels and then connecting to a MV bus.
- *MV generator based wind farm*—generators are designed for MV outputs and star connected to a MV bus, thus eliminating the individual MV transformer.
- *Multiple VSC HVDC converters*—use of multiple HVDC converters to connect multiple wind farms or a large spread out wind farm to an HVDC line has been proposed for the connection of offshore wind farms to a multi-terminal HVDC line or offshore HVDC hub.

Single line diagrams of the various wind farm AC grid models are shown in Figure 9.

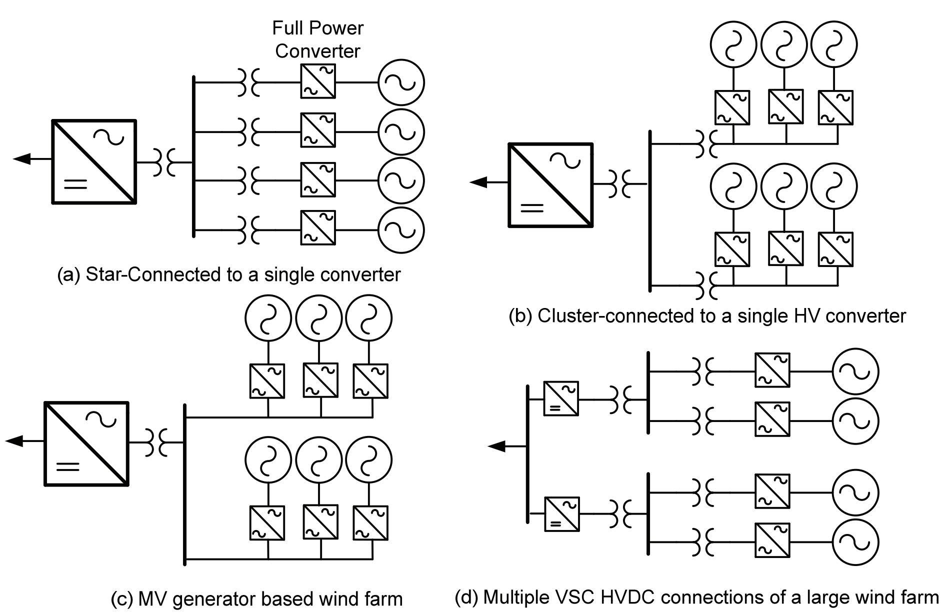

Figure 9: AC grid topologies.

The AC grid that will be studied in this thesis will be based on topology (a). The AC grid will consist of 3 MW PMSGs with a rated 1000 V output, and the total wind farm will consist of 100 turbines. A full power converter will convert the variable generator output to the rated grid frequency and then it will be transformed by the MV transformer to 33 kV. The HV transformer and VSC HVDC converter will connect the entire wind farm to a 500 kV HVDC line.

3.1 Wind Turbine Full Converter

This thesis will not analyze in detail the generator control and therefore the operation of the full converter will be considered decoupled at the DC bus. The focus will be on the design and control of the grid side inverter and the rectifier and therefore the synchronous generator will be modeled by a controllable DC current source, shown in Figure 10.

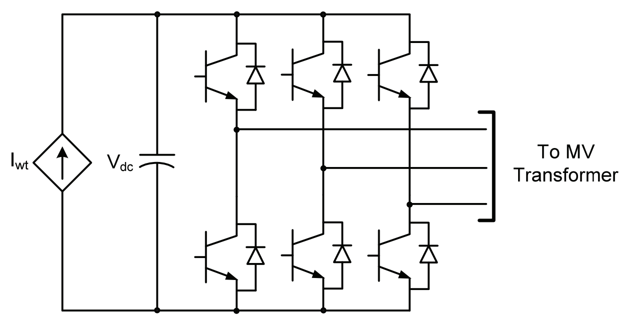

Figure 10: Wind turbine model with a 2-level VSC inverter connected to the AC grid.

The inverter control must be designed to inject the power generated by the wind turbine into the AC grid. Other control requirements may include:

- minimizing AC harmonics,
- low voltage ride through,
- reactive power support (if required),
- possibly other features such as power system stabilizers.

Use of a PWM inverter allows control of the frequency (if injecting into an isolated grid), current control (to prevent the current from exceeding the converter capability), and active and reactive power control. Since the VSC designs (outlined in Section 2.1.2) are already well developed, this analysis will summarize the main features and compare the number of switches (and switch utilization), the switching frequency, and the efficiency of a 2-level inverter and 3-level NPC inverter. Note that some commercial designs use multiple parallel converters as they offer increased redundancy and can reduce losses as some converters can be disabled at low wind speeds.

3.1.1 2-Level Inverter

A 2-level inverter, as shown in Figure 10, will consist of six switching valves, each rated for the voltage of the DC bus, given by:

$$V_{dc} = \frac{2\sqrt{2}V_{LL}}{m\sqrt{3}} \tag{9}$$

where m is the modulation index. Assuming operation in the linear region, then m must be less than 1 and will be assumed to be 0.95 for this design, resulting in a DC voltage of 1720 V_{DC}. The current of the converter will vary depending on the power output of the wind turbine and will have a maximum rms value of 1732 A. If the converter is sized to continue supplying rated power for a voltage dip of 85%, then the converter current should be rated for 2038 A. If the converter is designed for a current of at least 115% of the maximum and 200% of the maximum voltage, then, using ABB 5SNA 2400E170100 type switches will require two series switches per valve. A second design will be compared that uses a MV wind turbine with a rated line-to-line voltage of 4 kV, resulting in a DC voltage of 6880 V.

The voltage across the switch will be equal to the DC voltage, and the current through the switch and reverse recovery diode will be a pulsed sinusoidal waveform (shown in Figure 11).

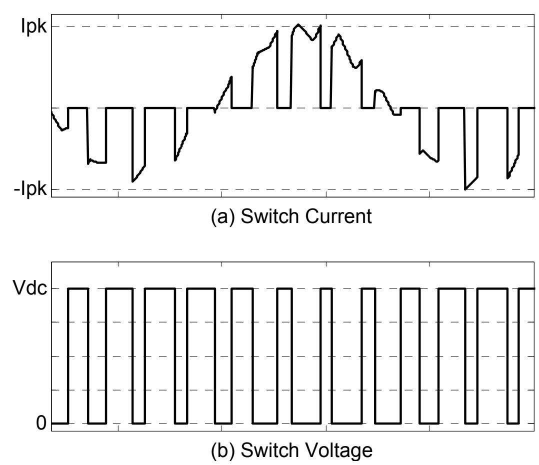

Figure 11: 2-Level inverter switch voltage and current.

Estimating the switching losses using (A16) requires the switching current at each turn-on and turn-off instance. If the switching frequency is high compared to the frequency of the collector current, then the losses can be estimated by finding the average current at each switching instant.

Assuming a sinusoidal current, then the average of the collector current and square of the collector current will be equal to $\pi/2$ and 0.5, respectively. Therefore considering that the losses in the IGBT will only occur during half a cycle (during the other half of the cycle the reverse recovery diode will conduct), the losses per switch will be given by:

$$P_{swIGBT} = 6\frac{V_{DC}}{V_{cc}}\frac{1}{2\pi}\int_0^{\pi}\left(A_{IGBT}I_{pk}^2\sin^2(\alpha)+B_{IGBT}I_{pk}\sin(\alpha)+C_{IGBT}\right)d\alpha\cdot 2f_s$$
$$= 6\frac{V_{DC}}{V_{cc}}\left(A_{IGBT}\frac{I_{pk}^2}{2}+B_{IGBT}\frac{2I_{pk}}{\pi}+C_{IGBT}\right)f_s \tag{10}$$

where V_{cc} is the switch voltage at which the datasheet loss parameters are specified, and losses are multiplied by 6 for the six valves. The parameters A_{IGBT}, B_{IGBT}, and C_{IGBT} are specific to the type of IGBT and are given on the datasheet (see Appendix A.2). The losses are calculated by integrating over half a cycle, $0<t<\frac{1}{2f_g}$ where f_g is the ac grid frequency. To simplify the analysis, a change of variables is used so that it is integrated from $0<\alpha<\pi$, where α is equal to $2\pi f_g t$,. Similarly using (A17), reverse recovery losses in the diode will by given by:

$$P_{rr} = 6\frac{1}{2}\frac{V_{DC}}{V_{cc}}\left(A_D\frac{I_{pk}^2}{2}+B_D\frac{2I_{pk}}{\pi}+C_D\right)f_s \tag{11}$$

The conduction losses will depend on the modulation waveform. Assuming sinusoidal PWM, then the modulation waveform will be a sinusoidal waveform depending on the modulation index and the angle between the current and the voltage. Taking the average over one cycle and using (A11) and (A12), then the conduction losses in the IGBT are [56]:

$$P_{onIGBT} = 6n\frac{1}{2\pi}\int_0^{\pi}\left[R_{CE}I_{pk}^2\sin^2(\alpha)+V_{T0}I_{pk}\sin(\alpha)\right]\frac{1}{2}\left(1+m\sin(\alpha+\theta)\right)d\alpha$$
$$= 6n\left[\left(\frac{1}{8}+\frac{m}{3\pi}\right)R_{CE}I_{pk}^2+\left(\frac{1}{2\pi}+\frac{m}{8}\cos(\theta)\right)V_{T0}I_{pk}\right] \tag{12}$$

where m is the modulation index and θ is the angle between the current and voltage, n is the number of switches per valve, and the factor $\frac{1}{2}[1+m\sin(\alpha+\theta)]$ is the duty cycle. R_{CE} and V_{T0} can be obtained from the IGBT datasheet (see Appendix A.2). Similarly, the conduction losses in the diode are:

$$P_{onDiode} = 6n\left[\left(\frac{1}{8}-\frac{m}{3\pi}\right)R_{DF}I_{pk}^2+\left(\frac{1}{2\pi}-\frac{m}{8}\cos(\theta)\right)V_{F0}I_{pk}\right] \tag{13}$$

where R_{DF} and V_{FO} can be obtained from the IGBT datasheet (see Appendix A.2). The off-state losses will depend on the cut-off current. Averaging the off-state losses over one cycle, then:

$$P_{off} = 6\frac{1}{2\pi}\int_0^{\pi}\left[V_{DC}\frac{V_{DC}}{nV_{ref}}I_{cutoff}\right]\left[\frac{1}{2}\left(1+m\sin(\alpha+\theta)\right)+\frac{1}{2}\left(1-m\sin(\alpha+\theta)\right)\right]d\alpha$$
$$= 6\frac{1}{2}\frac{V_{DC}^2}{nV_{ref}}I_{cutoff} \tag{14}$$

where V_{ref} can be obtained from the IGBT datasheet. Relevant characteristics of the IGBTs for calculating the losses are listed in Table 1. The 2400E170100 will be used for the 1720 V_{DC} design and the 0750G650300 will be used for the 6880 V_{DC} design.

Table 1: ABB 5SNA 2400E170100 IGBT parameters for calculating losses in a 3 MW VSC.

	2400E170100	0750G650300
Max. collector-emitter voltage	1700 V	6500 V
Max. DC collector current	2400 A	750 A
Series switches per valve	3	3
Total number of switches	18	18
IGBT on-state voltage	V_{T0}= 1.25 V, R_{CE}=0.417 mΩ	V_{T0}= 1.3 V, R_{CE}=4.17 mΩ
Diode on-state voltage	V_{F0}= 1.2, R_{DF}=0.19 mΩ	V_{F0}= 1.75, R_{DF}=1.67 mΩ
IGBT Switching Parameters	A_{IGBT}=1.38x10^{-7}, B_{IGBT}=2.8x10^{-4} C_{IGBT}=0.233, V_{cc}=900 V	A_{IGBT}=5.64x10^{-6}, B_{IGBT}=9.2x10^{-3}, C_{IGBT}=1.65, V_{cc}=3600 V
Diode Switching Parameters	A_D=-4.52x10^{-8}, B_D= 3.82x10^{-4} C_D=0.076, V_{cc}=900 V	A_D=-1.12x10^{-6}, B_D= 3.94x10^{-3}, C_D=375e^{-3} V_{cc}=3600 V
Cut-off current	12 mA (V_{CE}=1700 V)	12 mA (V_{CE}=6500 V)

Note: a detailed explanation of the different parameters is given in Appendix A.2.

The losses of the 1720 V_{DC} and 6880 V_{DC} based designs over the whole operating range of the converter for a converter with a switching frequency of 1980 Hz operating at unity power factor are given in Figure 12.

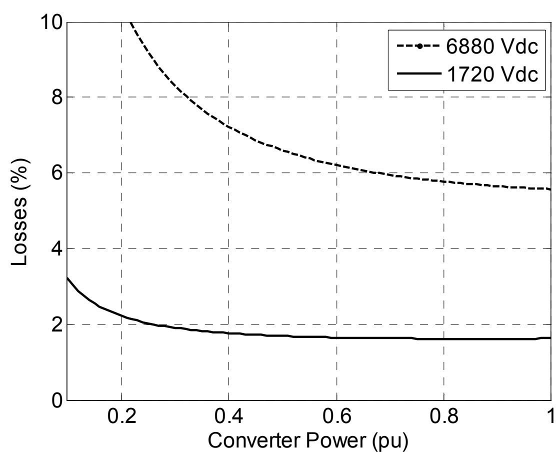

Figure 12: 2-Level converter losses.

It can be seen that the efficiency is much lower for the higher voltage wind turbine design. This is mostly due to higher switching losses in the 0750G650300 IGBTs, as using 2400E170100 IGBTs for the 6880 V_{DC} case will result in losses that are comparable to the

1720 V_{DC} case (although requiring larger switches and resulting in 3x the number of switches). The switch utilization, as defined in [57,58], will be given by:

$$U = \frac{P_{\max}}{\sum_{i=1}^{q_{sw}} I_{sw,i} V_{sw,i}} = \frac{P_{\max}}{q_{sw} I_{sw} V_{sw}} \tag{15}$$

where q_{sw} is the total number of switches (diodes and IGBTs) and I_{sw} and V_{sw} are the peak voltage and rms current. Utilization of the 1720 V and 6880 V cases is 24% at rated power.

It should be noted that if the converter is also used to provide reactive power then the efficiency will decrease, especially at low active power levels. In addition, these losses do not account for losses in other components.

3.1.2 3-Level Inverter

Multi-level converters can achieve a better voltage waveform by allowing intermediate voltage levels. This will allow the converter to operate at lower switching frequencies and still maintain low harmonics. Most designs are limited to 3 levels due to increased number of components and complexity, as well as uneven distribution of the switch losses [59]. The main types of 3-level converters are neutral point clamping (NPC) and flying capacitor (FC) voltage source converters. A variation of the NPC VSC is the Active Neutral point clamping (ANPC) VSC which is designed to reduce the uneven switch loss distribution [60,61]. This section will analyze a 3-phase NPC VSC, shown in Figure 13.

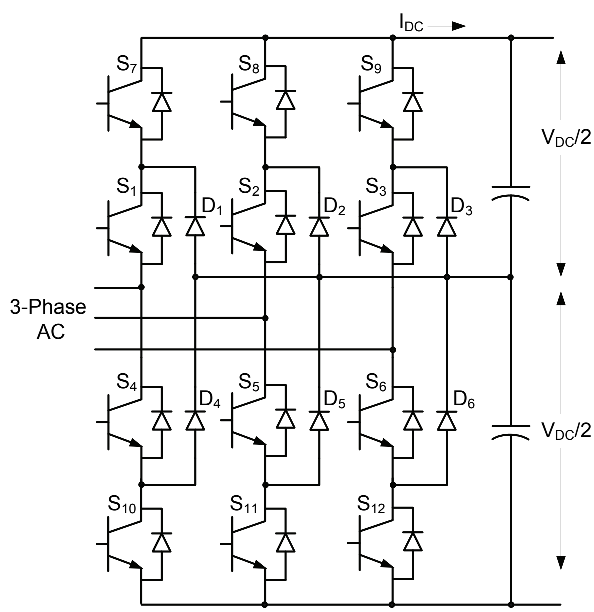

Figure 13: 3-Level neutral point clamping voltage source converter.

The switches and diodes of the NPC VSC must be rated for half the voltage of the converter and for a maximum current equal to the peak current of the converter. Using sinusoidal PWM control, the voltage and current waveforms for the various switches, while operating at unity power factor and operating in rectifier mode, are shown in Figure 14 and Figure 15. Switching characteristics of switches connected to the DC bus (S_7-S_{12}) are in Figure 14(b) and characteristics of switches connected to the AC side (S_1-S_6) are in Figure 14(a).

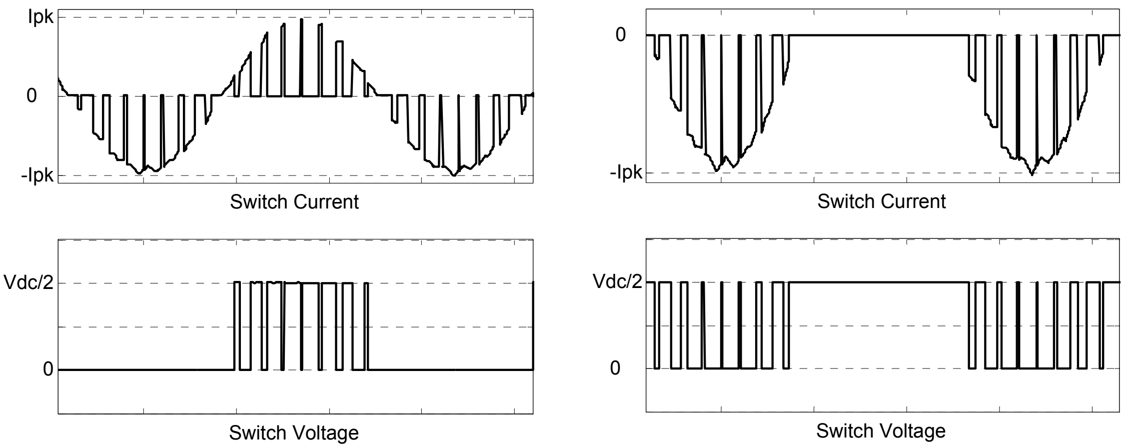

(a) inner switches (S_1-S_6) (b) outer switches (S_7-S_{12})

Figure 14: 3-Level converter switch voltage and current.

From Figure 14(a), the inner set of switches will have conduction losses both through the IGBTs and through the freewheeling diodes. Switching losses will only occur in the IGBTs (when operating in rectifier mode) since switching of the freewheeling diodes will be at zero voltage. In Figure 14(b), it can be seen that current will only flow through the freewheeling diodes, which will have reverse recovery losses. The neutral connected diodes (D_1-D_6) will only experience conduction losses as switching occurs at zero voltage, as shown in Figure 15.

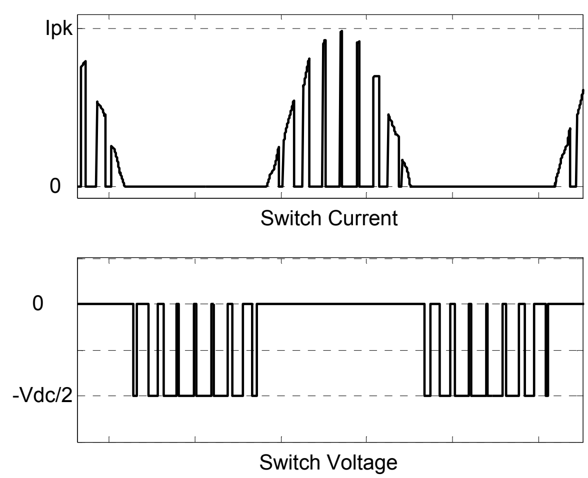

Figure 15: 3-Level converter neutral diode (D_1-D_6) voltage and current.

Although Figure 14 and Figure 15 only show the rectifier mode switching characteristics, other modes will have similar switching losses in each valve (each cycle having one hard switched diode and one hard switched IGBT). The converter losses can be analyzed similar to the 2-level converter in Section 3.1.1. Since the switching voltage across the inner and outer IGBTs will be half the DC voltage, then the switching losses are:

$$\begin{aligned} P_{swIGBT} &= 6\frac{V_{DC}}{2V_{cc}}\frac{1}{2\pi}\int_0^{\pi}\left(A_{IGBT}I_{pk}^2\sin^2(\alpha)+B_{IGBT}I_{pk}\sin(\alpha)+C_{IGBT}\right)d\alpha\cdot 2f_s \\ &= 6\frac{V_{DC}}{2V_{cc}}\left(A_{IGBT}\frac{I_{pk}^2}{2}+B_{IGBT}\frac{2I_{pk}}{\pi}+C_{IGBT}\right)f_s \end{aligned} \tag{16}$$

Similarly, the diode reverse recovery losses will be:

$$P_{rr} = 6\frac{1}{4}\frac{V_{DC}}{V_{cc}}\left(A_D\frac{I_{pk}^2}{2}+B_D\frac{2I_{pk}}{\pi}+C_D\right)f_s \tag{17}$$

The on-state losses in the outer set of IGBTs will be given by:

$$\begin{aligned} P_{onouter} &= \frac{6n}{2\pi}\int_0^{\theta}\left[R_{CE}I_{pk}^2\sin^2(\alpha)+V_{T0}I_{pk}\sin(\alpha)\right]m(1+\sin(\alpha-\theta))d\alpha \\ &= \frac{6nm}{2\pi}\left[\frac{R_{CE}I_{pk}^2}{2}\left(-1+\theta-\frac{1}{2}\sin(2\theta)-\frac{1}{3}\cos(2\theta)+\frac{4}{3}\cos(\theta)\right)+\right. \\ &\qquad \left.+V_{T0}I_{pk}\left(1-\cos(\theta)+\frac{\theta}{2}\cos(\theta)-\frac{1}{2}\sin(\theta)\right)\right] \end{aligned} \tag{18}$$

where θ is the absolute value of the angle between the current in the voltage and n is the number of IGBTs per switch. Similarly, the losses in the inner set of IGBTs will be given by:

$$\begin{aligned} P_{oninner} &= \frac{6n}{2\pi}\left[\int_0^{\theta}\left[R_{CE}I_{pk}^2\sin^2(\alpha)+V_{T0}I_{pk}\sin(\alpha)\right]d\alpha+\right. \\ &\qquad \left.+\int_{\theta}^{\pi}\left[R_{CE}I_{pk}^2\sin^2(\alpha)+V_{T0}I_{pk}\sin(\alpha)\right]m(1-\sin(\alpha-\theta))d\alpha\right] \\ &= \frac{6n}{2\pi}\left[R_{CE}I_{pk}^2\left(\frac{\theta-\cos(\theta)\sin(\theta)}{2}-\frac{m}{2}\left(1-\pi+\theta+\frac{4}{3}\cos(\theta)-\frac{1}{2}\sin(2\theta)+\frac{1}{3}\cos(2\theta)\right)\right)+\right. \\ &\qquad \left.V_{T0}I_{pk}\left((1-\cos(\theta))+m\left(1+\left(1+\frac{\pi}{2}\right)\cos(\theta)-\frac{1}{2}\sin(\theta)+\frac{\theta}{2}\cos(\theta)\right)\right)\right] \end{aligned} \tag{19}$$

Both the inner and outer IGBTs will have similar on-state losses through their freewheeling diodes. The on-state for both the inner and outer freewheeling diodes losses can be calculated using a duty cycle of *m*[sin(α-*θ*)], and are given by:

$$
\begin{aligned}
P_{onFWD} &= 6n\frac{2}{2\pi}\int_{\theta}^{\pi}\left[R_{DF}I_{pk}^{2}\sin^{2}(\alpha)+V_{F0}I_{pk}\sin(\alpha)\right]m(\sin(\alpha-\theta))d\alpha \\
&= \frac{6nm}{2\pi}\left[R_{DF}I_{pk}^{2}\left(1+\frac{1}{3}\cos(2\theta)+\frac{4}{3}\cos(\theta)\right)+V_{F0}I_{pk}(\theta\cos(\theta)-\sin(\theta))\right]
\end{aligned}
\tag{20}
$$

The neutral diodes will have on state losses over half a cycle and will be given by:

$$
\begin{aligned}
P_{on\,DIODE} = \frac{6n}{2\pi}\Bigg[&\int_{0}^{\theta}\left(R_{DF}I_{pk}^{2}\sin^{2}(\alpha)+V_{F0}I_{pk}\sin(\alpha)\right)m(1+\sin(\alpha-\theta))d\alpha + \\
&+\int_{\theta}^{\pi}\left[R_{DF}I_{pk}^{2}\sin^{2}(\alpha)+V_{F0}I_{pk}\sin(\alpha)\right]m(1-\sin(\alpha-\theta))d\alpha\Bigg] \\
= \frac{6nm}{2\pi}\Bigg[&R_{DF}I_{pk}^{2}\left(\frac{1}{2}(\pi-2)-\frac{1}{3}\cos(2\theta)\right)+V_{F0}I_{pk}\left(2+\left(\theta-\frac{\pi}{2}\right)\cos(\theta)-\sin(\theta)\right)\Bigg]
\end{aligned}
\tag{21}
$$

The off-state losses for the inner set of IGBTs will have a duty cycle over half a switching cycle of *m*[sin(α)]. The off-state losses for the outer set of IGBTs will have a duty cycle of *m*[1-sin(α+*θ*)] over half a switching cycle and over the other half of the switching cycle a constant voltage of $1/2V_{DC}$ will be applied across the switch. Using an off-state voltage drop of $\frac{1}{2}V_{DC}$, the losses for both sets of IGBTs will be:

$$
\begin{aligned}
P_{offIGBT} &= 6\frac{1}{2\pi}\int_{0}^{\pi}\left[\frac{V_{DC}}{2}\frac{V_{DC}}{2nV_{ref}}I_{cutoff}\right](1+m\sin(\alpha)+m(1-\sin(\alpha)))d\alpha \\
&= 6\frac{V_{DC}^{2}}{8nV_{ref}}(1+m)I_{cutoff}
\end{aligned}
\tag{22}
$$

Off-state losses in the neutral diodes will be over half a cycle with a duty cycle of *m*[sin(α)]:

$$
\begin{aligned}
P_{offDIODE} &= 6\frac{1}{2\pi}\int_{0}^{\pi}\left[\frac{V_{DC}}{2}\frac{V_{DC}}{2nV_{ref}}I_{cutoff}\right]m(\sin(\alpha))d\alpha \\
&= 6\frac{V_{DC}^{2}}{8nV_{ref}}mI_{cutoff}
\end{aligned}
\tag{23}
$$

Using the IGBT switch data for ABB IGBTs given in Section 3.1.1, the losses for a 3-level converter operating at 1260 Hz are plotted in Figure 16. Both cases will require a total of 24 IGBT switches (4 switches in series per valve).

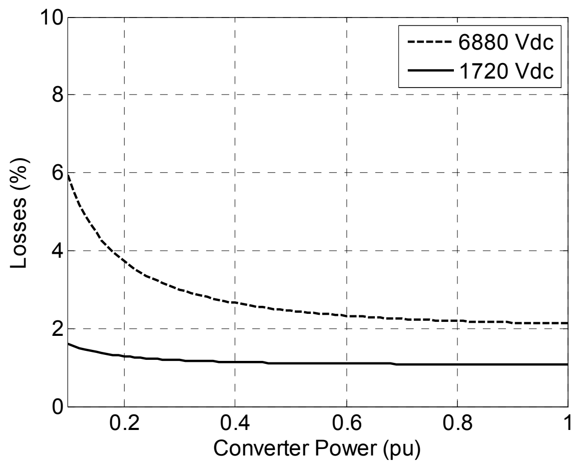

Figure 16: 3-level converter losses.

In comparison with the losses of the 2-level converter shown in Figure 12, it can be seen that the 3-level converter has lower losses at all power levels and shows and improvement of around 0.5-3.5% at rated power (depending on DC voltage level). The disadvantage is a more complex design, higher number of switches, and lower switch utilization (14.4% at rated power).

3.1.3 Filter Design

The filter design should effectively reduce harmonics from the VSC converter, while minimizing the effects on the converter response, resonances, and inrush currents. Methods of evaluating the major harmonics for sinusoidal PWM can be found in [62,63]. The major harmonics for 2-level converters occur at odd harmonics nearest to multiples of the carrier frequency, and harmonics for 3-level converters occur at multiples of the carrier frequency.

LCL based filters have been proposed for VSC applications as they can be designed to minimize the component size while also reducing inrush current problems with an LC filter. An LCL filter with a damping resistance is shown in Figure 17.

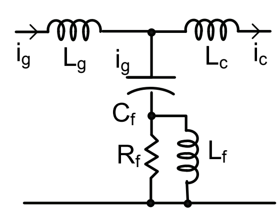

Figure 17: LCL Filter.

Using the design procedure outlined in [64,65], then for a maximum input current variation of 10%, the converter side inductor will be:

$$L_c = \frac{V_{dc}}{16 f_{sw} \Delta I_{\max}} = \frac{V_{dc}}{16 f_{sw} 0.1\sqrt{2}\frac{P_{rated}}{\sqrt{3}V_L}} \tag{24}$$

The filter capacitor is given be C_f=xC_{base} where C_{base} is $P_{rated}/\omega_g V_L^2$, and x is less than 5%, ω_g is the grid frequency (in rad/s) and V_L is the rms line voltage. The size of the grid size inductor is related to the converter side inductor by L=rL, where r can be obtained based on the ripple attenuation of the LC filter, given by:

$$\frac{i_g(h)}{i_c(h)} = \frac{1}{\left|1 + r\left[1 - L_c C_{base} \omega_{sw}^2 x\right]\right|} \tag{25}$$

where h is the harmonic number. If the ripple attenuation is 20%, then the total current ripple will be 2%. The damping resistor should be set high enough to reduce losses, but too high a value will reduce the damping effectiveness. It will be set to 1/3rd the impedance of the capacitor at the filter resonant frequency given by:

$$\omega_{res} = \sqrt{\frac{L_c + L_g}{L_c L_g C_f}} \tag{26}$$

The resonant frequency should be between 10x the line frequency and half the switching frequency. Further reduction in filter losses can be obtained by using an inductor in parallel with the resistor as in [65], given by:

$$L_f = \frac{R_f}{\omega_{res}} \tag{27}$$

Note that the transformer leakage inductance should be included in the grid inductance (L_g). The final filter component ratings for a total ripple value of 2% will be:

Table 2: 3-level VSC filter component ratings for a 3 MW converter with a 1000 V DC voltage.

L_c	398 μH
C_f	400 μF
L_g	272 μH
R_f	0.21 Ω
L_f	51 μH

3.2 MV Transformer

The MV transformer must be rated for the full power of the wind generator and should have good efficiency over the whole operating area. Size, weight, and insulation type may also be important design factors depending on the location.

3.2.1 Transformer Design Overview

The transformer ratio required depends on the LV and MV bus voltages. The LV side is determined by the wind turbine rating and is normally less than 1000 V. The MV side usually varies from 12 kV to 33 kV, with higher voltages normally used at larger and higher power wind farms to limit cable losses in the MV system and the HV transformer [1].

Most MV and HV transformer winding designs are wound in disks or interleaved disks (for higher strength against voltage impulses). Each disk will contain a number of turns and is separated from other disks by an insulation gap that allows cooling of the winding. Normally the LV winding is used as the inner winding. Insulation is required around the conductors, between the LV winding and the core, between the HV winding and the LV winding, between the HV windings of separate phases, and between the windings and the yokes [66].

The transformer insulation is normally a combination of paper and oil. The oil increases the resistivity of the paper insulation and improves the cooling of the transformer. Typically, an insulation electrical strength of 1 kV/mm is used for the transformer design, although the electrical strength of oil immersed paper can exceed 65 kV/mm [67,66]. Dry or air cooled transformers can be used in certain applications (such as indoors).

The transformer core is normally made of silicon steel, which offers high saturation flux density and low losses. Amorphous steel cores have also been used in small and medium power distribution transformers and offer lower core losses, but have lower saturation flux density. Core loss for 0.23 mm silicon steel and for Metglas amorphous steel are in Figure 18.

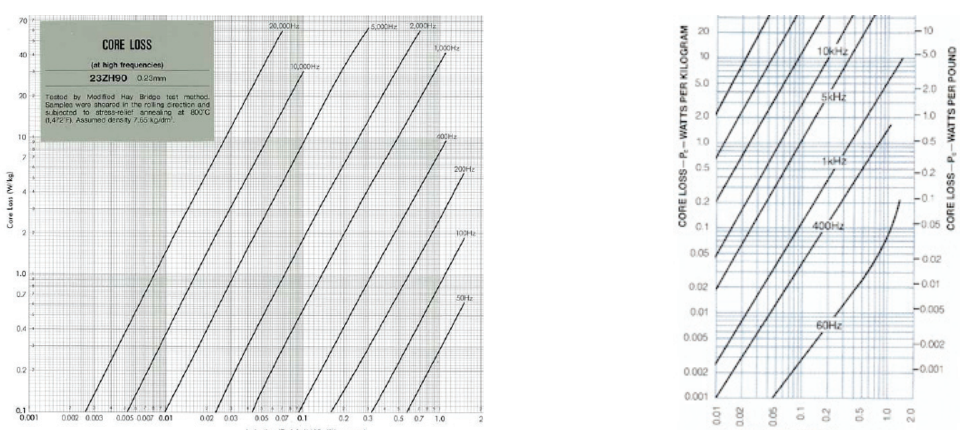

(a) 0.23 mm Silicon steel core loss (from Nippon Steel datasheet)

(b) 2605SA1 Metglas Amorphous Steel (from Metglas material datasheet)

Figure 18: Core loss per kg in silicon steel and amorphous steel.

A comparison between a MV amorphous core transformer and a MV silicon steel core transformer is in Appendix B.2. The amount of leakage reactance is a trade-off between having a low leakage reactance and improved voltage regulation and having a higher reactance and lower fault current. In most designs, the leakage reactive is around 10% [66].

Most transformers operate at very high efficiencies (>98%). Designing the transformer normally uses a cost minimization function to minimize the material costs and the core and copper losses. Transformer losses were outlined in Section B.1. Since the wind power output will typically operate well below the rated power, the design of a MV transformer for a wind turbine should be designed based on the wind characteristics of an area.

3.2.2 Grid Frequency MV Transformer

For the AC grid topology shown in Figure 9 (a), a 3 MVA transformer rated for 1/33 kV at 60 Hz will be considered. Using the amorphous core transformer design from Appendix B.1, then the efficiency for various wind powers for a transformer designed for an area with an average wind speed of 8 m/s is as shown in Figure 19.

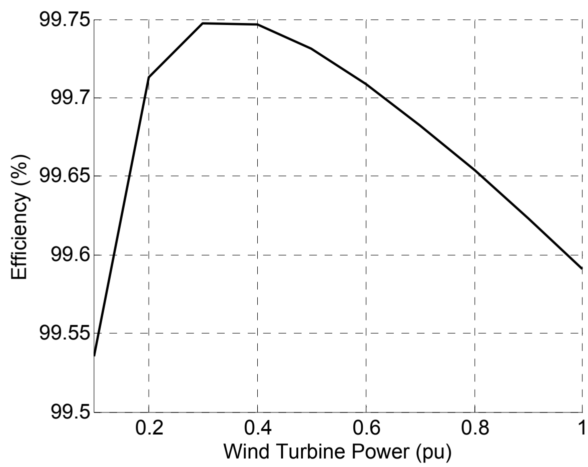

Figure 19: 1/33 kV, 3MVA amorphous core transformer efficiency.

The final transformer design variables are listed in Table 3.

Table 3: 3 MVA, 1/33 kV MV Transformer design.

Copper weight	1811 kg
Core weight	3268 kg
Core diameter	313.7 mm
Number of HV turns	660
Number of LV turns	20
LV/HV winding height	557.3 mm
LV winding width	77.3 mm
HV winding width	118 mm

3.3 HV Transformer

The HV transformer is used to transform the voltage for the VSC HVDC converter. The actual voltage level will depend on the VSC converter modulation; however for the SPWM based converters in Sections 3.1.1 and 3.1.2, the DC and AC voltage are related by:

$$V_{LL} = \frac{\sqrt{3}}{\sqrt{2}} \frac{v_{cont}}{v_{tri}} \frac{V_{dc}}{2} \tag{28}$$

where v_{cont}/v_{tri} is the modulation factor. If the modulation factor is around 0.95, and the VSC converter will connect to a 500 kV HVDC line, then the AC voltage should be approximately 290 kV. Many of the structural, mechanical, and insulation issues are more significant with HV transformers and therefore a detailed design will not be performed as for the MV transformers in Section 3.2. The efficiency is expected to be greater than 99% [68]. The weight can be expected to be greater than 300 tons, since offshore transformers for two 200 MW wind farms to be constructed near Denmark will be 280 and 300 tons.

3.4 HV VSC HVDC Converter

The VSC HVDC converter will connect the HVAC from the HV transformer to a 500 kV DC line.

The same design steps as in Section 3.1.1 will be used for a 300 MW converter to connect to the 500 kV HVDC line. ABB 5SNA 0750G650300 IGBT switches will be used (relevant characteristics were shown in Table 1). The total calculated 2-level converter losses are shown in Figure 20. The number of IGBTs required is 924 (154 in series per valve).

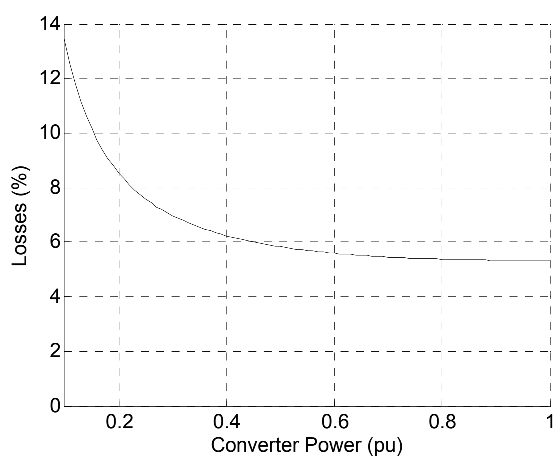

Figure 20: HV 2-level VSC HVDC converter losses.

Similarly to Section 3.1.2, the losses for a 3-level converter can be calculated using the switch information in Table 1. These losses are shown in Figure 21. The total number of IGBTs required is 924 (154 in series per valve).

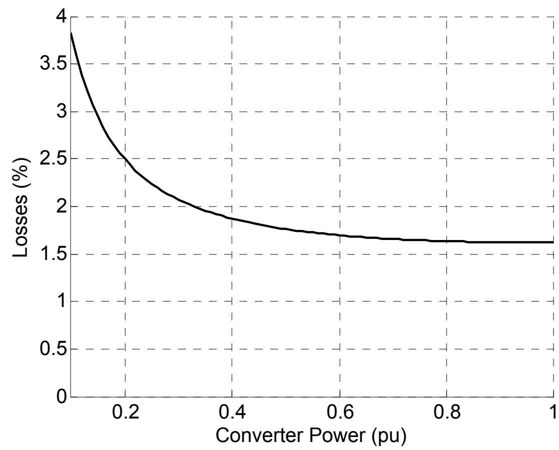

Figure 21: HV 3-level VSC HVDC converter losses.

As can be seen, the losses in a 3-level converter offer a substantial improvement and do not result in an increased number of IGBTs (but will require more diodes for the NPC). These types of converters have therefore been used in many recent VSC HVDC installations.

Harmonics for VSC HVDC converters are usually filtered by tuned shunt filters located on the converter side of the AC transformer.

CHAPTER 4: DC GRID DESIGN

From Section 1.2.4, the concept of a wind farm with a DC grid has been proposed for offshore applications as a way to reduce costs and increase efficiency. Similar topologies would be used as for an AC grid; however, instead of a DC-AC converter and transformer, a DC-DC converter would connect each wind turbine to a MV DC bus. The MV bus would then be connected to a HVDC line using an HV DC-DC converter. The connection of a single wind turbine in a wind farm to an HVDC line is shown in Figure 22.

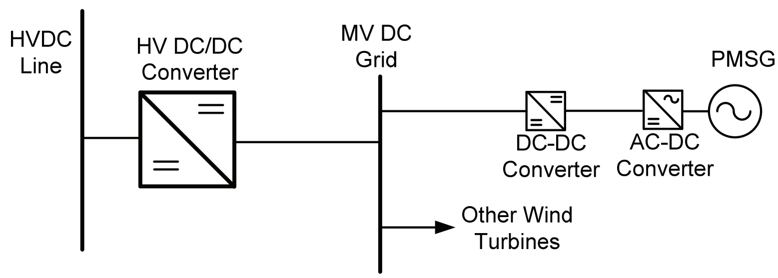

Figure 22: DC bus based wind farm.

The DC-DC converter proposed in [69,70] may offer some advantages for a DC grid based wind farm but it will depend on the ability to operate efficiently and to be stable during faults. The efficiency will be analyzed in detail in this section and the performance during faults will be evaluated in Chapter 5.

4.1 MV Resonant Converter

The MV converter proposed in [69,70] is shown in Figure 23.

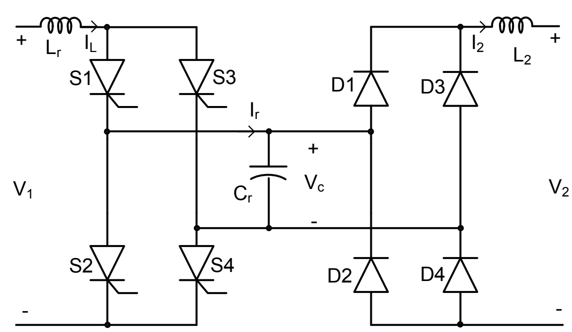

Figure 23: External inductance resonant converter.

The main equations for the inductor current and capacitor voltage are:

$$i_L(t) = I_{L0}\cos(\omega_0(t-t_0)) + \frac{V_s - V_{C0}}{Z_0}\sin(\omega_0(t-t_0)) \tag{29}$$

$$v_C(t) = V_s - (V_s - V_{C0})\cos(\omega_0(t-t_0)) + Z_0 I_{L0}\sin(\omega_0(t-t_0)) \tag{30}$$

where I_{L0} and V_{C0} are the initial inductor current and capacitor voltage and ω_0 and Z_0 are the resonant frequency and characteristic impedance defined as:

$$\omega_0 = \frac{1}{\sqrt{L_r C_r}} \tag{31}$$

$$Z_0 = \sqrt{\frac{L_r}{C_r}} \tag{32}$$

Note that in discontinuous mode, the initial conductor current (I_{L0}) will be zero and the initial capacitor voltage (V_{C0}) will be -V_2.

The resonant DC converter in Figure 23 operates by changing the direction of the current through the series resonant circuit. This effectively inputs an AC voltage onto the resonant circuit with a frequency equal to the switching frequency. Depending on the switching frequency the following operational modes are possible:

a) Switching at the resonant frequency
b) Switching below resonant frequency (discontinuous mode)
c) Switching above resonant frequency (continuous mode)

When the switching frequency is equal to the resonant frequency, then the circuit can be divided into two stages depending on the switches that are operating. These are shown in Figure 24.

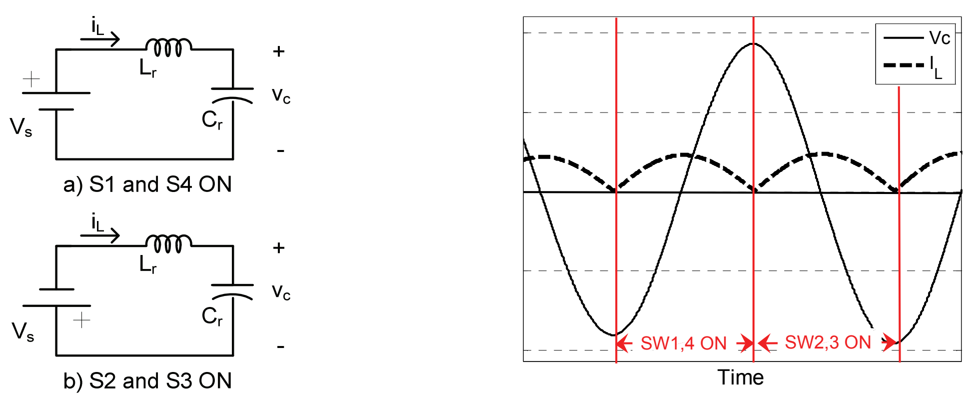

Figure 24: Switching at the resonant frequency.

When operating in discontinuous mode (below the resonant frequency), there will be a delay between when one set of switches turns off and when another turns on. When operating in the continuous mode (above the resonant frequency), one set of switches will turn on before the current in the other has decreased to zero. This will reverse bias the other switches, turning them off. The resonant inductor current and capacitor voltage during discontinuous and continuous mode operation is shown in Figure 25.

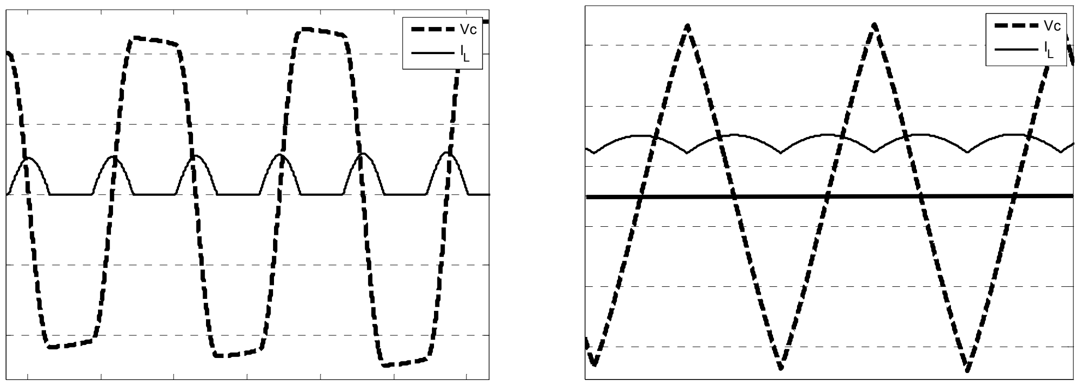

(a) Discontinuous mode. (b) Continuous mode.

Figure 25: Resonant voltage and current with switching above and below resonant frequency.

The required switch ratings will change depending on the switching frequency. The switch currents and voltages during continuous and discontinuous mode operation are shown in Figure 26.

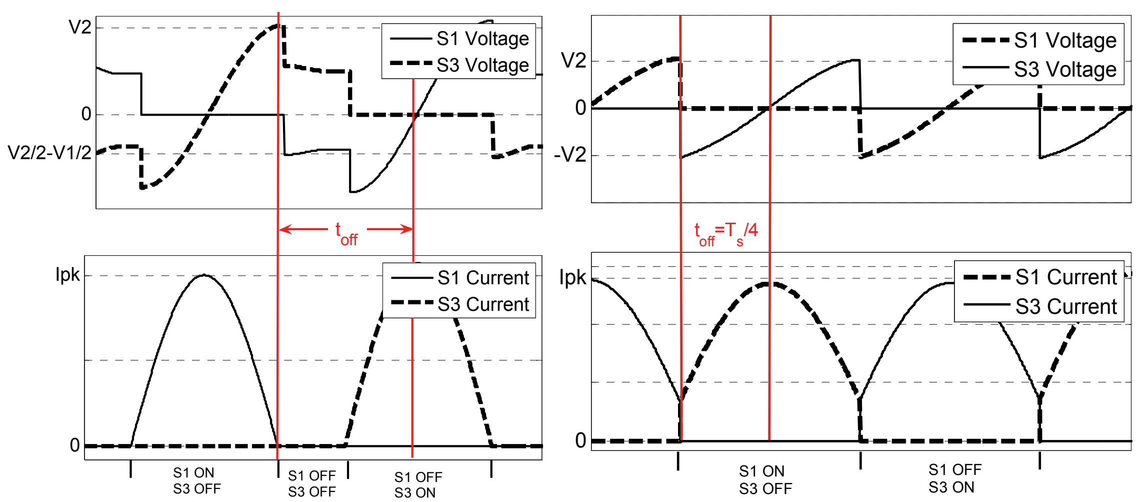

(a) Discontinuous mode. (b) Continuous mode.

Figure 26: Switching voltage and current characteristics.

As can be seen in Figure 26, the switches may experience high *di/dt* effects when switched above the resonant frequency and a series inductor may be required to reduce the *di/dt*. The turn-off voltage in discontinuous mode is $V_2/2$-$V_1/2$, much lower than that in continuous mode and therefore results in reduced switching losses.

The sizing of the series inductor will depend on the maximum *di/dt* of the thyristor. For example, the ABB 5STP 38Q4200 (considered in Section A.1) datasheet lists the maximum rate of rise of on-state current as 250 A/μs (for continuous switching at 50 Hz). In addition, the time after the switch turns off and the zero crossing of the voltage must be greater than the maximum circuit commutated turn-off time. Some example rated turn-off times for various thyristors are given in Table 4.

Table 4: Comparison of thyristor turn-off times from different manufacturers.

	Peak Voltage	Average Current	Turn-off time
5STP 16F2800	2800 V	1400 A	400 μs
5STP 08F6500	6500 V	830 A	700 μs
5STP 12F4200	4200 V	1150 A	600 μs
SPT411A	5000 V	4600 A	400 μs
SPT314A	2500 V	4700 A	300 μs
SPT407	2500 V	7525 A	300 μs
FT1500AU-240	12000 V	1500 A	1000-2000 μs
DCR720E	1800 V	724 A	300 μs
DCR1008SF	3600 V	1051 A	500 μs
EUPEC T2563 N	8000 V	2520 A	550 μs

Note that manufacturers may allow reduced turn-off times, although this will lead to higher on-state losses. As well, these turn-off times depend on the voltage gradient (e.g. 20 V/μs for ABB thyristors) and can be reduced for lower gradients. The voltage gradient can be varied with an RC snubber, where:

$$\left(\frac{dv}{dt}\right)_{\max} = \frac{V_{OFF}}{R_s C_s} \tag{33}$$

In discontinuous mode, the turn-off time is given by:

$$t_{off} = \frac{T_0}{4} + \frac{T_s - T_0}{2} = \frac{T_s}{2} - \frac{T_0}{4} \tag{34}$$

In continuous mode the turn-off time is given by:

$$t_{off} = \frac{T_s}{4} + \frac{T_s - T_s}{2} = \frac{T_s}{4} \tag{35}$$

Therefore the maximum switching frequency is given by:

$$f_{s\max} = \begin{cases} \dfrac{1}{4 \cdot T_{off\max}} & T_s \le T_0 \\ \dfrac{1}{2 \cdot T_{off\max} + \dfrac{T_0}{2}} & T_s > T_0 \end{cases} \tag{36}$$

Due to the short turn-off times in continuous current mode and the high *di/dt*, only the discontinuous mode will be considered (more details on the continuous mode operation are in Appendix C.2).

Other important design parameters include the peak current and power for different switching frequencies. Using the analysis in Appendix C.1, the peak current in discontinuous mode is given by:

$$I_p = \left(\frac{V_1 + V_2}{Z_0}\right) \tag{37}$$

and the average current in discontinuous mode is given by:

$$I_{Lave} = 4(V_1 + V_2)C_r f_s \tag{38}$$

From Appendix C.1.2, the converter power is given by:

$$P_{\max} = E_{in} \cdot 2f_s = \frac{2V_1V_2^2C_r}{V_2 - V_1}2f_s \tag{39}$$

4.1.1 Component Requirements

The component requirements of the switches and the resonant inductors and capacitors are listed in Table 5.

Table 5: Single phase DC-DC converter component requirements.

Component	Rating
Thyristor ($S_{1\text{-}4}$)	▪ Current—rated for the average input current (eq. (37)). Note that the peak current will be high, but the switch will be off for half the switching cycle. ▪ Voltage—rated for peak voltage which is greater than $V_2 + 2V_1$ (depending on the value of L_2)
Diode ($D_{1\text{-}4}$)	▪ Current—rated for the average output current ▪ Voltage—rated for peak voltage which is greater than $V_2 + 2V_1$ (depending on the value of L_2)
Capacitor (C_r)	▪ Current—rated for the peak input current (eq. (37)) ▪ Voltage—rated for peak voltage which is greater than $V_2 + 2V_1$ (depending on the value of L_2)
Inductor (L_r)	▪ Current—rated for the peak input current (eq. (37)) ▪ Voltage—rated for peak voltage which is greater than $V_2 + 2V_1$ (depending on the value of L_2)

The power ratings for the thyristors and the resonant capacitor and inductor will be very large since they must be rated for LV side current and the HV side voltage. When operating close to the resonant frequencies, the resonant capacitor and inductor rating can be approximated as an equivalent MVAR rating of:

$$Q_{eq} = \frac{V_2}{\sqrt{2}} \frac{I_1 \frac{\pi}{2}}{\sqrt{2}} = \frac{\pi}{4} G_c P_c \tag{40}$$

where G_c is the gain of the converter.

4.1.2 Design Example

The converter will be designed to step up the voltage from 1000 V to 33 kV and will be designed for a maximum power of 3 MW. Assuming a PWM based DC rectifier, then the DC voltage will be given by:

$$V_{dc} = \frac{2\sqrt{2}V_{LL}}{m\sqrt{3}} \tag{41}$$

where m is the modulation index. Assuming operation in the linear region, then m must be less than 1 and will be assumed to be 0.95 for this design and the resulting DC voltage will be 1720 V_{DC}. Using the maximum power (eq. (39)), then the size of the resonant capacitor is:

$$C_r = \frac{P_{\max}\left(V_2 - V_1\right)}{4 f_s V_1 V_2^2} \tag{42}$$

Using the maximum switching frequency for discontinuous mode operation (eq. (36)), then the value of the resonant inductor will be given by:

$$L_r = \frac{1}{C_r \pi^2}\left(\frac{1}{f_s} - 2T_{off}\right)^2 \tag{43}$$

If the maximum power corresponds to the boundary between the continuous and discontinuous operation, f_s=f_o=$1/(4T_{off})$, using (42) and (43), then:

$$L_r = \frac{2T_{off}}{\pi^2\left(\frac{P_{\max}\left(V_2 - V_1\right)}{2V_1 V_2^2}\right)} \tag{44}$$

$$C_r = 2T_{off}\left(\frac{P_{\max}\left(V_2 - V_1\right)}{2V_1 V_2^2}\right) \tag{45}$$

Therefore as the maximum power increases, the capacitor size will increase and the inductor size will decrease and decreasing the switch turn-off time will decrease the size of both the capacitor and inductor. In addition, since the peak input current is given by:

$$I_p = \left(V_1 + V_2\right)\sqrt{\frac{C_r}{L_r}} \tag{46}$$

then I_p is directly related to the maximum power and is independent of the turn-off time.

Three switches will be compared for this design: the ABB 5STP 12K6500, the ABB 5STP 12F4200, and the ABB 12N8500 and will be referred to as designs A, B, and C. Using a turn-off time equal to the maximum turn-off time of the switches and designing so that the maximum power of the converter corresponds to the border between the continuous and discontinuous modes, then the resulting size of the inductor will be 6.5 mH for Design A.

As can be seen by the waveform in Figure 26, when all switches are off, then the voltage across the switches will be around $V_2/2$. Allowing the switch voltage to remain at a lower voltage over the reverse recovery time will reduce the turn-off losses (outlined in Section A.1). To take advantage of this, the maximum turn-off time in this design will be increased by the reverse recovery time of the switches, therefore:

$$f_{s\max} = \frac{1}{T_0 + 2t_{rr}} = \frac{1}{4T_{off} - 2t_{rr}} \tag{47}$$

Note that if the high voltage inductor is small, then the diode turn-off losses will also be reduced, since the voltage across the capacitor will be constant at the end of the switching cycle that will allow the diodes to turn off before the beginning of the next switching cycle.

The reverse recovery time can be estimated using the rate-of-change of current when the switches turn off, which from (C14) is given by:

$$s_i = \frac{di_{sw}(t)}{dt} = \frac{(V_1 - V_2)}{L} \tag{48}$$

and are equal to 4.81 A/μs for Design A. From the switch datasheet, the reverse recover charge and current can be estimated as 5510 μAs and 174 A for Design A. From Figure A-5(b), the reverse recovery time will be:

$$t_{rr} = \frac{2Q_{rr}}{I_{rr}} \tag{49}$$

and will be equal to 63.3 μs for Design A. Using (42), (43), and (47), the sizes of the resonant capacitor and inductor are given by:

$$L_r = \frac{4(T_{off} - t_{rr})}{\pi^2 \left(\frac{P_{\max}(V_2 - V_1)}{2V_1 V_2^2} \right) (2T_{off} - t_{rr})} \tag{50}$$

$$C_r = \left(2T_{off} - t_{rr}\right)\left(\frac{P_{\max}\left(V_2 - V_1\right)}{2V_1V_2^2}\right) \tag{51}$$

The resulting inductor sizes are 5.7 mH for Design A. The resulting rate-of-change of current when the switches turn off will result in similar reverse recovery times as before. The output capacitor and input capacitors will be designed for a maximum 5% variation using (C33) and (C34). The resulting converter parameters for designs A, B, and C, using the same design procedure, are listed in Table 6.

Table 6: Converter design components for a 1.72/33 kV, 3 MW wind turbine DC-DC converter.

	Design A	Design B	Design C
Switch model	ABB 12K6500	ABB 12F4200	ABB 12N8500
Turn-off time	800 µs	600 µs	800 µs
Resonant capacitor (C_r)	38.5 µF	28.4 µF	38.3 µF
Resonant inductor (L_r)	5.7 mH	4.1 mH	5.6 mH
Resonant frequency	339 Hz	467 Hz	342 Hz
Maximum switch frequency	325 Hz	440 Hz	327 Hz
Peak current	2.85 kA	2.90 kA	2.86 kA
Max. rate-of-change of current (s)	6.1 A/µs	7.66 A/µs	5.5 A/µs
LV DC capacitor	31.1 mF	23 mF	31 mF
MV DC capacitor	82.6 µF	61 µF	82.3 µF

Note that the switching frequency in this thesis is based on a switching period from when a switch turns on to when it turns on again. There will be two current pulses in each period.

The number of series connected thyristors per switch valve will be designed for the secondary voltage with a 100% margin. Therefore each valve will have 11 thyristors for Design A, 16 thyristors for Design B, and 8 thyristors for Design C.

The thyristor utilization, as defined in [57], will be given by:

$$U = \frac{P_{\max}}{q_{thy} I_{thy} V_{thy}} \tag{52}$$

where q_{thy} is the total number of thyristors in the inverter and I_{thy} and V_{thy} are the peak voltage and rms current through the switches. The full load utilization ratios of designs A, B, and C vary between 0.1% for Design B and 0.2% for Design C.

4.1.3 Converter Losses

Using the design examples, the converter losses can be estimated based on the methods outlined in Section A.1.

4.1.3.1 Switch Losses

At turn-on, the initial current through a thyristor is zero (since it is operating in discontinuous mode) and the initial voltage across the thyristor will be equal to $V_2/2$-$V_1/2$. Estimating the initial resonant capacitor voltage at the time of switching as V_2, then the current through the switch at turn-on will be:

$$i_{sw}(t) = i_L(t) = \frac{V_1 + V_2}{Z_0}\sin(w_0 t) \tag{53}$$

The time to reach the peak of the input current will be:

$$t_p = \frac{1}{4f_0} \tag{54}$$

This time for both designs is too short to be obtained from the switch datasheet graphs of the turn-on energy for half sinusoidal waves (the minimum time specified is 1 ms). To estimate the losses using (A5), V_{OFF} is considered equal to $V_2/2$-$V_1/2$, the rate of change of current given in Table 6, and t_{v0} is estimated as outlined in Section A.1, the turn-on loss per half-cycle can be approximated as:

$$W_{turn-on} = 2\left(\frac{V_{OFF}}{6}s_i t_{v0}^2\right) = \frac{1}{3}s_i t_{v0}^2\left(\frac{V_2}{2} - \frac{V_1}{2}\right) \tag{55}$$

where s_i is the rate of change of current during turn-on, and t_{v0} is the time for the voltage to decrease to the on-state voltage (see Appendix A.1). Eq. (55) is multiplied by two since two sets of thyristors will turn on in each half cycle.

To estimate the turn-off losses, Q_{rr} and I_{rr} can be obtained from the datasheet depending on the rate-of-change of current. From (A7) and Q_{rr} and I_{rr} (given in Section 4.1.2), the reverse recovery losses can be estimated as:

$$W_{RR} = 2\left(Q_{RR}V_{OFF} - \frac{I_{rr}^2 V_{OFF}}{2s_i}\right) = 2\left(Q_{RR} - \frac{I_{rr}^2}{2s_i}\right)\left(\frac{V_2}{2} - \frac{V_1}{2}\right) \tag{56}$$

The thyristor conduction losses can be estimated using (A1). Therefore from (29) and (C14), the on-state losses over one half-cycle will be given as:

$$W_{ON}=\int_0^{t_C} I_L(t)2n_{sw}\left(V_{T0}+r_T I_L(t)\right)dt$$

$$=2n_{sw}\left[V_{T0}I_{1ave}+r_T\left(\left(\frac{V_1+V_2}{Z_0}\right)^2\left(\frac{t_B}{2}-\frac{1}{4\omega_0}\sin(2\omega_0 t_B)\right)+I^2(t_B)(t_C-t_B)+\right.\right.$$

$$\left.\left.+2I(t_B)\left(\frac{V_1-V_2}{L}\right)\frac{t_C^2-t_B^2}{2}+\left(\frac{V_1-V_2}{L}\right)^2\frac{t_C^3-t_B^3}{3}\right)\right] \tag{57}$$

where n_{sw} is the number of series connected thyristors per switch valve and t_B and t_C are shown in Figure C-1. The thyristor off-state losses per half cycle can be estimated using the forward and reverse blocking leakage current:

$$W_{OFF}=2\int_0^{T_0/2} V_{OFF}^2(t)\frac{I_{leak}}{n_{sw}V_{thy}}dt+4\int_{T_0/2}^{T_s/2} V_{OFF}^2\frac{I_{leak}}{n_{sw}V_{thy}}dt$$

$$=2\int_0^{T_0/2}\left[V_1-(V_1+V_2)\cos(\omega_0 t)\right]^2\frac{I_{leak}}{n_{sw}V_{thy}}dt+4\int_{T_0/2}^{T_s/2}\left(\frac{V_2}{2}-\frac{V_1}{2}\right)^2\frac{I_{leak}}{n_{sw}V_{thy}}dt$$

$$=2\int_0^{T_o/2}\left[(V_1+V_2)\sin(\omega_0 t)\right]^2\frac{I_{leak}}{n_{sw}V_{thy}}dt+4\int_{T_0/2}^{T_s/2}\left(\frac{V_2}{2}-\frac{V_1}{2}\right)^2\frac{I_{leak}}{n_{sw}V_{thy}}dt$$

$$=2(V_1+V_2)^2\frac{1}{4f_0}\frac{I_{leak}}{n_{sw}V_{thy}}+4\left(\frac{V_2}{2}-\frac{V_1}{2}\right)^2\frac{(T_s-T_o)}{2}\frac{I_{leak}}{n_{sw}V_{thy}} \tag{58}$$

where I_{leak} is the leakage current. The thyristor parameters (either estimated or obtained from the datasheet) used for calculation of the losses of the two converter designs are summarized in Table 7.

Table 7: Thyristor parameters for calculating losses in a 1.72/33 kV, 3 MW DC-DC converter.

	Design A	Design B	Design C
Model	ABB 12K6500	ABB 12F4200	ABB 12N8500
t_{v0}	23 µs	21.1 µs	23 µs
Q_{rr}	6186 µAs	4873 µAs	11218 µAs
I_{rr}	206 A	159 A	346 A
V_{T0}	1.18 V	0.95 V	1.25 V
r_T	0.63 mΩ	0.575 mΩ	0.48 mΩ
n_{sw}	11	16	8
I_{leak}	600 mA	200 mA	700 mA

Using (55)-(58), the total power losses can be calculated at various frequencies of operation. The total power losses will be given by:

$$P_{thy} = \left(W_{turn-on} + W_{RR} + W_{ON} + W_{OFF}\right)2 f_s \tag{59}$$

where only W_{OFF} varies with the frequency of operation. Losses in the HV terminal diodes can be calculated using (C14). The diode on-state losses will be:

$$\begin{aligned} W_{ONdiode} &= \int_0^{T_o/2} I_L(t) 2 n_d \left(V_{F0} + r_F I_L(t)\right) dt \\ &= 2 n_d \left[V_{F0} I_{2ave} + r_F \left(I^2(t_B)(t_C - t_B) + 2 I(t_B)\left(\frac{V_1 - V_2}{L}\right)\frac{t_C^2 - t_B^2}{2} + \left(\frac{V_1 - V_2}{L}\right)^2 \frac{t_C^3 - t_B^3}{3} \right)\right] \end{aligned} \tag{60}$$

where V_{F0} and r_f can be obtained from the datasheet and n_d is the number of diodes connected in series per valve, and the different times are defined in Appendix C.1.1. The diode reverse recovery losses will be ignored since by keeping the switching time below the resonant frequency, then the capacitor voltage will remain close to the turn-off voltage long enough for the diode to fully turn-off before the beginning of the next switching cycle (detailed in Section 4.1.2).

Over each switching period, the voltage across the diodes will change between zero and V_2. In the off-time, after the current has fallen to zero and before the next switching cycle, half of the diodes will have a voltage of V_2 across them. Therefore the diode off-state losses over half a switching cycle will be:

$$W_{OFFdiode} = \frac{4 I_{leak}}{n_d V_{rat}} \int_0^{T_0/2} \left(\frac{V_2}{2} + \frac{V_2}{2}\cos(\omega_0 t)\right)^2 dt + \frac{2 I_{leak} V_2^2}{n_d V_{rat}} \frac{T_s - T_0}{2} = \frac{I_{leak} V_2^2}{n_d V_{rat}}\left(\frac{T_0}{4} + \frac{T_s}{2}\right) \tag{61}$$

The total diode losses will be:

$$P_{diode} = \left(W_{ONdiode} + W_{OFFdiode}\right)2 f_s \tag{62}$$

The diodes should be selected to have a high voltage drop and low on-state losses. These losses should be low since the average current through the diodes will be $I_2/2$. The diodes used for this example are ABB 5SDD 31H6000 rectifier diodes, with parameters in Table 8.

Table 8: Diode parameters for calculating losses in a 1.72/33 kV, 3 MW DC-DC converter.

Model	ABB 12K6500
V_{rrm}	6000 V
I_{Fave}	3246 A
V_{F0}	0.894 V
r_F	0.166 mΩ
I_{leak}	120 mA

The losses for operation at various converter power levels are shown in Figure 27 for all switch designs:

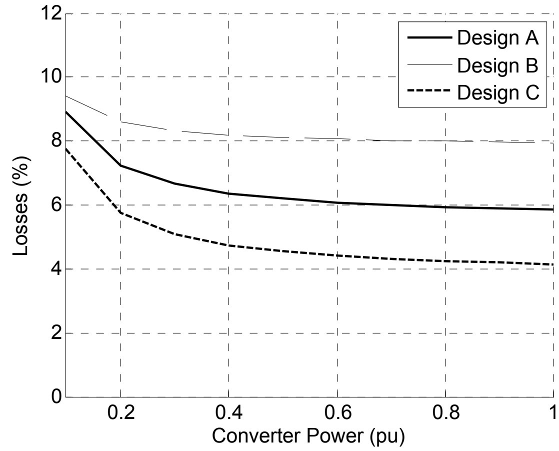

Figure 27: Converter losses at various power levels.

Designs A and C have lower losses due to lower on-state voltage drops and fewer switches. The individual switch losses from the different sources are shown in Figure 28 for Design A.

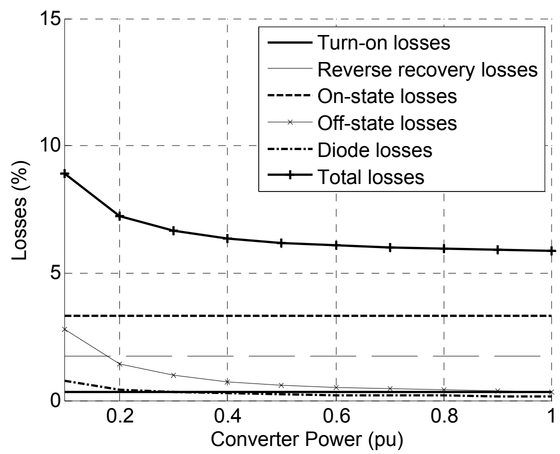

Figure 28: Components of converter losses for Design A at various power levels.

The main sources of thyristor losses at full load are from reverse recovery losses and on-state losses. Design methods to reduce reverse recovery losses include:

- *Reduce di/dt*—this can be reduced by increasing the size of the resonant inductor (or effectively by increasing the switch turn-off time). Adding thyristors in parallel will also decrease the switch *di/dt* but will result in increased number of switches and in increased off-state losses.
- *Use capacitive snubbers*—a capacitive snubber can be used to reduce I_{RR} and the voltage gradient at turn-off.
- *Using fast turn-off thyristors*—these thyristors have low turn-off losses but higher on-state voltage drops which will increase the on-state losses.

Design methods to reduce on-state losses include:

- *Reduce on-state current*—the on-state current can be reduced by adding thyristors in parallel, but will result in higher number of switches and higher off-state losses. In addition, this will only reduce the on-state current due to the on-state resistance (r_T) and losses due to the on-state voltage (V_{T0}) will not decrease, therefore adding more than two in parallel will not greatly decrease these losses.
- *Reduce on-state peak current*—the on-state peak current can be reduced by increasing the size of the resonant inductor (or effectively by increasing switch turn-off time).
- *Using low on-state voltage drop thyristors*—thyristors rated for higher currents generally have lower on-state voltage drops; however, these switches often have higher switching losses and turn-off times.

The losses will also be reduced when a lower converter gain is required. If the input voltage is higher, then a lower current will pass through the switches and will result in lower on-state losses. If the reverse recovery losses then dominate, using fast turn-off thyristors can be advantageous (as noted above). For comparison, Design B is used with a LV input of 3440 V and 6880 V, corresponding to generator AC voltages of 2000 V_{AC} and 4000 V_{AC}. In this case, the average on-state current will be lower and therefore the losses of Design B are compared with a low switching loss (but high on-state loss) thyristor. This is shown in Figure 29. Note that the Polovodiče switch used for Figure 29(b) was designed with the same design steps outlined in Section 4.1.2, but with a turn-off time of 150 μs. Another advantage of the 4000 V_{AC} configuration is that the utilization is twice that of the 1000 V_{AC} configuration.

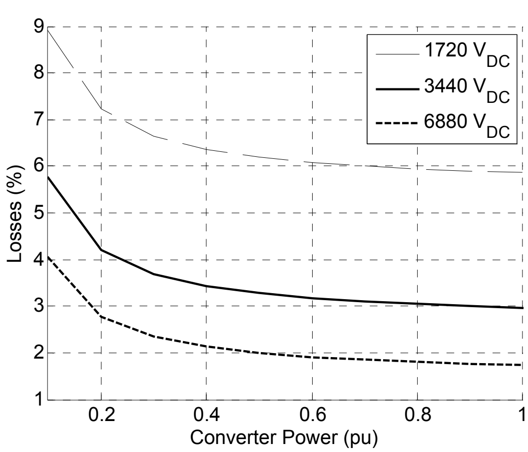

(a) Design B

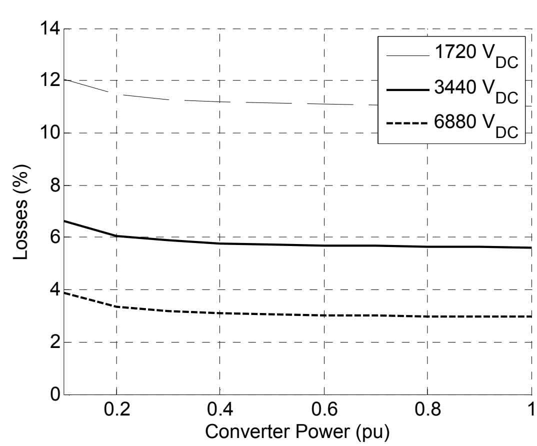

(b) Polovodiče TR918-1010-30

Figure 29: Converter total thyristor switching losses at various DC voltages.

As can be seen, the low reverse recovery losses in fast turn-off thyristors result in comparable converter losses when the average input current is lower. This can be beneficial since operating at a higher frequency will allow a reduction in the component sizes.

4.1.3.2 Resonant Capacitor Losses

The resonant capacitor at full load will have an almost sinusoidal waveform with a voltage amplitude of around $\pm V_2$ and a current amplitude of $\pm I_{pk}$. To estimate the losses in the resonant capacitor, the capacitor losses of from Figure A-11 of 0.1 W/kVar will be used. Approximating the capacitor voltage and current as sinusoidal, then the losses will be:

$$P_{cap} = 0.0001\left(\frac{V_2}{\sqrt{2}}\frac{I_{pk}}{\sqrt{2}}\right) \tag{63}$$

Using (63), the capacitor losses for the converter are around 0.15% at full load operation.

4.1.3.3 Resonant Inductor Losses

The resonant inductor will be designed for the inductances listed in Table 6. The maximum current of the inductor will be I_{pk} = 2.8 kA and the maximum voltage will be V_2 = 33 kV. The cost minimization function in Appendix B.3 will be used to design the inductor.

The conduction losses will vary depending on the frequency of operation and to the characteristics of the wiring. They can be divided into AC and DC losses using Fourier analysis. The AC losses will depend on the harmonics of the input current and losses due to the skin and proximity effect [58]. Using Fourier analysis at operation close to full load (at close to the resonant frequency), the input current can be given by:

$$I_1(t) = \frac{2}{\pi}I_{pk} + \sum_{n=1}^{\infty}\frac{I_{pk}}{2\pi}\left[\frac{1-\cos((1+n)\omega_0)}{1+n} + \frac{1-\cos((1-n)\omega_0)}{1-n}\right]\cos(n\omega_0 t) \tag{64}$$

The only major harmonic will occur at 2x the switching frequency and will be 1/8th of the magnitude of the DC component (which is the average input current). When the switching frequency decreases, more important harmonics will occur at lower frequencies. This can be seen in Figure 30, which shows an FFT plot for the input current when switching at the resonant frequency and at half the resonant frequency.

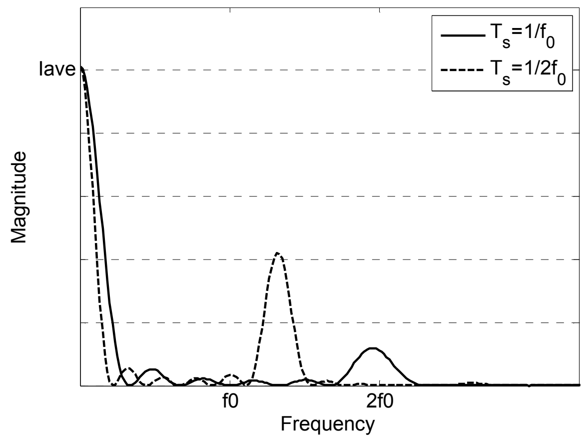

Figure 30: Input current harmonics.

Assuming copper wire, where the permeability is equal to μ_0, the skin depth for a cylindrical wire at 2x the resonant frequency is:

$$\delta = \sqrt{\frac{\rho_{cu}}{2\pi\mu_0 f_0}} \tag{65}$$

The AC resistance of a cylindrical conductor will be approximately equal to the DC resistance when the skin depth is greater than the radius of the wire. Therefore to limit skin effect losses for design B, which has a resonant frequency of 466 Hz, and a resistivity of 1.724e^{-5} Ω-mm, the radius of the conductor should be less than 2.16 mm. If the average current must be less than 4 A/mm^2, then the conductor radius should be greater than 11.8 mm, and therefore multiple parallel conductors or Litz wire may be required. Since the AC component is 1/8th of the magnitude, the issues with skin effect should be lower than with a comparable AC transformer.

If the conductor design is assumed to minimize additional skin and proximity effect losses, then using (29) and (C14), the DC copper losses will be given by:

$$\begin{aligned} P_{cu} &= \int_0^{t_C} I_L^2(t) R_{cu} dt \cdot 2 f_s \\ &= 2R_{cu} f_s \left(\left(\frac{V_1 + V_2}{Z_0} \right)^2 \left(\frac{t_B}{2} - \frac{1}{4\omega_0} \sin(2\omega_0 t_B) \right) + I^2(t_B)(t_C - t_B) + \right. \\ &\qquad \left. + 2I(t_B) \left(\frac{V_1 - V_2}{L} \right) \frac{t_C^2 - t_B^2}{2} + \left(\frac{V_1 - V_2}{L} \right)^2 \frac{t_C^3 - t_B^3}{3} \right) \end{aligned} \tag{66}$$

where R_{cu} depends on the conductor resistivity, the length, and the cross sectional area. If an inductor core is used, then from (B35), the core losses will be given by:

$$P_{core} = \frac{1}{2} k B^{\beta} f_0^{\alpha} \cdot \frac{f_s}{f_0} \cdot M_{core} \tag{67}$$

where V_{core} is the volume of the core and the core loss equation is divided by two because of the unipolar flux.

Based on (39) and (B11), and using the Raleigh distribution to estimate the wind variation, the expected switching frequency for a mean wind speed will be given by:

$$E_{fs} = \int_4^{25} f_s \frac{\pi}{2}\left(\frac{U}{\overline{U}}\right) e^{-\frac{\pi}{4}\left(\frac{U}{\overline{U}}\right)^2} dU = \int_4^{25} P_T(U)\left(\frac{V_2 - V_1}{4V_1V_2^2C_r}\right)\frac{\pi}{2}\left(\frac{U}{\overline{U}}\right) e^{-\frac{\pi}{4}\left(\frac{U}{\overline{U}}\right)^2} dU \tag{68}$$

where $P_T(U)$ can be estimated at various wind speeds based on (B6). As can be seen, both the core losses and the copper losses are linearly related to the switching frequency. Since the converter power is also related to the switching frequency then the efficiency over the entire range of operation will be constant.

The final inductor properties, based on minimizing the cost of the core and conductor materials (as outlined in Appendix B.3) and the cost of the losses over the lifetime of the converter, are summarized in Table 9. The flux in the core will be the sum of the AC and DC flux densities (given in (B24) and (B25)), and will be a maximum close to the zero crossing of the resonant capacitor voltage. The flux density at this point can be estimated as:

$$\begin{aligned} B_{\max} = B_{DC} + B_{AC} &= \frac{\mu_0 n I_{\max}}{l_g} + \frac{1}{nA_c}\int_T V_L(t)dt = \frac{\mu_0 n I_{\max}}{l_g} + \frac{V_2}{2\omega_0 n A_c} \\ &\cong \frac{\mu_0 n I_{\max}}{l_g} + \frac{I_{\max} Z_0}{2\omega_0 n A_c} = \frac{3}{2}\frac{\mu_0 n I_{\max}}{l_g} \end{aligned} \tag{69}$$

Table 9 shows the resulting design for an air core inductor as in Appendix B.3.1, with an average current density in the conductor set to 4 A/mm^2 (of the average full load current). Allowing this parameter to vary will increase the efficiency (up to around 99%) but will require more copper. An illustration of the toroid inductor dimensions is in Figure B-8.

Table 9: Toroid air core inductor design for a 1.72/ 33 kV, 3 MW single phase DC-DC converter.

	Designs A and C	Design B
Inductance (L)	5.7 mH	4.1 mH
Core diameter (d_c)	0.87 m	0.81 m
Conductor size (w_{cui}xl_{cu})	145x2043 mm^2	137x1920 mm^2
Conductor weight (M_{cu})	2375 kg	1949 kg
Ave. current density	4 A/mm^2	4 A/mm^2
Number of turns (n)	191	167
Expected efficiency	96.9%	97.4%

Based on the results in Table 9, the efficiency varies very little between the three designs. For comparison, inductors using a silicon steel core (with B_{max} set to a maximum of 1.5 T) and an amorphous steel core (with B_{max} set to a maximum of 1.2 T) are shown below:

Table 10: Toroid steel core inductor design for a 1.72/ 33 kV, 3 MW single phase DC-DC converter.

	Silicon Steel	Amorphous Steel
Inductance (L)	5.7 mH	5.7 mH
Max. flux density (B)	1.5 T	1.2 T
Core weight (M_{fe})	4167 kg	9557 kg
Core diameter (d_c)	0.44 m	0.64 m
Air gap (l_g)	0.42 m	0.28 m
Conductor size (w_{cu}xl_{cu})	55x320 mm^2	52x298 mm^2
Conductor weight (M_{cu})	930 kg	637 kg
Ave. current density	4 A/mm^2	4 A/mm^2
Number of turns (n)	135	62
Expected efficiency	98.1%	99%

As can be seen from Table 9 and Table 10, the air core conductors have worse efficiencies than those designed using silicon steel or amorphous steel, although equivalent efficiencies could be achieved by decreasing the current density (which was set to 4 A/mm^2). Air core inductors are easier to cool and construct, although they may require a magnetic shield depending on the design and the surrounding equipment.

Use of wind turbines with a higher output voltage will result in lower inductor sizes and losses in addition to lower switching losses (as seen in Figure 29). Toroid designs for inductors designed for Design A and Polovodiče TR918-1010-30 switches for a converter with an input voltage of 6880 V are shown in Table 11.

Table 11: Toroid air core design for a 6.88/33 kV, 3 MW single phase DC-DC converter.

	Design A	TR918-1010-30
Inductance (L)	25.6 mH	4.6 mH
Core diameter (d_c)	0.68 m	0.48 m
Conductor size (w_{cui}xl_{cu})	113x1590 mm^2	80x1128 mm^2
Conductor weight (M_{cu})	1108 kg	396 kg
Ave. current density	4 A/mm^2	4 A/mm^2
Number of turns (n)	459	231
Expected efficiency	98.6%	99.5%

As can be seen, the design using Polovodiče TR918-1010-30 fast turn-off thyristors has a higher efficiency and a much lower weight.

4.2 MV 3-Phase Resonant Converter

A possible variation of the resonant converter described in Section 4.1 is the 3-phase resonant converter described in Appendix C. This converter offers some improvements over the single-phase resonant converter, including:

- *Lower peak input current*—I^2R losses can be reduced in both the converter switches and the resonant inductors due to lower peak currents at full load. The peak input current at high switching frequencies will be close to the average input current. The efficiency advantages will be greatest for high power converters that will have a high peak current.
- *Lower switching losses*—by placing an inductor in each converter branch, the rate-of-change of current can be reduced (depending on the size of the inductor). Lowering the rate-of-change of current will decrease reverse recovery losses and turn-on losses, and allow the converter to be operated in discontinuous mode (which would result in very high di/dt with a single inductor).
- *Lower input current ripple*—since the converter can be operated in discontinuous mode, the input current at high switching frequencies will be close to a constant value equal to the average current.

The main disadvantages of this converter compared to the single phase converter are 1.5x the number of switches, 6x the number of inductors, and 3x the number of capacitors.

4.2.1 Design Example

If the minimum turn-off time of the thyristors is known, then the maximum switching frequency can be calculated since the turn-off time in continuous mode operation is $1/6^{th}$ the switching period. Since the converter will be designed for a set maximum power and maximum discontinuous mode current, then (D41) and (D89) can be used to obtain the resonant capacitance and inductance size. Designs using the same switches as were used in Section 4.1.2 will be compared. Note that to limit the sizes of the resonant inductors, Designs A and C will use a peak discontinuous mode current of 750 A while Design B will use a peak discontinuous mode current of 500 A.

The peak current in the switch (in continuous mode) can be calculated based on (D91). The resulting converter designs are summarized in Table 12. The number of thyristors per switch is based on a maximum switch voltage of V_2 with an extra 10% margin. The HV side capacitor will be sized using (D43) for a maximum voltage variation of 5% per pulse.

Table 12: 3-phase converter designs for a 1.72/33 kV, 3 MW DC-DC converter.

	Design A	Design B	Design C
Switch Model	ABB 12K6500	ABB 12F4200	ABB 12N8500
Turn-off time	800 μs	600 μs	800 μs
Resonant Inductor	8.9 mH (x6)	12.6 mH (x6)	8.9 mH (x6)
Resonant Capacitor	70 μF (x3)	44 μF (x3)	70 μF (x3)
Peak Input Current (disc. mode)	750 A	500 A	750 A
Max. Switch Frequency	208 Hz	278 Hz	208 Hz
MV DC Capacitor	36.4 μF	23 μF	36.4 μF
Series Connected thyristors per valve	11	16	8
Thyristor utilization	0.15%	0.1%	0.21%

4.2.2 3-Phase Converter Losses

4.2.2.1 Switch Losses

Calculating the losses will be performed similarly to the single phase converter. The voltage at turn-on and turn-off (V_{OFF}) will be given by (D90) in the continuous mode and by ($V_2/2+V_1/4$) in the discontinuous mode. In discontinuous mode, the rate of change of current at turn-on can be obtained from (D1) and (D41). The slope at turn-on and turn-off in continuous mode will be estimated based on (D60) and (D61) as $V_2/2L$. Similarly to (55) and (56), the turn-on losses for the six thyristor switches per cycle will be:

$$W_{turn-on} = 6\left(\frac{V_{OFF}}{6} s_i t_{v0}^2\right) \tag{70}$$

and the turn-off losses for each switch per cycle will be given by:

$$W_{RR} = 6\left(Q_{RR} V_{OFF} - \frac{I_{rr}^2 V_{OFF}}{2s_i}\right) \tag{71}$$

The on-state losses in discontinuous mode per cycle will be given by:

$$\begin{aligned} W_{ONdisc} &= 2\cdot 6\int_0^{T_0/2}\left(\frac{\frac{V_2}{2}+\frac{V_1}{4}}{2Z_0}\sin(\omega_0 t)\right) n_{sw}\left(V_{T0} + r_T\frac{\frac{V_2}{2}+\frac{V_1}{4}}{2Z_0}\sin(\omega_0 t)\right)dt \\ &= 12 n_{sw}\left(V_{T0}\left(\frac{V_2}{2}+\frac{V_1}{4}\right)C_r + r_T\left(\frac{\frac{V_2}{2}+\frac{V_1}{4}}{2Z_0}\right)^2\frac{T_0}{2}\right) \end{aligned} \tag{72}$$

where n_{sw} is the number of thyristors per switch. The losses are multiplied by a factor of two since there will be two current pulses in each switch per cycle. The on-state losses in continuous mode will be estimated by considering the current in each switch over 1/3rd of a cycle as that shown in Figure 31.

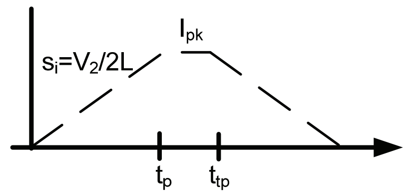

Figure 31: Estimated current waveform in continuous mode operation.

I_{ave} in Figure 31 is given by (D88). When $t_p<T_s/3$, then the peak current can be estimated as equal to the average current and the time $(t_{tp}-t_p)$ will be given by $T_s/3-t_p$. When $t_p>T_s/3$, then the peak current will be less than the average input current and the time t_p will be estimated as $T_s/3$ and $(t_{tp}-t_p)$ as $2LI_1/V_2-T_s/3$. The on-state losses will be:

$$W_{ONcont}=6n_{sw}\left[2\int_0^{t_p}\frac{V_2}{2L}t\left(V_{T0}+r_T\frac{V_2}{2L}t\right)dt+\int_{t_p}^{t_{tp}}I_{ave}\left(V_{T0}+r_TI_{ave}\right)dt\right]$$

$$=6n_{sw}\left[\frac{V_2}{2L}V_{T0}t_p^2+\left(\frac{V_2}{2L}\right)^2 2r_T\frac{t_p^3}{3}+I_{ave}V_{T0}\left(t_{tp}-t_p\right)+r_TI_{ave}^2\left(t_{tp}-t_p\right)\right] \tag{73}$$

The discontinuous mode off-state losses per cycle can be evaluated from Figure D-6 and using (D46), (D48), and (D51), so that:

$$W_{OFFdisc}=6\frac{I_{leak}}{n_{sw}V_{thy}}\left[\left(2\left(\frac{V_2}{2}+\frac{V_1}{4}\right)^2+2\left(\frac{V_2}{2}-\frac{V_1}{4}\right)^2+\left(\frac{V_1}{2}\right)^2\right)\left(\frac{T_s}{6}-\frac{T_0}{2}\right)+\right.$$
$$\left.+\left[\left(\frac{3V_2}{4}-\frac{V_1}{8}\right)^2+\left(\frac{3V_2}{4}+\frac{7V_1}{8}\right)^2\right]\frac{T_0}{2}+2\left(\left(\frac{V_1}{4}\right)^2\frac{T_0}{2}+\left(\frac{V_2}{4}+\frac{V_1}{8}\right)^2\frac{T_0}{4}\right)\right] \tag{74}$$

To estimate the off-state losses during continuous mode operation, the voltage during the off-state will be assumed to vary linearly between $\pm V_{OFF}$ (given by (D90)). The current will be assumed to vary as in Figure 31. Therefore the off-state losses over one cycle will be approximately:

$$W_{OFFcont}=6\int_0^{t_{off}}V_{OFF}^2(t)\frac{I_{leak}}{n_{sw}V_{thy}}dt=6V_{OFF}^2t_{off}\frac{I_{leak}}{nV_{thy}} \tag{75}$$

where t_{off} is equal to T_s–($2t_p$+t_{tp}). Therefore using (70)-(75), the switching losses over the entire converter operation can be evaluated. The thyristor power loss will be given by:

$$P_{thy} = \left(W_{turn-on} + W_{RR} + W_{ON} + W_{OFF}\right)f_s \tag{76}$$

The thyristor parameters used for this evaluation are evaluated from the datasheet, similar to Section 4.1.3.

The diode losses will include the on-state losses and off-state losses. Similarly to the single-phase resonant converter, the diode reverse recovery losses can be ignored if the inductor is small. The on-state losses during discontinuous mode can be evaluated since the current into the HV terminal will be equal to half the input current (shown in Figure D-5). Considering that there are two current pulses in each diode per cycle, then using the analysis in Appendix D.1, the total on-state losses per cycle will be:

$$\begin{aligned} W_{ONdisc\_diode} &= 12\int_{t_{2cond}}^{t_s/6} \frac{1}{2} I_L(t)\left(V_{F0} + r_F \frac{1}{2} I_L(t)\right)dt \\ &= 12\left[\frac{1}{2\omega_0} V_{F0} I_{pkdisc}\left(1+\cos(\omega_0 t_{2cond})\right) + \frac{1}{4} r_F I^2_{pkdisc}\left(\frac{1}{2}\left(\frac{T_0}{2} - t_{2cond}\right) - \frac{1}{4\omega_0}\sin(2\omega_0 t_{2cond})\right)\right] \end{aligned} \tag{77}$$

The off-state voltage drop across the diodes will change from $-V_2$ to (V_2/2+3V_1/4) to zero, and from zero to (V_2/2-3V_1/4) to V_2. Summing the different voltage drops over one cycle, then the total off-state losses per cycle in discontinuous mode operation will be:

$$W_{OFFdisc\_diode} = 6\int_0^{T_s} \frac{V^2_{OFFdiode}}{n_d V_{diode}} I_{leak} dt = 6\frac{V^2_{OFFdiode}}{n_d V_{diode}}\left(3\frac{T_s}{6} + \frac{T_0}{2} - t_{2cond}\right) I_{leak} \tag{78}$$

The continuous mode diode current will be estimated using the approximation of a constant input current. In each cycle, current will flow into the HV terminal at time t_{2cond}, with an approximate current of $I_1/2$. After switching, the current will decrease with a slope of $V_2/2L$. Considering there are two current pulses in each diode per switching cycle, the on-state diode losses will be:

$$\begin{aligned} W_{ONcont\_diode} &= 12\left[\int_{t_{2cond}}^{T_s/6}\left(\frac{I_1}{2}\right)\left(V_{F0} + r_F\frac{I_1}{2}\right)dt + \int_0^{I_1\frac{2L}{V_2}}\left(\frac{I_1}{2} - \frac{V_2}{2L}t\right)\left(V_{F0} + r_F\left(\frac{I_1}{2} - \frac{V_2}{2L}t\right)\right)dt\right] \\ &= 12\left[\left(\frac{I_1}{2}V_{F0} + r_F\left(\frac{I_1}{2}\right)^2\right)\left(\frac{T_s}{6} - t_{2cond}\right) + \frac{V_{F0}}{2}\left(\frac{I_1}{2}\right)^2\left(\frac{2L}{V_2}\right) + \frac{r_F}{3}\left(\frac{I_1}{2}\right)^3\left(\frac{2L}{V_2}\right)\right] \end{aligned} \tag{79}$$

During the continuous mode, the diode voltage drop will change from $-V_2$ to zero and from zero to $-V_2$. Approximating the rate-of-change of voltage to be constant, then the continuous mode off-state diode voltage loss will be:

$$W_{OFFcont\_diode} = 6\frac{V_2^2}{n_d V_{diode}}\frac{T_s}{2}I_{leak} \quad (80)$$

The thyristor losses of the converter in continuous mode operation are shown in Figure 32. Note that the losses close to the border between the continuous and discontinuous modes show a non-linearity since the estimation used in Appendix D.2 of a constant input current is not accurate in this region.

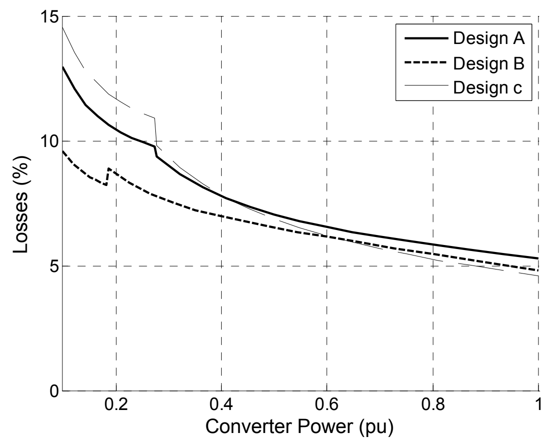

Figure 32: 3-phase converter continuous mode losses.

As can be seen, Design B has lower losses than the other designs (and slightly less than the single phase converter designs in Section 4.1.2), but this will require high component ratings. Similarly to the single phase converter, the main sources of full load losses are due to on-state losses and reverse recovery losses. Methods to reduce reverse recovery loss include:

- *Reduce di/dt*—this can be reduced by increasing the size of the resonant inductor (or effectively by decreasing the maximum discontinuous mode current). Adding thyristors in parallel will also decrease the switch *di/dt* but will result in increased number of switches and in increased off-state losses.
- *Using fast turn-off thyristors*—these thyristors have low turn-off losses but higher on-state voltage drops which will increase the on-state losses.

Design methods to reduce on-state losses include:

- *Reduce on-state current*—the on-state current can be reduced by adding thyristors in parallel, but will result in higher number of switches and higher off-state losses. In addition, this will only reduce the on-state current due to the on-state resistance (r_T) and losses due to the on-state voltage (V_{T0}) will not decrease, therefore adding more than two in parallel will not greatly decrease these losses.
- *Reduce on-state peak current*—the on-state peak current can be reduced by increasing the size of the resonant inductor (or effectively by increasing the switch turn-off time).
- *Using low on-state voltage drop thyristors*—thyristors rated for higher currents generally have lower on-state voltage drops; however, these switches often have higher switching losses and turn-off times.

Similarly to the single phase converter, using a higher voltage turbine will lower the converter losses. The losses of Design A and of a design using the same type of switches but with a wind turbine with an output voltage of 4000 V is shown in Figure 33.

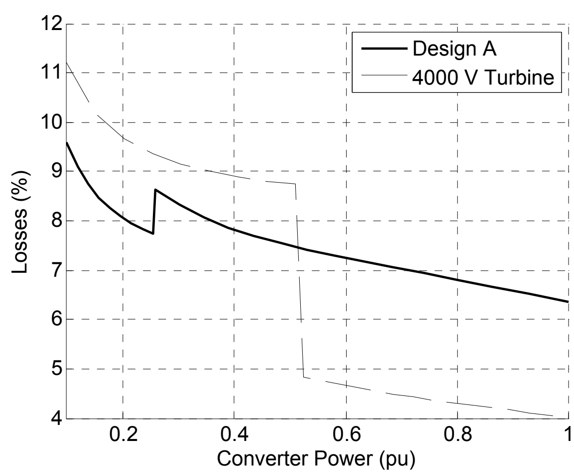

Figure 33: Comparison of losses for designs using 1000 V and 4000 V turbines.

In addition, the switch utilization increases from 0.15% to 0.68%. The 4000 V turbine design in Figure 33 was designed to have similarly sized resonant inductors. Lower losses of less than 2% can be achieved if the inductor size is increased.

4.2.2.2 Resonant Capacitor Losses

The maximum capacitor voltage will be given by (D85) and therefore the capacitors need to be rated for around 23.7 kV (peak). If the capacitor losses are evaluated similar to those in

Section 4.1.3 by assuming sinusoidal waveforms, and assuming that the peak capacitor current is equal to the peak switch current, then the maximum capacitor losses will be:

$$P_{cap} = 3 \cdot 0.0001\left(\frac{V_c}{\sqrt{2}}\frac{I_{pk}}{\sqrt{2}}\right) = \frac{3 \cdot 0.0001}{2}\left(\frac{V_2}{2}\frac{V_2}{6Lf_s}\right) = \frac{0.0001}{8}\left(\frac{V_2^2}{Lf_s}\right) \tag{81}$$

This results in losses of 0.13% at full load for both designs A and B.

4.2.2.3 Resonant Inductor Losses

Using the same design method as in Section 4.1.3, using a maximum average current through each inductor of 1/3rd the average input current, a maximum voltage of V_2, and a maximum input current given in Table 12. If a Raleigh distribution is used to estimate the wind variation, the expected conductor losses in an inductor will be given by:

$$P_{cond} = \int_4^{25} P_L(U)\frac{\pi}{2}\left(\frac{U}{\overline{\overline{U}}}\right)e^{-\frac{\pi}{4}\left(\frac{U}{\overline{\overline{U}}}\right)^2} dU \tag{82}$$

where $P_L(U)$ is the estimated inductor conduction losses for each wind speed. In discontinuous mode, the conduction losses as a function of the switching frequency will be:

$$P_{Ldisc} = 2\int_0^{T_0/2}\left(\frac{\frac{V_1}{2}+\frac{V_2}{4}}{2Z_0}\sin(\omega_0 t)\right)^2 \rho_L dt \cdot f_s = \left(\frac{\frac{V_1}{2}+\frac{V_2}{4}}{2Z_0}\right)^2 \frac{1}{2f_0}\rho_L f_s \tag{83}$$

where ρ_L will be calculated using the minimization function described in Appendix B.3 and f_s is a function of the power using (D38), which can be a function of the wind speed using (B6). In continuous mode, the converter current will be assumed to be similar to Figure 31 and will be given by:

$$P_{Lcont} = \left[2\int_0^{t_p}\left(\frac{V_2}{2L}t\right)^2 dt + \int_{t_p}^{t_{tp}}(I_{ave})^2 dt\right]\rho_L f_s = \left[\frac{2}{3}\left(\frac{V_2}{2L}\right)t_p^3 + I_{ave}^2\left(t_{tp}-t_p\right)\right]\rho_L f_s \tag{84}$$

where I_{ave} is the converter input current (P/V_1) and f_s can be obtained in terms of the converter power from (D88). Similarly to the single phase converter, the core losses in each inductor (if required) will be equal to:

$$P_{core} = \frac{1}{2}kB^{\beta} f_{eff}^{\alpha} \cdot \frac{f_s}{f_{eff}} M_{core} \tag{85}$$

where f_{eff} is the effective frequency, based on a period equal to twice the length of a current pulse, and the flux density is:

$$B = \frac{\mu_0 n I_{peak}}{l_g} \tag{86}$$

The peak current and effective frequency can be estimated based on the switching frequency, using similar assumptions as were used for the conduction losses.

Therefore evaluating the expected losses for a wind turbine in an area with an average wind speed of 8 m/s and designing air core inductors using the process described in Appendix B.3, then the resulting inductor parameters are shown in Table 13. Using a higher current density will reduce the cost of the copper, but result in higher current losses.

Table 13: 3-phase converter inductor design for a 1.72/33 kV, 3 MW DC-DC converter.

	Design A and C	Design B
Inductance (L)	8.9 mH	12.6 mH
Core length (l_c)	1.56 m	1.6 m
Core diameter (d_c)	1.1 m	1.13 m
Conductor size (w_{cui}xl_{cu})	198x2603 mm^2	188x2658 mm^2
Conductor weight (M_{cu})	4857 kg	5178 kg
Ave. current density	0.9 A/mm^2	1 A/mm^2
Number of turns (n)	212	250
Expected efficiency	99.5%	99.5%

The inductor efficiency over the whole converter operation for all six inductors is plotted in Figure 34. Note that the non-linearities are due to an inaccurate model at the border of the continuous and discontinuous operating regions.

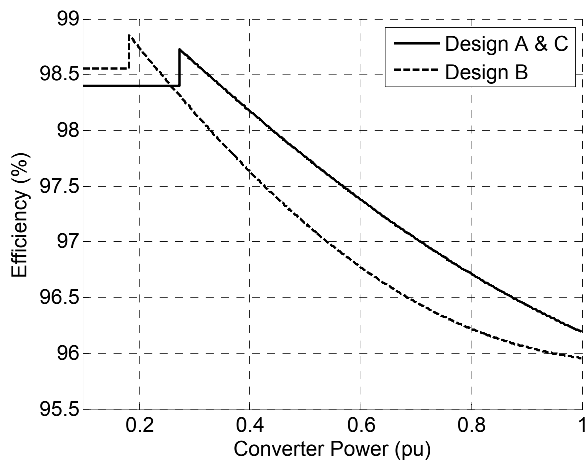

Figure 34: 3-phase converter combined efficiency for the 6 resonant inductors.

As can be seen in Figure 34, the efficiency drops for high converter powers, except near the maximum power, where the peak current decreases. If required, the weight of the inductors in both designs can be reduced, but will result in even lower efficiencies due to an increased average conductor current density.

4.3 HV DC-DC Converter

This section will use similar design procedures as were used in Section 4.1 to design HV converters for connecting a 33 kV DC bus to a 500 kV HVDC line. The power rating of the converters will be designed for 300 MW.

4.3.1 Single Phase HV Resonant Converter

A 300 MW single phase resonant converter will require components with a high average current and therefore may require parallel thyristors. Three designs will be compared, Design A will use ABB 45Q2800 thyristors, Design B will use ABB 34Q5200 thyristors, and Design C will use ABB 42U6500 thyristors.

Following the single phase converter design procedure in Section 4.1.2, the resulting converter designs are shown in Table 14. Note that the peak current and maximum rate of change of current is for the individual thyristors, not the inductor. The peak inductor current is estimated as twice the peak current of the thyristors when there are two parallel switches.

Table 14: HV Converter design components for a 33/500 kV, 300 MW wind farm DC-DC converter.

	Design A	Design B	Design C
Switch Model	ABB 45Q2800	ABB 34Q5200	ABB 42U6500
Turn-off time	400 µs	700 µs	1600 µs
Parallel rows of thyristors	1	2	2
Series connected thyristors per valve	358	193	154
Total Thyristors	1432	1544	1232
Resonant Capacitor (C_r)	6.5 µF	11.3 µF	26.5 µF
Resonant Inductor (L_r)	8.3 mH	14.3 mH	35.4 mH
Resonant Frequency	685 Hz	395 Hz	164 Hz
Maximum Switch Frequency	653 Hz	375 Hz	160 Hz
Peak Current	14.9 kA	7.5 kA	7.3 kA
Max. Rate of Change of Current (s)	64.2 A/µs	18.6 A/µs	73.1 A/µs
Input Capacitor	4.2 mF	7.3 mF	17.1 mF
Output Capacitor	17.9 µF	31.2 µF	39.3 µF
LV Rated (V_1)	33 kV	33 kV	33 kV
HV Rated (V_2)	500 kV	500 kV	500 kV

The converter losses are shown in Figure 35.

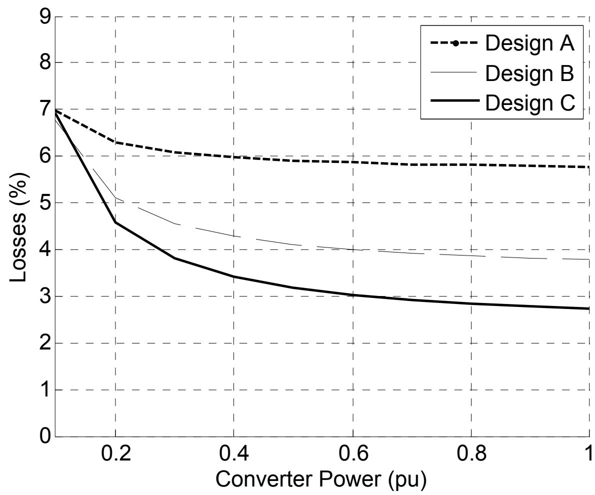

Figure 35: HV converter losses for a 500 kV HVDC line.

Similar to the single phase converter example, the losses can be reduced if the required converter gain is lower. For example, if the HVDC line will be 350 kV instead of 500 kV, then the thyristor losses will be as shown in Figure 36.

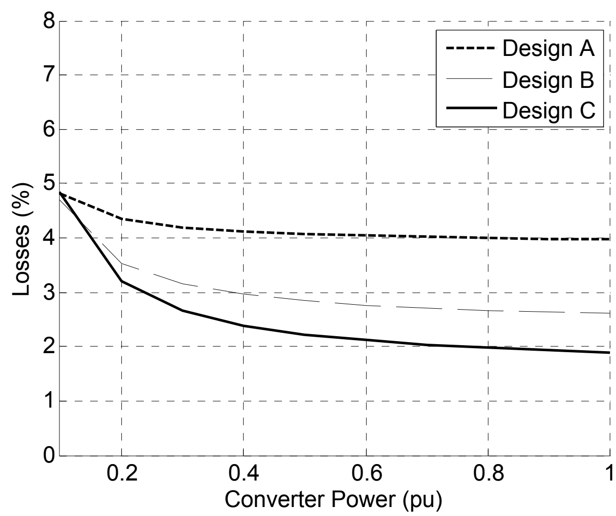

Figure 36: HV converter losses for a 350 kV HVDC line.

4.3.1.1 HV Single Phase Inductor Design

Using the same design approach as in Section 4.1.3, the resulting inductor properties for an air-core toroidal inductor are shown in Table 15. Note that the current density was fixed at 4 A/mm^2, higher efficiencies can be obtained for lower current densities but will increase the weight of the conductor.

Table 15: HV single phase air core inductor design for a 33/500 kV, 300 MW DC-DC converter.

	Design A	Design B	Design C
Inductance (L)	8.3 mH	14.3 mH	35.4 mH
Core Length (l_c)	2.57 m	2.86 m	3.4 m
Core Diameter (d_c)	1.82 m	2.02 m	2.4 m
Conductor size (w_{cu}xl_{cu})	145x2043 mm^2	137x1920 mm^2	137x1920 mm^2
Conductor Weight (M_{cu})	4 A/mm^2	4 A/mm^2	4 A/mm^2
Ave. current density	21579 kg	29908 kg	51521 kg
Number of Turns (n)	160	199	285
Expected efficiency	99.7	99.6	99.3

4.3.2 3-Phase HV Resonant Converter

Similar analysis for the 3-phase resonant converter as in Section 4.2 using a 300 MW converter with a maximum discontinuous mode input current of 3 kA, results in converter designs shown in Table 16. Note that parallel connected thyristors are not required since the average current will be lower (around 3 kA at full load), but can be used to decrease losses.

Table 16: 3-phase HV converter designs for a 33/500 kV, 300 MW wind farm DC-DC converter.

	Design A	Design B	Design C
Switch Model	ABB 45Q2800	ABB 42U6500	ABB 34Q5200
Turn-off time	400 μs	800 μs	700 μs
Resonant Inductor	40 mH (x6)	80 mH (x6)	70 mH (x6)
Resonant Capacitor	7.5 μF (x3)	15 μF (x3)	13 μF (x3)
Peak Input Current (disc. mode)	1750 A	1750 A	1750 A
Max. Switch Frequency	417 Hz	208 Hz	238 Hz
HV Capacitor	4.9 μF	9.8 μF	8.6 μF
Parallel rows of thyristors	1	1	2
Series connected thyristors per valve	358	154	193
Total thyristors	2148	924	2316

The thyristor losses for the different converter designs are shown in Figure 37.

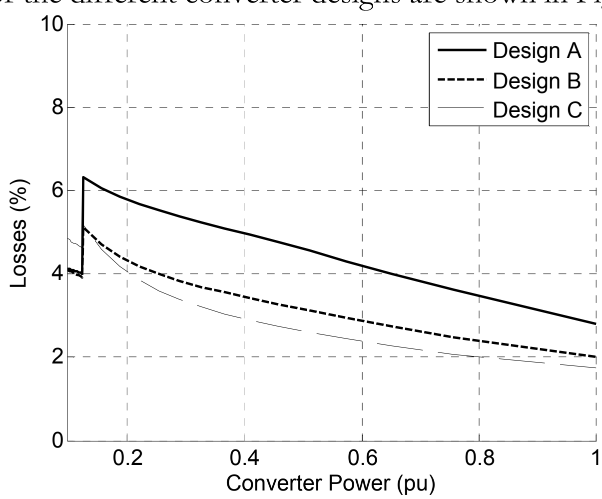

Figure 37: HV 3-phase converter losses for a 500 kV HVDC line.

From comparing Figure 35 and Figure 37, better losses can be obtained using the 3-phase converter, but this will require higher passive component ratings and a higher number of passive components. The efficiency of the six inductors is also lower, as shown in Figure 38.

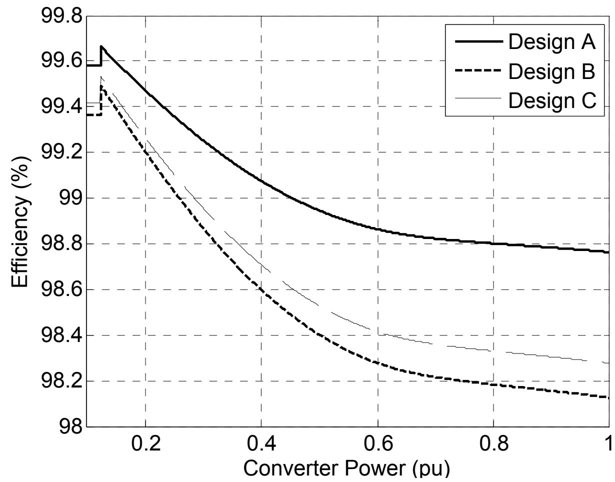

Figure 38: HV 3-phase converter efficiency of the six inductors.

4.4 Cable Design

Standards documenting the cable design, current rating, and losses include IEEE 835-1994 and IEC 60287. Cable losses depend on the conduction losses and dielectric losses. Conduction losses will depend on the cross sectional area of the conductor, the current, and the proximity and skin effects. Dielectric losses occur when the line is energized, and depend on the type of insulation and are related to the square of the voltage. Although dielectric losses are important for HV cables, they can be ignored for most MV levels (less than 63.5 kV for filled XLPE cables [15]). Assuming that the yearly cost of the cable is a direct function of the conductor size, the optimal cable cross sectional area can be chosen using *Kapp's rule*, which states that the optimum conductor size is one where the yearly costs of losses is equal to the yearly costs of the cable [15].

Designing the optimum conductor size will require detailed information on the installation and cable costs, and therefore this section only outlines the design trade-offs between AC and DC cables, comparing cable designs for 33 kV AC and DC grids which have equal losses. Example datasheet information for buried 33 kV XLPE aluminum and copper cable is in Table 17.

Table 17: General Cable 33 kV XLPE armoured aluminum and copper cable information [71,72].

	33 kV 3-Conductor Cable				22 kV 1-Conductor Cable			
Conductor Material	Copper		Aluminum		Copper		Aluminum	
Cond. area (mm^2)	70	120	70	120	150	240	150	240
No. of strands	19	19	19	19	19	37	19	36
Overall diameter (mm)	71.7	78.9	71.7	78.9	35.3	39.6	35.3	39.6
Mass (kg/km)	5000	6950	3900	4700	2900	3920	1970	2370
Rated Current (A) (30˚C, buried in ducts)	240	320	187	249	367	455	298	375
DC Resistance (Ω/km)	0.268	0.153	0.443	0.253	0.124	0.075	0.206	0.125
Eq. Star Reactance (Ω/km)	0.135	0.122	0.135	0.122	0.120	0.111	0.120	0.111
Star Capacitance (μF/km)	0.16	0.19	0.16	0.19	0.25	0.30	0.25	0.3
Fault Rating (kA)	10	17.2	6.6	11.3	21.5	34.3	14.2	22.7

Note that the ratings will vary depending on the temperature, and thermal resistivity of the soil.

The rated current may be higher for cable not buried in ducts, since ducts generally have poorer heat transfer, and require larger cross sectional areas to meet the cable thermal requirements.

Considering a star-connected wind farm of 100x3 MW wind turbines with individual MV transformers, then each AC MV cable must be rated for a full load current of 52.4 A (for a summary of wind farm topologies see Figure 9). As can be seen from Table 17, copper cables will have lower resistivity but higher weight (although aluminum cables would require more insulation due to the larger surface area). For 70 mm^2 aluminum and copper cables, the charging current (given by $2\pi fCV_{ph}$) will be 6-7 A (assuming an average cable length from the wind turbine to the HV converter of 3 km), and therefore the total current will be well within the cable current margin (smaller cables could be used but would result in higher conduction losses).

If the DC cables will be designed to achieve equal losses to AC cables, then:

$$P_{loss} = 3I_L^2 R_{AC} = 2I_{DC}^2 R_{DC} \tag{87}$$

and:

$$V_{DC} = V_L \sqrt{\frac{2R_{DC}}{R_{AC}}} \tag{88}$$

If the DC voltage is equal to the AC rms voltage, then R_{AC} should be equal to $2R_{DC}$ to achieve equal losses (ignoring charging current and dielectric losses). Based on IEC 60287, the AC and DC resistance will be similar and therefore assuming the AC design uses 70 mm^2 copper cables and 120 mm^2 aluminum cables, then the DC design would require 150 mm^2 copper cables and 240 mm^2 aluminum cables. Full load losses are around 0.2% (considering an average cable length of 3 km). A comparison in terms of the overall weight and minimum duct area for the AC and DC designs (considering one 3-core 33 kV AC cable and two 1-core 22 kV DC cables) is shown in Table 18.

Table 18: AC and DC cable comparison (based on data from Table 17).

	33 kV AC Cables		22 kV DC Cables	
Conductor material	70 mm^2 copper	120 mm^2 aluminum	150 mm^2 copper	240 mm^2 aluminum
Total weight (kg/km)	5000	4700	5800	4740
Min. duct area (mm^2)	4038	4890	3915	4927

As can be seen from Table 18, despite having a lower number of conductors, the DC cables should have a larger conductor to achieve similar cable losses, resulting in a higher total DC cable weight. It should be noted that the DC cables are rated for a higher voltage than required (the maximum voltage would be +/- 16.5 kV). The minimum duct area is similar for both the AC and DC cables.

CHAPTER 5: SYSTEM INTEGRATION

This section outlines integration issues and benefits of DC and AC wind farm topologies when connecting to an HVDC line. The efficiency analysis in Chapters 3 and 4 shows that out of the designs evaluated, the NPC VSC design and the single phase resonant converter designs may have the most potential (a summary will be given in Chapter 6). Therefore, the systems studied in this section connect a 300 MW wind farm using a DC grid with single phase resonant DC-DC converters and using an AC grid with 3-level NPC voltage source converters. A description is given of the PSCAD models for the two systems, converter controller designs, and the various system conditions that will be studied.

The results are evaluated based on the ability to effectively deliver power from the wind farm to an HVDC line under normal conditions, and to isolate and prevent fault propagation during grid faults. This section does not consider all aspects of the control and protection of the wind farms, but highlights issues that will need further study for the AC and DC systems.

5.1 System Models

Each area is connected using either an AC transformer and VSC converter or a DC-DC converter. The wind turbines considered will use variable speed permanent magnet synchronous generators. The AC and DC systems studied are shown in Figure 39.

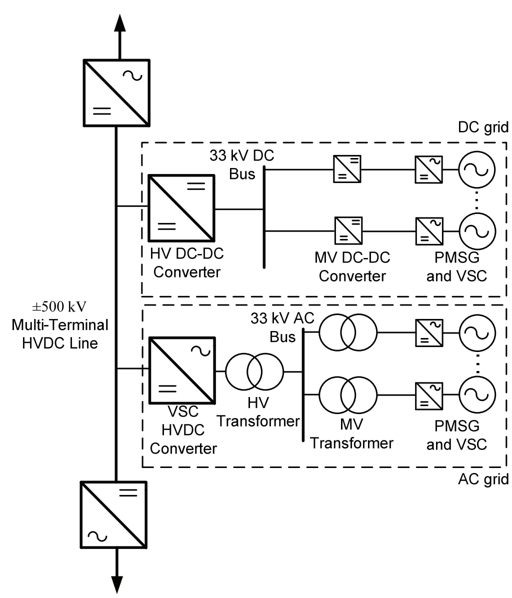

Figure 39: Single line diagram of AC and DC systems.

The performance with both LCC HVDC lines and VSC HVDC lines will be compared. Since much research has already been performed on the control and operation of permanent magnet wind turbines and on both types of HVDC lines, then analysis will focus on the operation of the MV grid, using simplified models for the wind farm and HVDC line. The simplified models of the MV AC and DC buses are in Figure 40.

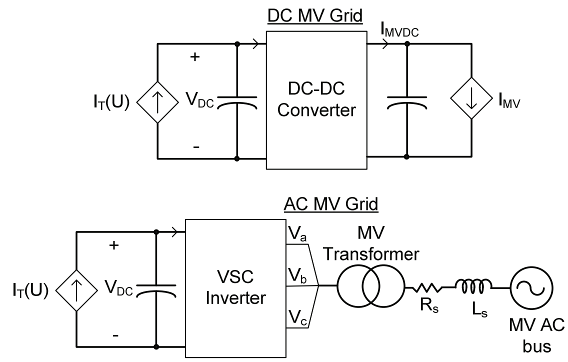

Figure 40: MV grid wind turbine converter models.

The models of the DC-DC converter and VSC inverter have been detailed in Sections 3.1.2 and 4.1. The controller design for the converters is detailed in Section 5.2.

Modelling the HV connection to the HVDC line will require an aggregate model of the 300 MW wind farm. To test the operation of the HVDC converters for the wind farm, as well as to test interactions between the HV converter and the MV converters, two of the 100 turbines will be modelled using the MV grid models in Figure 40 and the other turbines will use an aggregated model. The DC grid will use a controllable current source, with a similar controller to that shown in Figure 44. The AC grid will use a Norton equivalent model with a controllable current source and impedance representing the transformer. As outlined in [73], the current source model may result in problems simulating faults close to the converter terminal since the active and reactive currents may not be distinguishable. Since the aggregated wind farm model will only be used to investigate faults on the MV bus, then this model will be appropriate for these tests. The resulting HV models are shown in Figure 41.

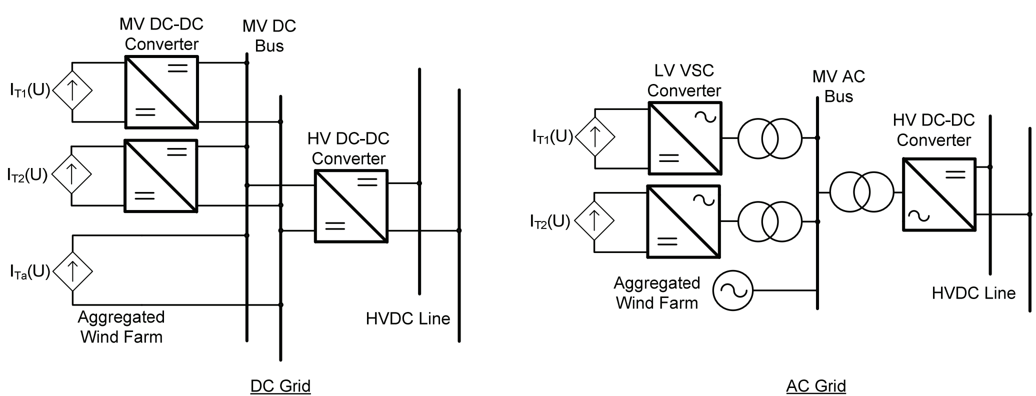

Figure 41: HVDC integration models.

A simplified model of the HVDC line using a controlled voltage source will be used during the simulations.

5.2 Controller Design

The converter controllers will be designed to operate over the whole range of the wind turbines, ramp up the voltage during startup, and isolate and protect against faults.

5.2.1 DC Controller Design

The wind turbine will be modelled assuming a VSC based generator side rectifier (as in Figure 7a), a constant DC voltage, and used to control the power from the synchronous generator to obtain maximum power point tracking. Simplifying the permanent magnet synchronous generator VSC control in [4], where the DC current is controlled based on the wind speed, the simulation will model a wind turbine using a controlled DC current source as shown in Figure 44.

During a MV DC bus fault, the MV capacitor and the resonant capacitor will discharge through the diode bridge. If the thyristors continue to be switched after the MV capacitor voltage has dropped below the voltage of the LV side, then the thyristors will not turn off and control will be lost. This will lead to resonance between the LV DC capacitor and the resonant inductor, causing the voltage to resonant between $\pm V_{DC}$, depending on the damping. The resonant circuit is shown in Figure 42.

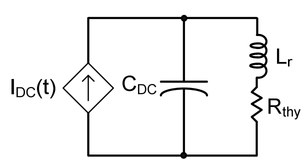

Figure 42: Resonant circuit after a MV fault and loss of control.

The fault will also propagate to the LV AC grid and will require tripping the wind turbine. In order to prevent this disturbance, the voltage level across the MV capacitor should be measured to allow the fault to be detected and to stop the switching of the converter thyristors before the voltage has dropped below that of the LV side. Rather than increasing the size of the MV inductor, which will lead to higher switching losses in the diodes, a second inductor will be placed on the MV DC terminal as shown in Figure 43.

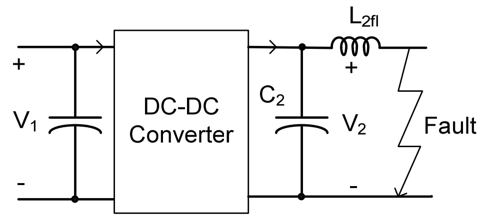

Figure 43: Fault current limiting inductor on the MV terminal.

To avoid turning off the converter due to a voltage dip, then an undervoltage relay will be set for 75% of V_{nom}. The inductor will be sized so that the time for the voltage to drop to 50%V_{nom} for a fault when operating at full load is equal to 1.5x the period of the resonant converter. Since the current from the converter will be pulsed, then the inductor will be sized considering I_2 from the converter as zero. Therefore the MV capacitor voltage will be:

$$V_{MV}(t) = V_{MV0}\cos(\omega_{MV}t) - I_{MV0}Z_{MV}\sin(\omega_{MV}t) \tag{89}$$

where ω_{MV} and Z_{MV} are the resonant frequency and impedance of the MV capacitor (C_2) and inductor (L_{2fl}).

The additional inductor will create a low pass LCL filter, but could also lead to resonance with the other capacitances and inductances on the MV grid. This oscillation may be difficult to damp using the converter controllers and will therefore be damped using a parallel resistor, similar to that proposed in [74].

Once the converter has stopped switching, the voltage across the LV capacitor will start to rise, depending on the output of the wind turbine. This problem has been dealt with for full converter based wind turbines in ac grids and methods of minimizing the DC overvoltage include adjusting the pitch angle of the wind turbine, absorbing energy in the inertia of the machine, adjusting the control strategy to maximize active power injection into the grid, increasing the size of the DC capacitor, using a breaking resistor to absorb excess energy from the wind turbine, or a combination of the different methods. In [73] it is shown that this method can simplify analysis of a full converter wind turbine, allowing the reactive power responses of the generator and grid side converters to be decoupled and grid fault analysis to be performed without a detailed generator model. Since these methods have been studied in detail and are not the focus of this thesis, then a full power breaking resistor will be considered. For simplification, an ideal breaking resistor is used, but in practice the dissipated energy will need to be limited depending on the rating of the resistor. Typically the voltage is limited to 125% of the rated voltage [73]. The wind turbine control is shown in Figure 44.

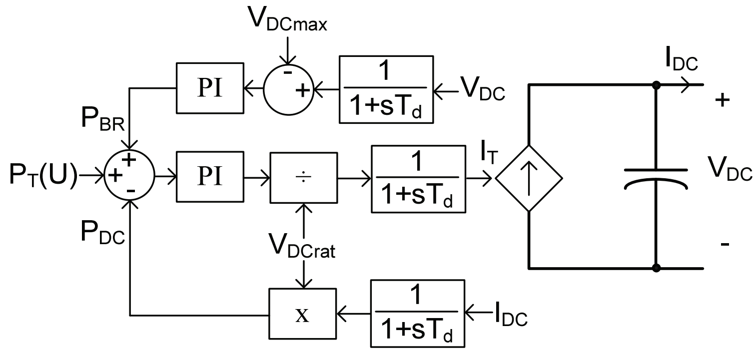

Figure 44: Simplified wind turbine and VSC rectifier model.

$P_T(U)$ is the power from the wind turbine as a function of the wind speed, given by (B6), and P_{BR} is the power absorbed by the breaking resistor. Time delays were added to represent measurement delays and delays in the generator side VSC converter. The maximum voltage was set to be 120% of the rated voltage. If a better response is required, then a faster controller can be used for the breaking resistor.

As developed in Section 4.1, the power through the DC-DC converter is controlled by varying the switching frequency. The controller for the DC-DC converter is in Figure 45.

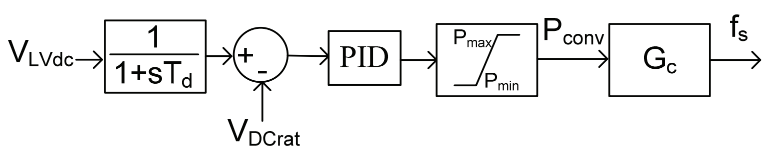

Figure 45: DC-DC converter controller.

G_c is based on (39) and f_s is the switching frequency. The derivative control is added to reduce the peak current when ramping up the voltage on the DC bus. The converter for the HV DC-DC converter will have a similar controller, with an added control to disable switching when the voltage on the MV bus is ramping up.

Faults on the HVDC line are a more difficult problem for the HV DC-DC converter. Similar to the MV converter, the converter must stop operation before the voltage on the HVDC line has fallen or it will lead to a loss of control and the fault will propagate onto the MV bus. This will also lead to resonance between the MV DC capacitor and the HV resonant inductor, similar to that shown in Figure 42. Stopping the LV converters and absorbing the wind turbine energy in the LV breaking resistors (as for a MV fault) will reduce the overvoltage; however, the current in the inductors of the MV grid will continue to draw current from the MV capacitors of the wind turbine DC-DC converters, causing the voltage to drop and possibly leading to instability (depending on the power level of the wind farm before the fault). Despite the high power requirements of using a breaking resistor on the MV grid to absorb the energy of the wind farm during a fault, this solution may be the most practical as custom commercial resistors are available in the MJ range [75] and this will minimize the disturbance of the wind farm grid and the time to reconnect the wind farm. The controller will be similar to that described for the MV converter, but the limits will be scaled for the MV bus voltage.

For transient faults on an LCC HVDC line, generally the charge on the line is dissipated by operating the end converters as inverters, and then repowering the line after around 200 ms [27]. During this time, the MV breaking resistor would have to absorb the excess wind energy, which at full load will be around 60 MJ.

For the aggregated wind turbine model, a similar control will be used as shown in Figure 43, but a simplified model will be used that approximates the converter using a controllable current source and the HV side inductors and capacitors, shown in Figure 46.

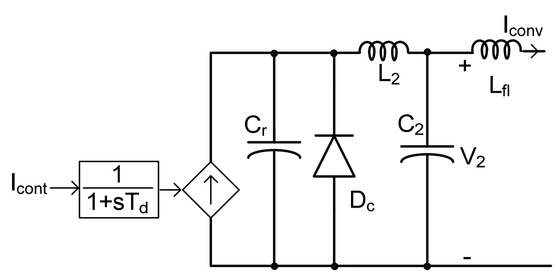

Figure 46: Simplified wind turbine circuit model.

After a fault on the HV side, the resonant capacitor and HV side capacitor will discharge into the fault and current will flow through the HV diodes until the fault is cleared. This effect is modelled by placing a diode in parallel with the HV side capacitor (see Figure 46). For an aggregated model, multiple converters will be connected in parallel, which together can be modeled using a Norton equivalent circuit, representing the combined current from the converters as a controllable current source with a Norton equivalent impedance, given by:

$$Z_{eq} = \left(\left(\frac{1}{sC_r} + sL_2 \right) \| \frac{1}{sC_2} + sL_{fl} \right) \Bigg\| \ldots \Bigg\| \left(\left(\frac{1}{sC_r} + sL_2 \right) \| \frac{1}{sC_2} + sL_{fl} \right) = \frac{1}{n_T} \left(\left(\frac{1}{sC_r} + sL_2 \right) \| \frac{1}{sC_2} + sL_{fl} \right) \quad (90)$$

where n_T is the number of aggregated wind turbines. The Norton current is given by:

$$I_{eq} = \left(I_{conv,1} + \ldots + I_{conv,n} \right) \left(\frac{\frac{1}{sC_r}}{sL_2 + \frac{1}{sC_r} + \frac{1}{sC_2} \| sL_{fl}} \right) \left(\frac{\frac{1}{sC_2}}{sL_{fl} + \frac{1}{sC_2}} \right) = \frac{\left(I_{conv,1} + \ldots + I_{conv,n} \right)}{s^4 L_2 L_{fl} C_r C_2 + s^2 \left(L_2 C_r + L_{fl} C_r + L_{fl} C_2 \right) + 1} \quad (91)$$

Since the capacitors and inductors will normally be small, then the poles in (91) will be very high frequency and can be ignored so that:

$$I_{eq} = \left(I_{conv,1} + \ldots + I_{conv,n} \right) \quad (92)$$

After a fault on the MV bus that causes the voltage to drop and the capacitors to discharge, then the HV side diodes (D_1-D_4) will conduct until the energy in the converter inductors has discharged. The equivalent impedance will therefore be given by:

$$Z_{eq} = \left(sL_2 \| \frac{1}{sC_2} + sL_{fl} \right) \Bigg\| \ldots \Bigg\| \left(sL_2 \| \frac{1}{sC_2} + sL_{fl} \right) = \frac{1}{n} \left(sL_2 \| \frac{1}{sC_2} + sL_{fl} \right) \quad (93)$$

By combining (90) and (93), the aggregated circuit model is shown in Figure 47.

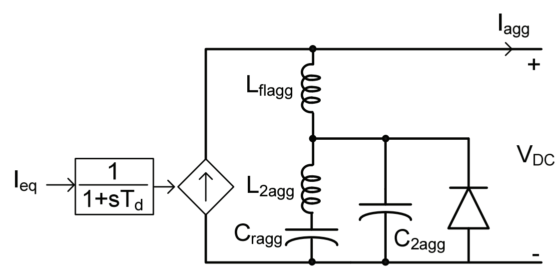

Figure 47: Aggregated wind turbine circuit model.

As can be seen from (91), the Norton equivalent is the sum of the individual wind turbines and high frequency changes will be filtered, however, oscillation could be induced at the resonant frequency of the filter components. A resistance in parallel with the inductor can be used to damp any resonant current oscillations.

5.2.2 AC Controller Design

The wind turbine control will have similar issues as with the DC grid design and will therefore be controlled using the controller in Figure 44. The LV VSC rectifier will be controlled to obtain unity power factor and to regulate the LV DC bus voltage. The converter will be controlled as a current source using a decoupled *pq* controller, shown in

Figure 48. This type of controller has high power quality and is able to maintain low fault current [76,77].

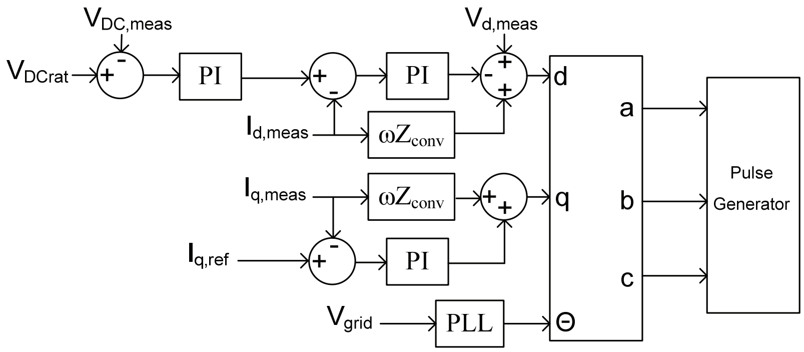

Figure 48: LV AC grid side converter controller.

The HV controller will be controlled to maintain the frequency of the wind farm grid and to support the voltage. This will require controlling the converter as a voltage source, directly controlling the magnitude and phase of the converter output depending on the magnitude of the AC voltage and the frequency of the grid [76]. The controller is shown in Figure 49.

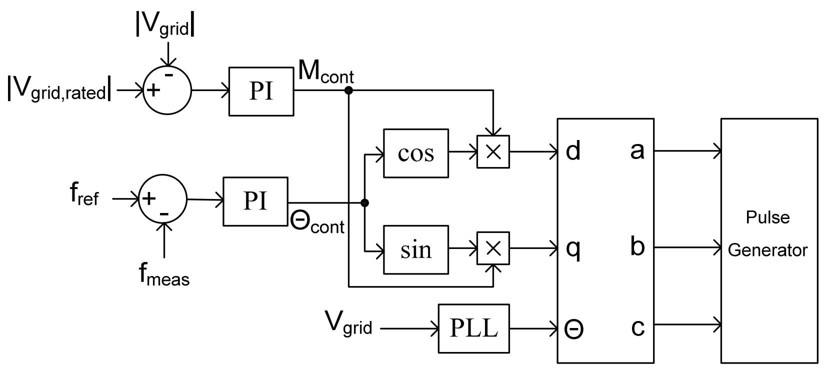

Figure 49: HV AC inverter controller.

The phase will determine the active power supplied to the grid and is controlled based on the magnitude of the DC voltage. The reactive power will be controlled by the magnitude of the grid voltage and will be used to support the MV grid. As shown in [78], this control can have a better response over decoupled *dq* axis control.

The controller for the AC grid aggregated wind farm converter uses the model derived in [73] and models the VSC converter using time delays. The aggregated wind farm controller is shown in Figure 50.

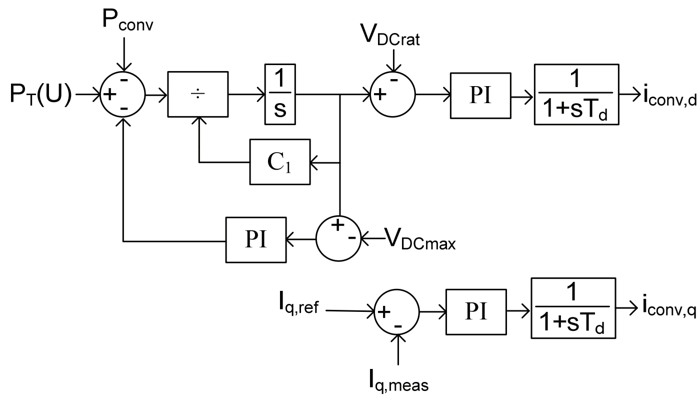

Figure 50: AC aggregated wind farm grid side converter model.

5.3 Integration Requirements

The effective operation of the systems will be evaluated based on the ability to deliver power from the wind farm during normal conditions, and to prevent fault propagation from a wind turbine to the wind farm, and from the wind farm to the HVDC line.

To test the operation during normal conditions, the MV systems (shown in Figure 40) will be tested by adjusting the power from the wind turbine with a ramp signal from zero to rated power and from rated power to zero. Effective operation will be determined by the ability of the system to maintain the DC and AC voltages within ±20% rated. Similar tests will be performed on the HVDC integration models (shown in Figure 41).

To test the operation during fault conditions, the following faults will be placed on the MV systems:

1. *LV DC bus fault*—a fault on the LV bus should not affect the voltage on the MV system and the converter currents and voltages should not exceed rated values.
2. *MV bus fault*—the fault should not cause current through the converter above the rated current and the wind turbine power should be ramped down to prevent an overvoltage on the LV DC bus. For the AC system, the fault will be tested on both the LV and MV sides of the transformer and both single phase and three phase faults will be tested.

To test the operation of the HVDC integration models during fault conditions, the models in Figure 41 will be subjected to the following tests:

1. *MV bus fault*—a fault on the MV bus should meet the same conditions as for the previous tests on the MV systems, and in addition should not propagate to the

HVDC line. For the AC system, the fault will be tested on both the MV and HV sides of the HV transformer and both single phase and three phase faults will be tested.

2. *HVDC line fault*—a fault on the HVDC line should not lead to overcurrent or overvoltage operation on the MV and LV buses.

5.4 Simulation Testing

PSCAD simulations were performed for the various tests describe in Section 5.3.

5.4.1 Operation for Normal Conditions

To test the operation of the MV DC-DC converter for normal operations, the wind power was varied from no-load to full load over 20 s. The input and output power of the converter is shown in Figure 51, where it can be seen that for a ramping signal from the start-up of the wind turbine to full power and from full power to no power, the converter is able to track the power and maintain the LV capacitor voltage within 20% of the rated voltage.

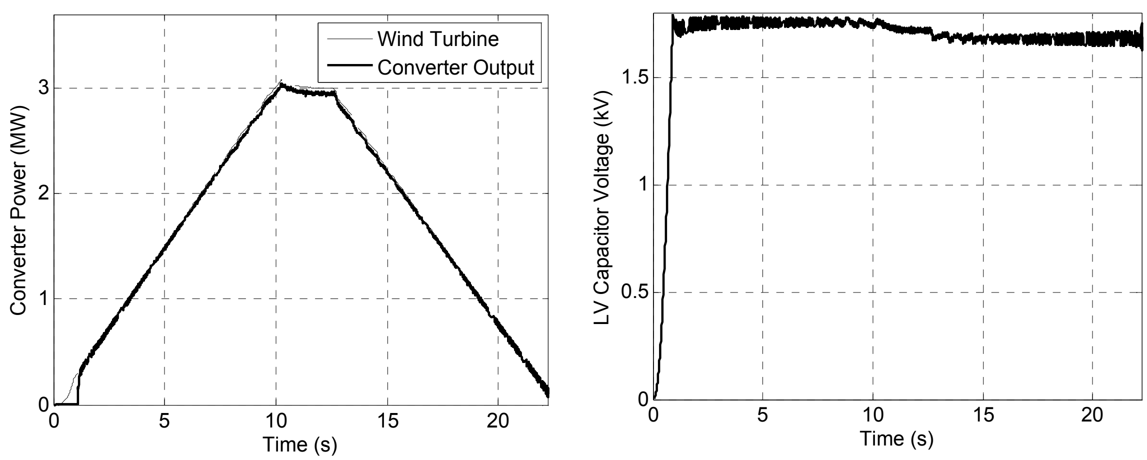

Figure 51: Converter power and LV capacitor voltage for ramping wind power input.

Figure 52 shows response of a DC grid based wind farm (shown in Figure 41) for increasing and decreasing wind power. The power into the grid is increased from 3% to full load and then decreased to 3%. The simulation was performed with the MV bus already energized, although the same converter control settings were used in energizing the bus. The MV bus voltage during the test is within 15% of the rated voltage. Converter losses were not considered in the model, but line losses used in the model were estimated at 1% for the simulation and can be seen when operating at full load.

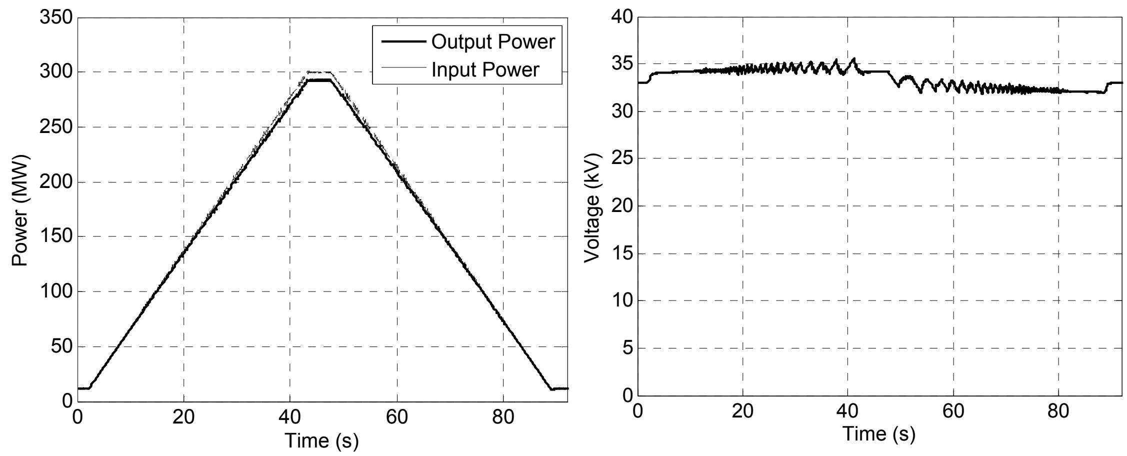

Figure 52: DC wind farm input/output power and MV bus voltage for ramping power input.

A similar ramp test was performed for the AC system in Figure 40 and the results are shown in Figure 53.

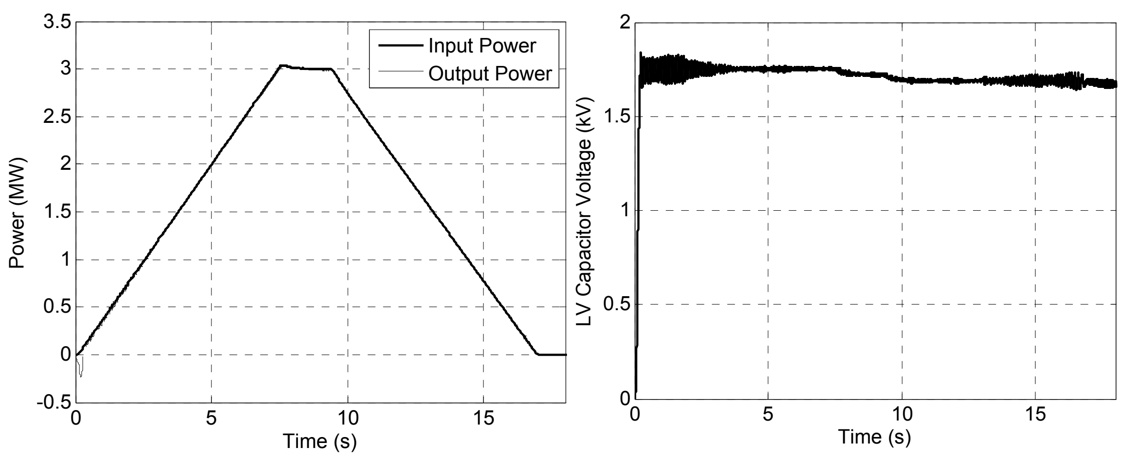

Figure 53: AC wind turbine converter input/output power and bus voltage for ramping power input.

A similar test was performed on the complete AC grid shown in Figure 41, using individual models for two turbines and an aggregated model for the others. The results show accurate power tracking by the HV converter over the whole operation.

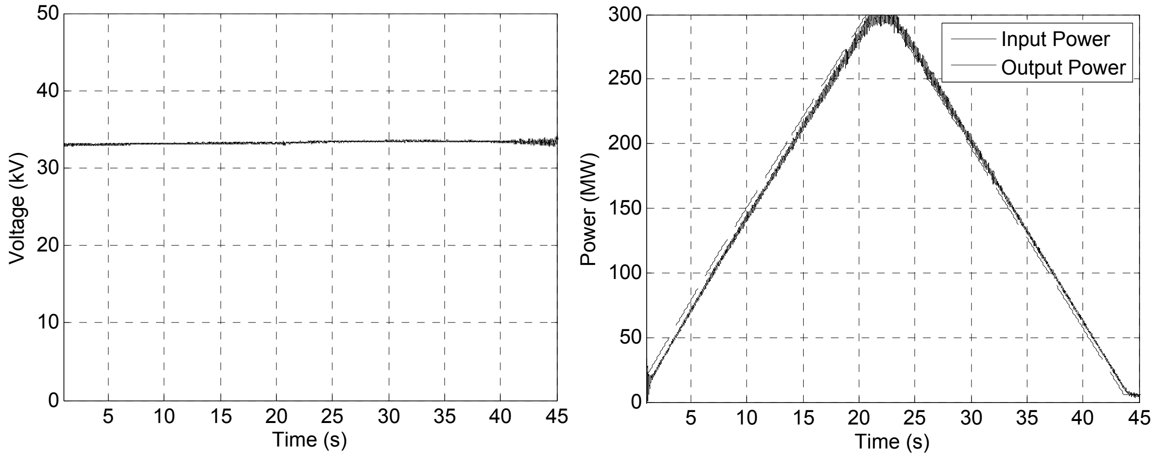

(a) MV bus rms voltage (b) AC grid input/output power

Figure 54: AC wind farm input/output power and MV bus voltage for ramping power input.

5.4.2 DC System Fault Analysis

The DC grid wind turbine converter model (shown in Figure 40) was tested for faults on the LV and MV terminals. Figure 55(a) shows the LV capacitor voltage for a MV fault and Figure 55(b) shows the MV capacitor voltage for a LV fault.

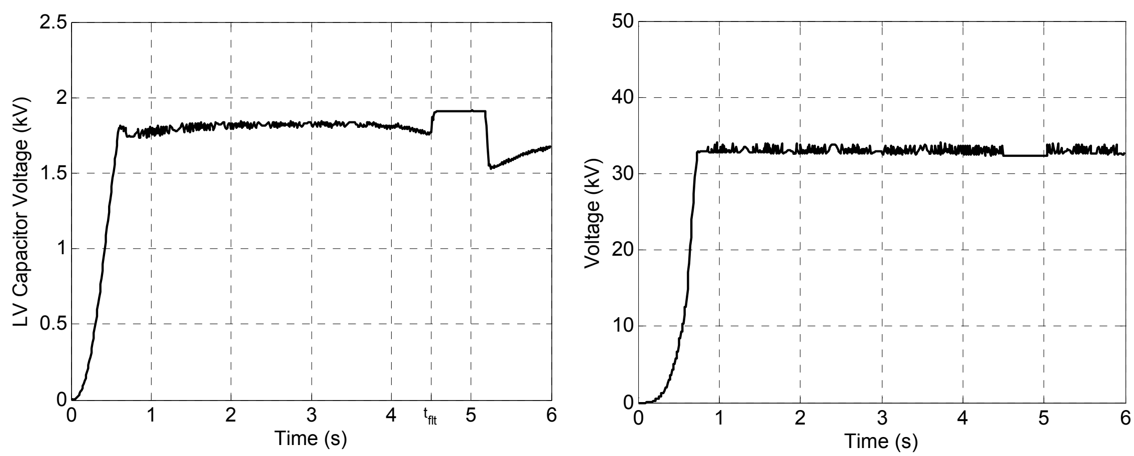

(a) MV fault (b) LV fault

Figure 55: DC wind turbine converter voltages during LV and MV DC bus faults.

As can be seen in Figure 55(a), after a fault is applied (at time t_{flt}), the converter stops switching, causing the voltage to increase. The operation of the breaking resistor keeps the voltage within limits until the fault is cleared. After the converter starts operating again, there is an initial drop in the voltage, but it is within limits and causes no oscillation in the LV capacitors or inductors. From Figure 55(b) it is clear that a fault on the LV side of the converter has very little impact on the voltage of the MV capacitor. It should be noted that a fault on the LV DC bus will cause the VSC converter to lose control, however, since the wind turbine operation is not studied in detail with this model then the impacts of this are not shown.

Results for testing the system for a fault applied to the HVDC line are shown in Figure 56.

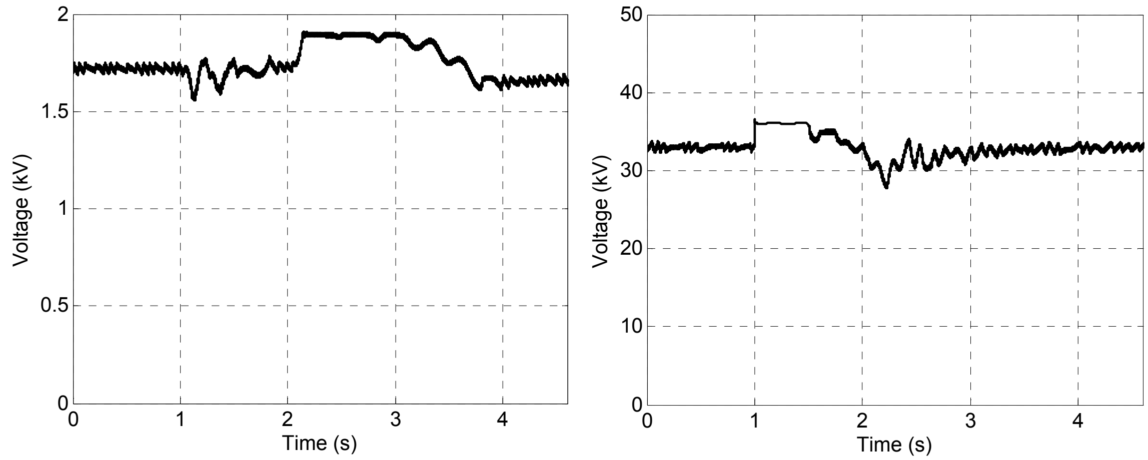

(a) LV bus voltage.   (b) MV bus voltage.

Figure 56: DC wind turbine LV and MV bus voltages during an HVDC line fault.

Starting from steady state operation at full load, a HV fault is applied at 1 s, after which it can be seen from Figure 56(b), the voltage of the MV bus increases rapidly when the converter operation is stopped until it is cut off by the operation of the breaking resistor. The fault is cleared after 500 ms, after which the converter starts operating again and the voltage decreases. The LV bus voltage shown in Figure 56(a) shows that the voltage increases after the fault is cleared and is cut off by the LV breaking resistor. This is due to the drop in MV bus voltage after the fault is cleared, requiring the converter to increase the frequency of operation to transfer the same amount of power.

5.4.3 AC System Fault Analysis

During AC faults, a VSC converter using decoupled *dq* current control can maintain control to minimize the fault current; however, a sudden decrease in grid voltage could result in overcurrent as the controller attempts to maintain the same level of power as before the fault [79]. IGBTs have smaller overcurrent ratings than thyristors (ABB IGBTs are generally rated for a peak transient current of 2x the DC current) and therefore this could cause problems during close-in faults. High current can also lead to saturation of the filter inductors, which can lead to current distortion and instability [2]. In addition, the lower power flow from the converter could also result in high voltages on the DC bus, possibly requiring a method of absorbing or decreasing the excess wind energy.

For the AC system showed in Figure 40, a 3-phase fault was applied on the MV side of the transformer and the resulting DC bus voltage and current is shown in Figure 57.

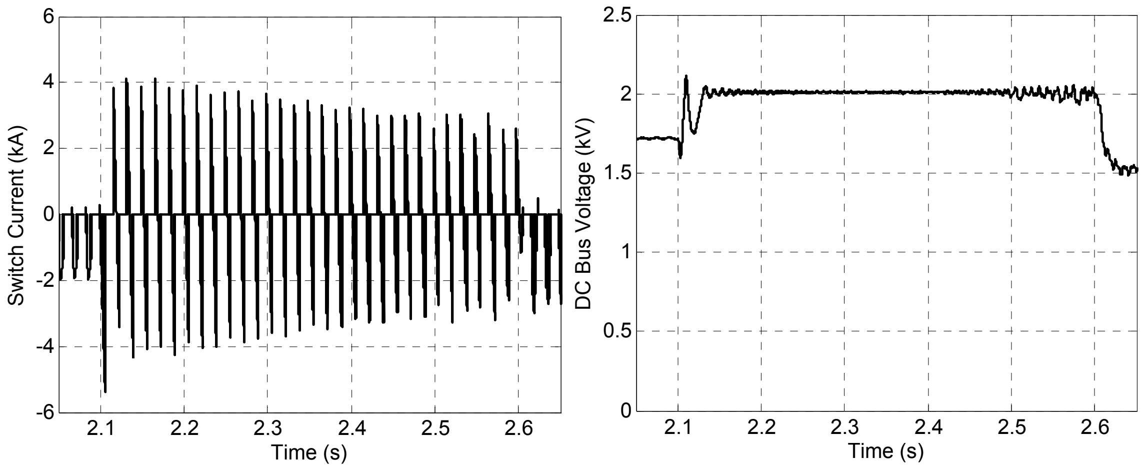

Figure 57: 3-Phase fault on the MV line during full power operation.

The fault occurs at t=2.1 and results in an increase in the DC bus voltage which activates the breaking resistor control to limit the overvoltage to less than 20%. The continued operation of the converter during the fault results in high current spikes. These high current peaks can be eliminated by detecting the fault and disabling converter operation and absorbing excess wind energy until the fault has been cleared and converter reconnected.

Faults on the DC bus of the VSC converter will forward bias the freewheeling diodes of the converter, causing it to lose control and resulting in a voltage dip on the AC side. This will require tripping the wind turbine, but the effect on the MV bus will be small due to impedance of the filter and transformer. The effect of a fault on the HVDC line will similarly forward bias the freewheeling diodes of the VSC HVDC converter, causing a major disturbance of the wind farm and at high powers could quickly lead to instability. The fault will need to be detected quickly and the converter operation disabled. Faults on the MV grid could affect the HVDC line and cause high currents in the VSC since it is operated as a voltage source. To prevent damage to the converter during MV grid faults will require quickly detecting the fault and stopping converter operation.

CHAPTER 6: DESIGN COMPARISON

This section summarizes the advantages and disadvantages of the AC and DC systems, based on the efficiency and component requirements (from Chapters 3 and 4) and the performance during normal conditions and grid faults (from Chapter 5).

6.1 Efficiency and Component Requirements

The advantages and disadvantages of the different technologies based on their efficiency and component requirements are listed in Table 19. The overall efficiency of the AC grid includes the VSC converters and the MV and HV transformers. The overall efficiency of the DC grid includes the MV and HV DC-DC converter and inductors.

Table 19: Comparison of design aspects of the AC and DC grid topologies.

	AC System		DC Systems	
	2-Level Converter based	3-Level NPC Converter based	Single Phase Resonant Converter	3-Phase Resonant Converter
Efficiency	▪ LV converter losses are 1.5% for the 1000 V_{AC} turbine and 5.5% for the 4000 V_{AC} turbine. ▪ HV converter losses are around 5%. ▪ Transformer efficiency is greater than 99%.	▪ LV converter losses are 1% for the 1000 V_{AC} turbine and 2% for the 4000 V_{AC} turbine. ▪ HV converter losses are around 1.5%. ▪ Transformer efficiency is greater than 99%.	▪ MV converter losses are around 4% for the 1000 V_{AC} turbine and 1.5% for the 4000 V_{AC} turbine. ▪ HV converter losses are around 2.5%. ▪ Inductor efficiency is around 97-99% for the 1000 V_{AC} turbine and 98-99% for the 4000 V_{AC} turbine.	▪ MV converter losses are around 5% for the 1000 V_{AC} turbine and 2-4% for the 4000 V_{AC} turbine. ▪ HV converter losses are less than 2%. ▪ Inductor efficiency is around 96% at full power. The efficiency of HV converter inductors is around 98%.
	▪ Grid efficiency: 92-93%	▪ Grid efficiency: 95-96.5%	▪ Grid efficiency: 91-95%	▪ Grid efficiency: 89-94%
Component Size/Weight	▪ The MV transformer mass is 4-5000 kg. ▪ The component sizes will be smaller than the DC converters since they are not rated for both high current and high voltage. ▪ Switch utilization is around 24%.	▪ Component sizes will be similar to the 2-level converter. ▪ Switch utilization is around 14%.	▪ The resonant inductor and capacitors will be large and built for high power and high voltage. ▪ The weight of the MV inductors varies from 400-2000 kg depending on the turbine and losses. ▪ Switch utilization is around 0.1-0.4%.	▪ Similar to the single phase design, the resonant inductors and capacitors are large. Disadvantages are that there are 3 resonant capacitors and 6 LV inductors. ▪ There are 1.5x the number of switches compared to the single phase design; switch utilization is around 0.15-0.68%.
Cable Design	▪ Losses are ~0.2% for a 70 mm^2 3-cond. copper cable or 120 mm^2 aluminum cable (avg. cable length of 3 km).		▪ Losses are ~0.2% for a 150 mm^2 copper cable or 240 mm^2 aluminum cable (avg. cable length of 3 km)	

Overall, the most efficient method analyzed is to connect the wind farm using 3-level NPC VSC converters and to transform the voltage using 60 Hz AC transformers. The DC grid topology has very high losses when considered for a design using wind turbines with a 1000 V_{AC} output voltage. There is more potential though when wind turbines with 4000 V_{AC} output voltages are considered. The 3-phase resonant converter design offers lower switching losses, but the additional components and thyristor losses reduce the benefits of this topology.

6.2 Performance Analysis

The performance of both the AC and DC systems for tracking changing wind power was similar. Both the individual wind turbine converters, and the HV converters, showed the ability to maintain stability during fast changing wind power.

The results of the simulation tests for the AC and DC systems, developed in Sections 5.4.2 and 5.4.3, are summarized in Table 20.

Table 20: Fault responses of the AC and DC systems.

	AC System	DC System
LV DC Bus Fault	▪ A fault on the LV DC bus had a minimal effect on the MV bus due to the impedance of the filter and transformer.	▪ A fault on the LV DC had no effect on the MV bus
MV Bus Fault	▪ A close-in fault on the MV AC bus could result in high current peaks that could damage the IGBT switches and may require stopping converter operation. ▪ The operation of the HV converter is as a voltage source and a fault on the MV AC bus could lead to high currents in the VSC, which may need to be tripped.	▪ A fault on the MV DC bus required temporarily stopping operation the MV DC-DC converter and absorbing the power from the wind turbine. ▪ There was no effect on the HVDC bus.
HVDC Bus Fault	▪ This will forward bias the converter diodes, causing the converter to lose control. The low voltage on the DC side could result in high current and instability of the wind farm grid due to loss of control.	▪ This will require the HV DC-DC converter to temporarily stop operation and the excess power must be absorbed.

It should be noted that the control of both systems was done by PI controllers that needed to be fine tuned to have good performance and maintain stability. In addition, the AC system required the wind turbines to also produce reactive power to help maintain the wind farm grid voltage when the wind farm is operating close to full power.

Overall, the system responses during faults varied between the AC and DC systems, with both systems having different issues. Solutions were developed in Chapter 5 in order to minimize the disturbance during a fault and to allow fast reconnection after faults, but this is an area requiring further study.

6.3 Result Validation

Models of the single and 3-phase DC-DC converters were built in both Matlab Simulink and PSCAD to verify the overall operation of each type of converter. The detailed derivations of both the single phase and 3-phase DC-DC converters in Appendices C and D accurately correspond to the simulation results. Figure 58 shows the PSCAD simulation results and the converter power at various frequencies predicted by the derived models.

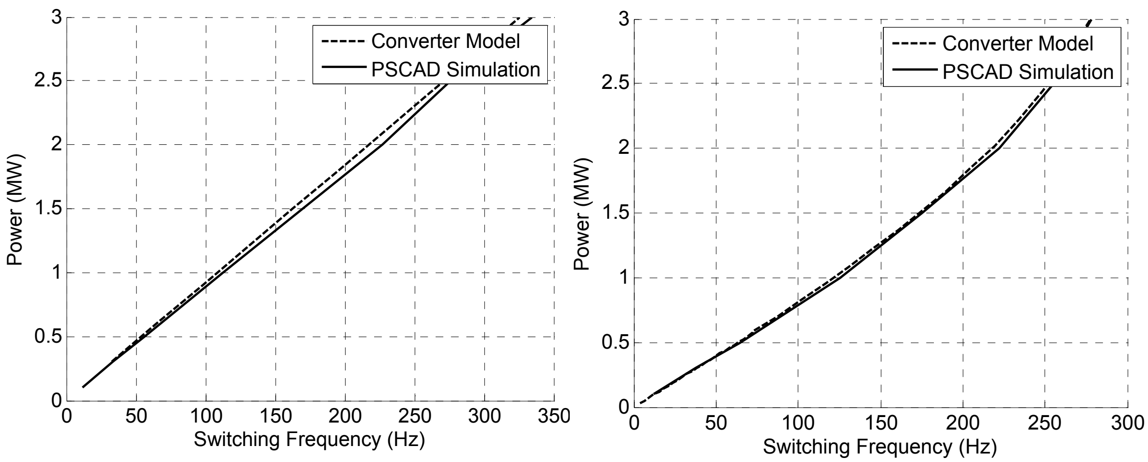

(a) Single phase resonant converter

(b) 3-phase resonant converter

Figure 58: 3-Phase fault on the MV line during full power operation.

Simulink and PSCAD models were also built for both the 2-level and 3-level converters.

Although the use of different simulation programs allows some verification of the predicted results, more detailed testing will require construction of a prototype converter. This will allow more accurate analysis of the component losses and the performance during faults.

CHAPTER 7: CONCLUSION

7.1 Summary

This thesis outlined designs for AC and DC grid based wind farms connected to an HVDC line. AC grids using 2 and 3-level voltage source converters were compared with DC grids using single phase and 3-phase DC-DC resonant converters based on:

- *Efficiency and Component Requirements*—the efficiency and losses for the various designs were estimated using detailed calculations based on switch datasheets and models of the transformers and inductors. Different types of switches were used to compare the effects on the overall efficiency and component requirements. The benefits for different grid voltages were also compared.
- *Performance*—the performance of the AC and DC grids were compared during normal operation and during faults. Wind farm models using the 3-level NPC converters and single phase DC-DC resonant converters were built using PSCAD. The grid models were tested to determine the performance for a ramping input from no-load to rated power, and for faults on the LV DC bus, the MV bus, and the HVDC line. Controller designs were developed for the different converters to minimize the effect of faults and enable fast reconnection after transient faults.

7.2 Conclusions

The main conclusions related to the efficiency of the AC and DC grid based wind farms are:

1. The most efficient method studied for connecting the wind farm is using 3-level NPC VSC converters. The converter losses are around 1-1.5% and the transformer losses are less than 1%.
2. The most efficient DC grid based method studied for connecting a wind farm uses a single phase resonant converter and has converter losses of 1.5-4% and inductor losses of 1-3%.
3. Amorphous core technology could offer lower losses and lower costs than silicon steel cores; however, the weight will be increased, which could affect their use in offshore applications. More study is required to analyse structural, mechanical, and insulation issues.

4. The DC-DC resonant converters have lower efficiencies when transforming high power with a high voltage gain. Therefore the losses were much lower when they were calculated for wind turbines operating at 4000 V, where the gain would be less than ten.

5. The 3-phase resonant converter can achieve lower switching losses than the single phase resonant converter, since it has reduced thyristor reverse recovery losses. The advantages gained by this design are reduced due to the higher component requirements and higher inductor losses.

The main conclusions related to the performance of the AC and DC grid based wind farms are:

1. Simulations of the NPC VSC HVDC and single phase resonant converter systems showed close power tracking during normal operation of the wind farm.

2. The HV side of a single phase resonant converter is not affected by faults on the LV side. This is an important advantage when connecting to a HVDC line.

3. Faults on the HVDC line will require stopping operation of the connecting single phase resonant converter. The energy from the wind farm will then have to be absorbed or decreased.

4. To allow fault ride through in the DC grid, breaking resistors, or a suitable method of absorbing excess wind energy during a fault, are required for both the wind turbine converters and the HV DC-DC converter. The sizing of these resistors could be an issue.

5. The VSC converters have poor isolation for faults on the HVDC line, which could lead to instability on the wind farm grid.

6. Faults on the MV bus of the AC grid could cause high currents through the HV VSC and affect the HVDC line, since it is operated as a voltage source and is not controlling the current directly.

7. Close in faults on the MV bus could cause high current in the LV converters. Even though the current is directly controlled, the low voltage and small impedance on the AC side will lead to high peak current during switching.

7.3 Future Research

Possible areas of future research include:

1. Further studies of other types of DC-DC converters should be performed using the same application of connecting a wind farm to an HVDC line. Although other DC-DC converter studies have been conducted, they are not directly comparable with the results in this work since the application was different.

2. At this point, only simulation testing has been performed with the single-phase and 3-phase resonant converters. Although this thesis has analyzed the switching losses in detail, a better approximation would be obtained using a hardware model.

3. A newer VSC technology that is promising is the multi-module based converter (reviewed in Section 1.2). This type of converter may be better suited for this application.

4. More research is required for both the AC and DC grids on improving the protection. The analysis in Chapter 4 has only demonstrated some of the control and protection issues. A detailed model of the PMSG of the wind turbine should be used.

5. Integration analysis is required using a more detailed HVDC model, such as the CIGRE benchmark. This will allow more detailed design of fault ride through capability for faults on the HVDC line.

REFERENCES

[1] E. Hau, *Wind turbines : fundamentals, technologies, application, economics*, Berlin, Germany: Springer, 2006.

[2] E. Bueno, S. Cobreces, F. Rodriguez, A. Hernandez, and F. Espinosa, "Design of a Back-to-Back NPC Converter Interface for Wind Turbines With Squirrel-Cage Induction Generator," *IEEE Trans. Energy Convers.*, vol. 23, Sep. 2008, pp. 932-945.

[3] B. Andresen and J. Birk, "A high power density converter system for the Gamesa G10x 4,5 MW wind turbine," *2007 European Conference on Power Electronics and Applications*, 2007, pp. 1-8.

[4] P. Bresesti, W. Kling, R. Hendriks, and R. Vailati, "HVDC Connection of Offshore Wind Farms to the Transmission System," *IEEE Trans. Energy Convers.*, vol. 22, Mar. 2007, pp. 37-43.

[5] D. Jovcic, "Interconnecting offshore wind farms using multiterminal VSC-based HVDC," *Power Engineering Society General Meeting, 2006. IEEE*, 2006, p. 7.

[6] C. Anderson and J. Cardell, "Reducing the Variability of Wind Power Generation for Participation in Day Ahead Electricity Markets," *Hawaii International Conference on System Sciences, Proceedings of the 41st Annual*, 2008, p. 178.

[7] W. Xu, K. Mauch, and S. Martel, *An Assessment of Distributed Generation Islanding Detection Methods and Issues for Canada*, CANMET Energy Technology Centre - Varennes: Natural Resources Canada, 2004.

[8] J. Morneau, C. Abbey, and G. Joos, "Effect of Low Voltage Ride Through Technologies on Wind Farm," *Electrical Power Conference, 2007. EPC 2007. IEEE Canada*, 2007, pp. 56-61.

[9] J. Arrillaga, Y.H. Liu, and N. Watson, *Flexible Power Transmission: The HVDC Options*, West Sussex, England: John Wiley and Sons, 2007.

[10] M. Bahrman and B. Johnson, "The ABCs of HVDC transmission technologies," *Power and Energy Magazine, IEEE*, vol. 5, Apr. 2007, pp. 32-44.

[11] S. Bozhko, G. Asher, Risheng Li, J. Clare, and Liangzhong Yao, "Large Offshore DFIG-Based Wind Farm With Line-Commutated HVDC Connection to the Main Grid: Engineering Studies," *IEEE Trans. Energy Convers.*, Mar. 2008, pp. 119-127.

[12] B. Andersen and Lie Xu, "Hybrid HVDC system for power transmission to island networks," *Transmission and Distribution Conference and Exposition, 2003 IEEE PES*, 2003, pp. 55-60 Vol.1.

[13] Lie Xu, Liangzhong Yao, and C. Sasse, "Grid Integration of Large DFIG-Based Wind Farms Using VSC Transmission," *IEEE Trans. Power Syst.*, Aug. 2007, pp. 976-984.

[14] B.R.A. Lie Xu, "Grid connection of large offshore wind farms using HVDC," *Wind Energy*, vol. 9, Dec. 2006, pp. 371-382.

[15] R. Bartnikas and K. Srivastava, *Power and Communication Cables: Theory and Applications*, IEEE Press, 2000.

[16] A. Carlson, *Specific requirements on HVDC converter transformers*, ABB, 1996.

[17] B. Bisewski and R. Atmuri, "Considerations for the Application of 800 kV HVDC Transmission from a System Perspective," *International Workshop for 800 kV HVDC Systems*, 2005.

[18] T. Yamanaka, S. Maruyama, and T. Tanaka, "The development of DC+/-500 kV XLPE cable in consideration of the space charge accumulation," *Proceedings of the 7th International Conference on Properties and Applications of Dielectric Materials.*, 2003, pp. 689-694

[19] ABB, "Grid Connection of Offshore Wind Farms - NORD E.ON 1," 2008.

[20] B. Gemmell, J. Dorn, D. Retzmann, and D. Soerangr, "Prospects of multilevel VSC technologies for power transmission," *Transmission and Distribution Conference and Exposition, 2008. T&D. IEEE/PES*, 2008, pp. 1-16.

[21] Guanjun Ding, Guangfu Tang, Zhiyuan He, and Ming Ding, "New technologies of voltage source converter (VSC) for HVDC transmission system based on VSC," *Power and Energy Society General Meeting - Conversion and Delivery of Electrical Energy in the 21st Century, 2008 IEEE*, 2008, pp. 1-8.

[22] S. Allebrod, R. Hamerski, and R. Marquardt, "New transformerless, scalable Modular Multilevel Converters for HVDC-transmission," *Power Electronics Specialists Conference, 2008. PESC 2008. IEEE*, 2008, pp. 174-179.

[23] R. Marquardt and A. Lesnicar, "New Concept for High Voltage - Modular Multilevel Converter," *Power Electronics Specialists Conference*, 2004.

[24] A. Hammad, "Stability and control of HVDC and AC transmissions in parallel," *IEEE Trans. Power Del.*, vol. 14, Oct. 1999, pp. 1545-1554.

[25] L. Pilotto, M. Szechtman, A. Wey, W. Long, and S. Nilsson, "Synchronizing and damping torque modulation controllers for multi-infeed HVDC systems," *IEEE Trans. Power Del.*, vol. 10, Jul. 1995, pp. 1505-1513.

[26] H. Clark, A. Edris, M. El-Gasseir, K. Epp, A. Isaacs, and D. Woodford, "Softening the Blow of Disturbances," *Power and Energy Magazine, IEEE*, vol. 6, Feb. 2008, pp. 30-41.

[27] B. Qahraman, A. Gole, and I. Fernando, "Hybrid HVDC converters and their impact on power system dynamic performance," *Power Engineering Society General Meeting, 2006. IEEE*, 2006, p. 6 pp.

[28] Wulue Pan, Yong Chang, and Hairong Chen, "Hybrid Multi-terminal HVDC System for Large Scale Wind Power," *Power Systems Conference and Exposition, 2006. PSCE '06. 2006 IEEE PES*, 2006, pp. 755-759.

[29] Hongbo Jiang and A. Ekstrom, "Multiterminal HVDC systems in urban areas of large cities," *IEEE Trans. Power Del.*, vol. 13, Oct. 1998, pp. 1278-1284.

[30] N. Nosaka, Y. Tsubota, K. Matsukawa, K. Sakamoto, H. Nakamura, M. Takasaki, and H. Kawazoe, "Simulation studies on a control and protection scheme for hybrid multi-terminal HVDC systems," *Power Engineering Society Winter Meeting,* 1999, pp. 1079-1084

[31] Weixing Lu and Boon-Teck Ooi, "Premium quality power park based on multi-terminal HVDC," *IEEE Trans. Power Del.*, vol. 20, Apr. 2005, pp. 978-983.

[32] G. Asplund, "Electric Transmission System in Change," Rhodes, Greece: 2008.

[33] Lianxiang Tang and Boon-Teck Ooi, "Locating and Isolating DC Faults in Multi-Terminal DC Systems," *IEEE Trans. Power Del.*, vol. 22, 2007, pp. 1877-1884.

[34] Weixing Lu and Boon-Teck Ooi, "DC overvoltage control during loss of converter in multiterminal voltage-source converter-based HVDC (M-VSC-HVDC)," *IEEE Trans. Power Del.*, vol. 18, 2003, pp. 915-920.

[35] Xiao-Ping Zhang, "Multiterminal voltage-sourced converter-based HVDC models for power flow analysis," *IEEE Trans. Power Syst.*, vol. 19, Nov. 2004, pp. 1877-1884.

[36] R. Gules, J. De Pellegrin Pacheco, H. Hey, and J. Imhoff, "A Maximum Power Point Tracking System With Parallel Connection for PV Stand-Alone Applications," *IEEE Trans. Ind. Electron.*, vol. 55, Jul. 2008, pp. 2674-2683.

[37] Seung-Ho Song, Shin-il Kang, and Nyeon-kun Hahm, "Implementation and control of grid connected AC-DC-AC power converter for variable speed wind energy conversion system," *Applied Power Electronics Conference and Exposition, 2003*. pp. 154-158 vol.1.

[38] S. Lundberg, "Configuration Study of Large Wind Parks," Licentiate thesis, Chalmers University of Technology, 2003.

[39] Xiong Xin and Liang Hui, "Research on multiple boost converter based on MW-level wind energy conversion system," *Electrical Machines and Systems, 2005. ICEMS 2005. Proceedings of the Eighth International Conference on*, 2005, pp. 1046-1049 Vol. 2.

[40] L. Max and S. Lundberg, "System efficiency of a DC/DC converter-based wind farm," *Wind Energy*, vol. 11, Oct. 2008, pp. 109-120.

[41] C. Meyer, M. Hoing, A. Peterson, and R. De Doncker, "Control and Design of DC-Grids for Offshore Wind Farms," *Industry Applications Conference, 2006. 41st IAS Annual Meeting. Conference Record of the 2006 IEEE*, 2006, pp. 1148-1154.

[42] O. Martander, "DC Grids for Wind Farms," Licentiate thesis, Chalmers University of Technology, 2002.

[43] D. Jovcic, "Step-up DC-DC converter for megawatt size applications," *IET Power Electronics*, vol. 2, Nov. 2009, pp. 675-685.

[44] D. Jovcic, "Bidirectional, High-Power DC Transformer," *IEEE Trans. Power Del.*, vol. 24, Oct. 2009, pp. 2276-2283.

[45] H. Polinder, F. van der Pijl, G. de Vilder, and P. Tavner, "Comparison of direct-drive and geared generator concepts for wind turbines," *Electric Machines and Drives, 2005 IEEE International Conference on*, 2005, pp. 543-550.

[46] K. Larsen, "Making wind more efficient?," *Renewable Energy Focus*, vol. 9, Dec. 2008, pp. 40-42.

[47] Hui Li, Zhe Chen, and H. Polinder, "Optimization of Multibrid Permanent-Magnet Wind Generator Systems," *IEEE Trans. Energy Convers.*, vol. 24, Mar. 2009, pp. 82-92.

[48] J. Manwell, J. McGowan, and A. Rogers, *Wind Energy Explained - Theory, Design and Application.*, John Wiley & Sons Ltd., 2002.

[49] Wei Li, C. Abbey, and G. Joos, "Control and Performance of Wind Turbine Generators based on Permanent Magnet Synchronous Machines Feeding a Diode Rectifier," *Power Electronics Specialists Conference, 2006. PESC '06. 37th IEEE*, 2006, pp. 1-6.

[50] M. Chinchilla, S. Arnaltes, and J. Burgos, "Control of permanent-magnet generators applied to variable-speed wind-energy systems connected to the grid," *IEEE Trans. Energy Convers.*, vol. 21, Mar. 2006, pp. 130-135.

[51] I. Schiemenz and M. Stiebler, "Control of a permanent magnet synchronous generator used in a variable speed wind energy system," *Electric Machines and Drives Conference, 2001. IEMDC 2001. IEEE International*, 2001, pp. 872-877.

[52] Xiangjun Zeng, Zhe Chen, and F. Blaabjerg, "Design and comparison of full-size converters for large variable-speed wind turbines," *European Conference on Power Electronics and Applications.*, 2007, pp. 1-10.

[53] L. Helle and S. Munk-Nielsen, "Comparison of converter efficiency in large variable speed wind turbines," *Applied Power Electronics Conference and Exposition, 2001. APEC 2001. Sixteenth Annual IEEE*, 2001, pp. 628-634 vol.1.

[54] E. Carroll, S. Linder, I. Blidberg, and A. Chekmarev, "High power semiconductors in the world of energy management," *Russian Electrical Engineering*, vol. 78, Oct. 2007, pp. 11-15.

[55] Dynex Semiconductor, "Parallel Operation of Dynex IGBT Modules - Application Note," Jul. 2002.

[56] F. Casanellas, "Losses in PWM inverters using IGBTs," *Electric Power Applications, IEE Proceedings*, vol. 141, 1994, pp. 235-239.

[57] N. Mohan, T. Undeland, and W. Robbins, *Power Electronics - Converters, Applications, and Design*, John Wiley and Sons, Inc., 2003.

[58] R. Erickson, *Fundamentals of Power Electronics*, Chapman & Hall, 1997.

[59] J. Rodriguez, S. Bernet, Bin Wu, J. Pontt, and S. Kouro, "Multilevel Voltage-Source-Converter Topologies for Industrial Medium-Voltage Drives," *IEEE Trans. Ind. Electron.*, vol. 54, Dec. 2007, pp. 2930-2945.

[60] T. Bruckner, S. Bernet, and P. Steimer, "Feedforward Loss Control of Three-Level Active NPC Converters," *IEEE Trans. Ind. Appl.*, vol. 43, Dec. 2007, pp. 1588-1596.

[61] J. Sayago, S. Bernet, and T. Bruckner, "Comparison of Medium Voltage IGBT-based 3L-ANPC-VSCs," *Power Electronics Specialists Conference, 2008. PESC 2008. IEEE*, 2008, pp. 851-858.

[62] A. Leedy and R. Nelms, "Harmonic Analysis of a Three-Level Sinusoidal PWM Inverter Using the Method of Pulse Pairs," *Industrial Electronics, 2006 IEEE International Symposium on*, 2006, pp. 1188-1193.

[63] A. Leedy, W. Dillard, and R. Nelms, "Harmonic analysis of a two-level sinusoidal PWM inverter using the method of pulse pairs," *Industrial Electronics Society, 2005. IECON 2005. 31st Annual Conference of IEEE*, 2005, p. 6 pp.

[64] M. Liserre, F. Blaabjerg, and S. Hansen, "Design and control of an LCL-filter based three-phase active rectifier," *Industry Applications Conference, 2001. Thirty-Sixth IAS Annual Meeting. Conference Record of the 2001 IEEE*, 2001, pp. 299-307 vol.1.

[65] S. Araujo, A. Engler, B. Sahan, and F. Antunes, "LCL filter design for grid-connected NPC inverters in offshore wind turbines," *7th Internatonal Conference on Power Electronics, 2007. ICPE '07.*, 2007, pp. 1133-1138.

[66] Bharat Heavy Electricals Limited, *Transformers*, McGraw-Hill, 2005.

[67] J. Fothergill, P. Devine, and P. Lefley, "A novel prototype design for a transformer for high voltage, high frequency, high power use," *IEEE Trans. Power Del.*, vol. 16, Jan. 2001, pp. 89-98.

[68] R. Del Vecchio, B. Poulin, P. Feghali, D.M. Shah, and R. Ahuja, *Transformer Design Principles: with applications to core-form power transformers*, Gordon and Breach Science Publishers, 2001.

[69] D. Jovcic, "Step up DC-DC converter for MW-size applications," *in print, IET Power Electronics, PEL-2008-0101*, pp. April, 2008.

[70] D. Jovcic, "Bidirectional high power DC transformer," *IEEE Trans. Power Del., TPWRD-00689-2008, in print September 2008*.

[71] General Cable, "19/33 kV Aluminium XLPE 1C Heavy Duty Cable Brochure," 2002.

[72] General Cable, "19/33 kV Copper XLPE 1C Heavy Duty Cable Brochure," 2002.

[73] A. Perdana, "Dynamic Models of Wind Turbines," Ph.D. diss., Chalmers University of Technology, 2008.

[74] N. Kimura, T. Funaki, and K. Matsu-ura, "Damping of current oscillation in superconductive line applied for high voltage direct current transmission system," *IEEE Trans. App. Supercond.*, vol. 3, Mar. 1993, pp. 223-225.

[75] HVR Advanced Power Component, "Custom Resistor Assemblies Brochure," May. 2008.

[76] T. Ishikawa, *Grid-connected photovoltaic power systems: Survey of inverter and related protection equipments*, IEA-PVPS, 2002.

[77] M. Prodanovic and T. Green, "Control and filter design of three-phase inverters for high power quality grid connection," *IEEE Trans. Power Electron.*, vol. 18, Jan. 2003, pp. 373-380.

[78] D. Jovcic, L. Lamont, and K. Abbott, "Control system design for VSC transmission," *Electric Power Systems Research*, vol. 77, May. 2007, pp. 721-729.

[79] F.A. Magueed, A. Sannino, and J. Svensson, "Design of robust converter interface for wind power applications," *Wind Energy*, vol. 8, 2005, pp. 319-332.

[80] *Calculation of Major IGBT Operating Parameters*, Infineon Technologies, 1999.

[81] T. Eichhorn, "Estimate Inductor Losses Easily in Power Supply Designs," *Power Electronics Technology*, Apr. 2005.

[82] Pavlos S. Georgilakis and Eleftherios I. Amoiralis, "Spotlight on transformer design," *Power and Energy Magazine, IEEE*, vol. 5, Feb. 2007, pp. 40-50.

[83] AK Steel, "Oriented & TRAN-COR H Electrical Steels - Brochure," Jul. 2007.

[84] K. Iwayama, K. Ueno, Y. Yoshitomi, H. Nakayama, and T. Kumano, "7-mil-thick high-permeability grain-oriented silicon steel sheet," *Journal of Applied Physics*, vol. 63, 1988, pp. 2971-2973.

[85] Nippon Steel, "Electrical Steel Sheets - Brochure," Mar. 2007.

[86] M. Heathcote, *J & P Transformer Book: a practical technology of the power transformer*, Elsevier/Newnes, 2007.

[87] R. Hasegawa and D. Azuma, "Impacts of amorphous metal-based transformers on energy efficiency and environment," *Journal of Magnetism and Magnetic Materials*, vol. 320, Oct. 2008, pp. 2451-2456.

[88] Hitachi, "Hitachi Amorphous Transformers Brochure," Mar. 2009.

APPENDIX A. EFFICIENCY CALCULATIONS

The efficiency for different wind farm connection topologies will be compared by calculating the losses of the various components. Since the AC and DC grids are both analyzed using PMSG wind turbines, therefore generator losses will not be compared. Both passive and active components are examined.

Switch losses will vary depending on the type of switch and will include both switching and conduction losses. To precisely determine the switching losses will require building a prototype or using a detailed simulation program. However, an estimate may be obtained by using the current and voltage waveforms of ideal switches and loss information obtained from the datasheet. The switches that are considered are thyristors, IGBTs, and diodes.

A.1 Thyristor Losses

An estimate of thyristor losses can be obtained by using datasheet information to calculate the turn-on losses, reverse recovery losses during turn-off, and conduction losses.

A.1.1 Thyristor Conduction Losses

The steady state losses during the on-state will depend on the voltage drop across the thyristor when on (V_T) and the current through the diode. The voltage drop across the thyristor is a function of the thyristor current. A graph showing the voltage and current during conduction from the ABB 5STP 38Q4200 datasheet is shown in Figure A-1.

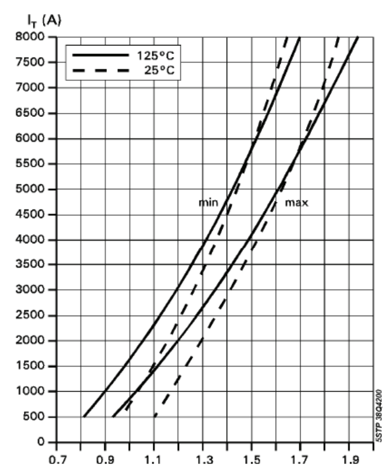

Figure A-1: ABB 5STP 38Q4200 thyristor conduction characteristics.

This can be estimated as a linear function:

$$I_T = V_{T0} + r_T V_T \tag{A1}$$

where V_{T0} and r_T are constants obtained from the datasheet. A more precise value may be given by the manufacturer. The datasheet for the ABB 5STP 38Q4200 thyristor specifies that the voltage drop across the thyristor when on is:

$$V_T = A + BI_T + C\ln(I_T + 1) + D\sqrt{I_T} \tag{A2}$$

where A=341.7x10^{-3}, B=90.0 x10^{-6}, C=76.26x10^{-3}, D=2.31 x10^{-3}. The steady state losses during the off-state will depend on the leakage current and the voltage across it. From the datasheet for ABB 5STP 38NQ4200 thyristors, the peak leakage current during both forward and reverse blocking is 400 mA. These losses will be estimated by considering the leakage current to be linearly related to the off-state voltage across the thyristor.

The total thyristor conduction losses over one switching cycle are given by:

$$W_{cond} = \int_0^{t_{ON}} I_{ON} V_T \, dt + \int_0^{t_{OFF}} I_{leak} \frac{V_{OFF}^2}{V_{rated}} dt \tag{A3}$$

A.1.2 Thyristor Turn-on Losses

Turn-on losses are caused by higher resistance across the switch after turning on. These losses can be estimated using the current rise-time, the voltage fall-time, and the initial voltage across the thyristor. The current rise-time will depend on the external circuit; however, the voltage fall-time must be estimated from datasheet information. A typical turn-on waveform (from the Polovidiče TR 918F-1790-12 datasheet) and a simplified waveform that will be used for estimating turn-on losses are in Figure A-2.

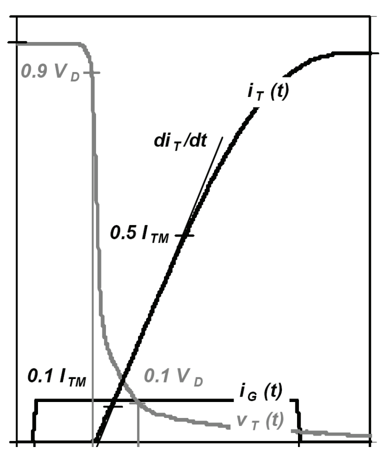

(a) Polovidiče TR 918F-1790-12 turn-on waveform.

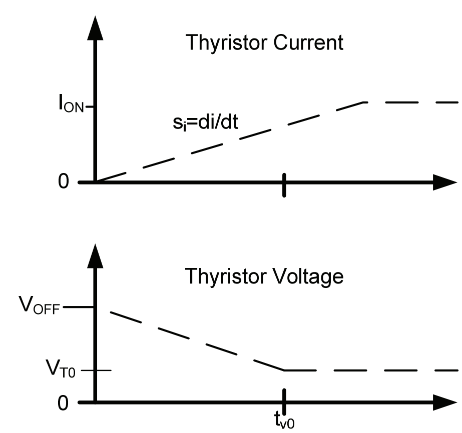

(b) Waveform for turn-on loss estimation

Figure A-2: Turn-on voltage and current waveforms.

The time t_{v0} in Figure A-2(b) represents the time for the voltage to drop to the on-state voltage drop. This time will vary depending on the gate current and rate of change of current at turn-on. An example graph showing the turn-on-time of a Mitsubishi thyristor (taken from the FT1500AU-240 datasheet) is shown in Figure A-3.

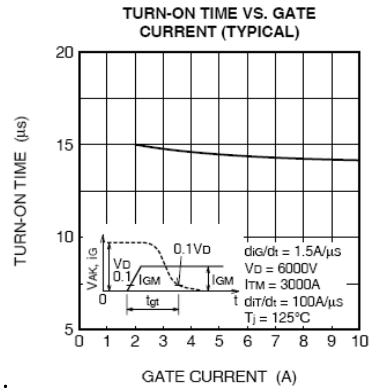

Figure A-3: Mitsubishi Electric FT1500AU-240 turn-on time.

The turn-on losses may also be given as a function of the rate-of-change of current (such as the Polovidiče TR 918F-1790-12) or a function of the on-state current and rate-of change of current (such as for ABB thyristors). ABB calculates these losses using the following formula (from ABB's Data Sheet User's Guide, section 3):

$$W_{turn-on} = \int_0^{t_{spread}} \left(V(t) - V_{T0}\right) I(t) dt \tag{A4}$$

where t_{spread} is the plasma spreading time and V_{T0} is on the on-state voltage drop. The actual voltage and current characteristic at turn on is difficult to estimate and therefore the estimated waveform in Figure A-2(b) will be used. Using Figure A-2(b) and ignoring losses due to the on-state voltage drop, as in (A4), the energy loss at turn-on will therefore be:

$$W_{turn-on} = \int_0^{t_{v0}} V(t) I(t) dt = \int_0^{t_{v0}} \left(V_{OFF} - \frac{V_{OFF}}{t_{v0}} t \right) (s_i t) dt = \frac{V_{OFF}}{6} s_i t_{v0}^2 \tag{A5}$$

The time for the voltage to drop to 10% of its original value may be specified in the datasheet based on the initial voltage, final voltage and current, and the gate current. Also, the gate current pulse may be optimized to reduce losses by using a higher initial amplitude.

If the turn-on losses are given for varying di/dt (as in Polovidiče datasheets), the value of t_{v0} (the time for the voltage to decrease to the on-state voltage drop) can be estimated using

(A5) and the off-state voltage (V_{OFF}). With ABB 5STP 38Q4200 datasheets, the turn-on energy losses are shown in Figure A-4.

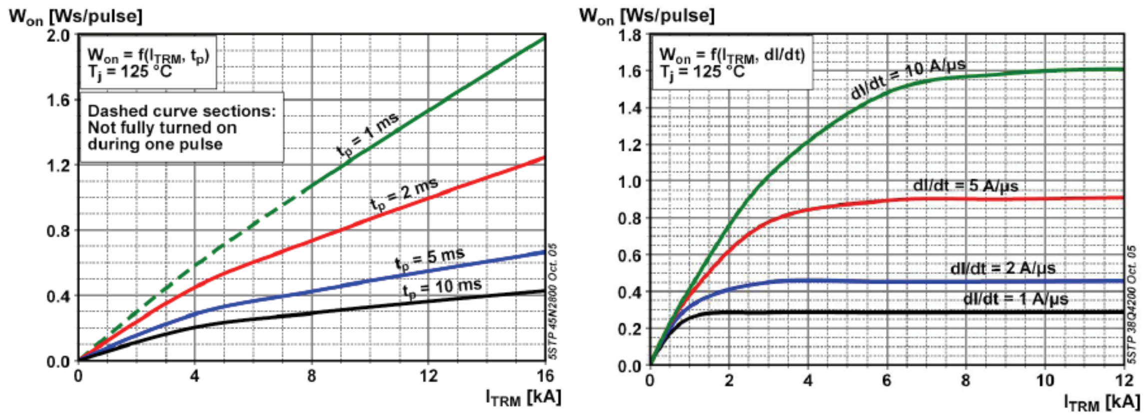

(a) Half-sinusoidal wave (b) Rectangular wave

Figure A-4: ABB 5STP 38Q4200 datasheet power loss during turn-on.

The losses at a different *di*/*dt* at turn-on than those specified can be estimated by considering that the maximum turn-on losses will occur when the rise time for the current will be greater than or equal to the time for the voltage to drop (t_{r0}). Therefore using (A5), a maximum reverse blocking voltage of 4200 V, and the losses in Figure A-4(b), the value of t_{r0} can be estimated as being between 20 µs to 15 µs as the rate of change of current varies between 1 A/µs to 10 A/µs. If the fall-time of the voltage is less than the current rise-time, then the turn-on losses can be estimated as a linear function of *di*/*dt*, so from Figure A-4(b):

$$W_{ON} = 0.15\left(\frac{di}{dt}\right) + 0.15$$

A.1.3 Thyristor Turn-off Losses

The reverse recovery losses during turn-off can be estimated based on the reverse recovery charge (Q_{rr}) and the peak reverse recovery current (I_{rr}). Figure A-5 shows the reverse recovery current and voltage from the ABB 5STP 38Q4200 datasheet and the current and voltage waveform that will be used to estimate the losses.

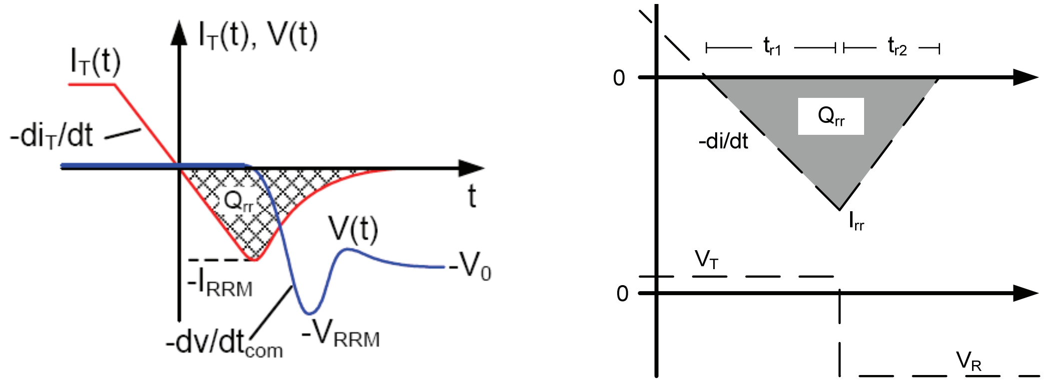

(a) ABB 5STP 38Q4200 datasheet reverse recovery.

(b) Reverse recovery estimate.

Figure A-5: ABB 5STP 38Q4200 current and voltage waveforms at turn-off and estimated waveform.

In Figure A-5(b), the reverse recovery charge is given by Q_{rr} and the peak reverse recovery current is given by I_{rr}. Using this approximation, the peak reverse recovery current is:

$$I_{rr} = \frac{di}{dt} \cdot t_{r1} \tag{A6}$$

The reverse recovery charge will be:

$$Q_{rr} = \frac{I_{rr}\left(t_{r1} + t_{r2}\right)}{2} \tag{A7}$$

From the datasheet for ABB 5STP 38Q4200 thyristors, the reverse recovery charge and peak reverse recovery current are shown in Figure A-6.

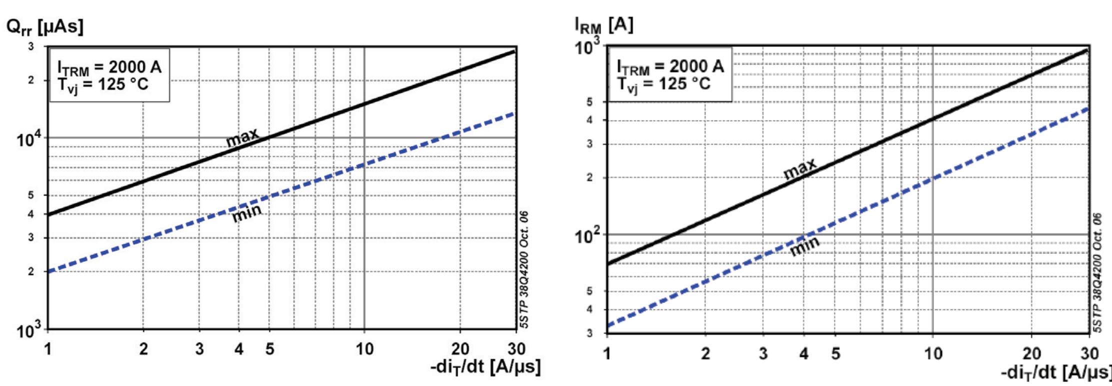

(a) Reverse recovery charge.

(b) Peak reverse recovery current.

Figure A-6: ABB 5STP 38Q4200 datasheet reverse recover charge and peak current.

Therefore if di/dt is known, then Q_{rr} and I_{rr} can be obtained from Figure A-6 and therefore the time t_{r2} will be given by:

$$t_{r2} = \frac{2Q_{rr}}{I_{rr}} - \frac{I_{rr}}{\frac{di}{dt}} \tag{A8}$$

Therefore the reverse recover losses per cycle will be given by:

$$W_{RR} = \int v(t)i(t)dt = \frac{I_{rr}t_{r2}}{2}V_R \tag{A9}$$

A.2 IGBT Losses

IGBTs are often hard switched at non-zero currents and voltages and therefore an estimation of the switch losses should include conduction losses, turn-on losses, and turn-off losses. In many circuits, IGBTs include a parallel freewheeling diode to allow reverse current flow that will result in reverse recovery losses when it is turned off.

A.2.1 IGBT Conduction Losses

The steady state conduction losses during the on-state will depend on the voltage drop across the IGBT when on (V_T) and the current through the IGBT. When current is flowing through the reverse diode then the losses will depend on the diode voltage drop and the current. The on-state voltage drop from the collector to the emitter can be estimated as a DC voltage source in series with a resistance, given by:

$$V_{CE\_ON} = V_{T0} + R_{CE}I_C \tag{A10}$$

These parameters can be estimated from the datasheet information. For an ABB 5SNA 2400E170100 IGBT, the collector current is shown in Figure A-7.

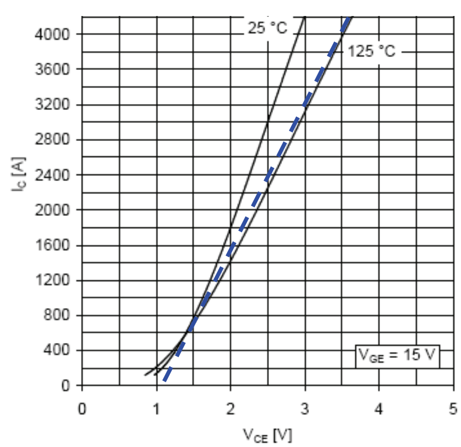

Figure A-7: ABB 5SNA 2400E170100 datasheet collector current vs. collector emitter voltage.

The dashed line in Figure A-7 represents the estimated collector current characteristic, and V_{T0} is the voltage when the current crosses zero and R_{CE} is the slope of the line. In a similar way, the forward current through the freewheeling diode can be approximated based on the datasheet information. The current and voltage relationship of the ABB 5SNA 2400E170100 freewheeling diode are shown in Figure A-8.

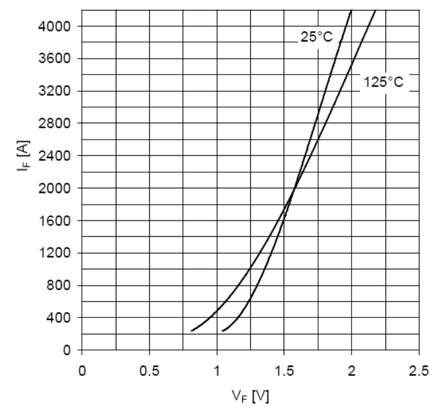

Figure A-8: ABB 5SNA 2400E170100 freewheeling diode characteristics.

The voltage drop in the freewheeling diode during conduction can be approximated as:

$$V_F = V_{F0} + R_{DF} I_F \tag{A11}$$

The off-state power is determined by the voltage across the IGBT and the leakage current. For the ABB 5SNA 2400E170100, it is given as the collector cut-off current which is between 12-120 mA (for temperatures from 25-125˚C). The conduction losses of an IGBT over one switching cycle will be given by:

$$W_{cond} = \int_0^{t_{IGBT\_ON}} I_{IGBT\_ON} V_{CE} dt + \int_0^{t_{DIODE\_ON}} I_F V_F dt + \int_0^{t_{OFF}} I_{cutoff} V_{OFF} dt \tag{A12}$$

A.2.2 IGBT Switching Losses

IGBT switching losses can be approximated with the following formula:

$$W_{sw} = \frac{1}{2} V_c I_c \left(t_{sw\_ON} + t_{sw\_OFF}\right) \tag{A13}$$

where V_c and I_c are the collector voltage and current, t_{sw_ON} is time for the current rise and the voltage to fall when it is switched on, and t_{sw_OFF} is the time for the voltage to rise and the current to fall when it is switched off.

Switching losses can be estimated by linearizing the switching losses given in the IGBT datasheet. For the ABB 5SNA 2400E170100, the switching losses during turn-on and turn-off are given for a set collector voltage, gate resistance, and junction temperature (Figure A-9).

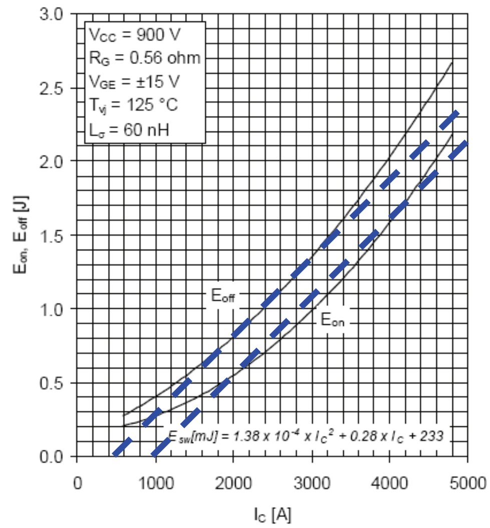

Figure A-9: ABB 5SNA 2400E170100 switching losses.

The dotted lines represent linear approximations of the switching losses, linearized at a collector current of 2000 A (the switches are rated for I_C = 2400 A). The linearized approximation of the losses during turn-on and turn-off can be given by:

$$W_{ON} = A_{ON} + B_{ON} I_C \tag{A14}$$

$$W_{OFF} = A_{OFF} + B_{OFF} I_C \tag{A15}$$

where A_{ON} and A_{OFF} are the zero crossings of the linearized turn-on and turn-off losses and B_{ON} and B_{OFF} are the slopes. A more accurate estimate of the combined switching losses for various conductor currents may be given in datasheet in the form:

$$W_{sw} = \frac{V_{OFF}}{V_{cc}}\left(AI_C^2 + BI_C + C\right) \tag{A16}$$

where V_{cc} is the datasheet voltage corresponding to the parameters in (A16). Similar multipliers can be used to estimate the losses for different gate resistances and junction temperatures (outlined in [80]).

A.2.3 IGBT Diode Reverse Recovery Losses

Reverse recovery losses in the freewheeling diode can be calculated similar to those for the thyristor. The losses may also be given on the datasheet as a function of the forward current in the form:

$$W_{rr} = \frac{V_{OFF}}{V_{cc}}\left(AI_F^2 + BI_F + C\right) \tag{A17}$$

A.2.4 Diode Losses

Since the diodes will turn on at approximately zero voltage, then the turn-on losses can be assumed to be small. Therefore, an estimate of the diode losses will be the sum of the conduction losses and reverse recovery losses. These can be calculated similarly to the losses in the freewheeling diodes calculated for the IGBT.

A.3 Magnetic Device Losses

Transformer and inductor losses are due to core loss and conduction loss. In general, core losses are independent of the load current, while conduction losses increase by the square of the load current. Factors that influence the losses include the material type and dimensions, operating frequency, voltage and current magnitude, and the harmonics.

Transformer and inductor losses can be grouped under conduction losses and core losses. Conduction losses depend on the resistivity of the coil material, the cross sectional area and length of the conductor, and parasitics. Core losses depend on the type of core, frequency, and flux density. A detailed description of magnetic device losses is in [66,68,58].

A.3.1 Core Losses

The core loss includes hysteresis losses and eddy current losses. Hysteresis loss is given by:

$$P_H = f\int v(t)i(t)dt = fA_c l_m \int_{onecycle} HdB \tag{A18}$$

where f is the operating frequency, A_c and l_m are the core area and length., and H is the magnetic field.

Eddy current losses, from currents induced in the magnetic core, are from i^2R losses in the core and are proportional to the square of the frequency (since by faradays law, the induced voltage is the derivative of the flux). Eddy currents can be reduced by using laminated cores, powdered cores, or core materials with higher resistivity. These cores are often more expensive and saturate more easily.

Based on manufacturer's data, the core loss at a given frequency can be approximated by the Steinmetz equation, where the transformer core losses are given by:

$$P_{loss} = Kf^{\alpha} B_{\max}^{\beta} \qquad (W/kg) \tag{A19}$$

where B_{max} is the saturation flux density, and K, α, and β are based on the datasheet information and depend on the operating frequency. Note that most core loss curves use bipolar flux swings, so for unipolar flux swings then the losses can be approximated by dividing the peak flux density by two [81].

A.3.2 Conduction Losses

The conduction losses can be modelled as a series resistance, where the total power loss (for a transformer) is given by:

$$P_{cond} = I^2 R = \rho\left(I_{LV}^2 \frac{l_{LV}}{A_{LV}} + I_{HV}^2 \frac{l_{HV}}{A_{HV}}\right) \tag{A20}$$

where ρ is the wire resistivity, l is the wire length, and A is the cross sectional area of the wire. The resistivity of copper is 1.724 μΩ-mm at room temperature and increases to 2.3 μΩ-mm at 100˚C. Copper wire resistance in Ω/km can be obtained based on the wire gauge; however, large transformers and inductors often use square conductors for structural reasons.

Other factors that affect the conduction losses include the skin effect (which will limit the size of the cables) and the proximity effect (which induces eddy currents in the cables). Methods to limit these losses include use of Litz wire (which is composed of many insulated strands) and interleaving the primary and secondary windings. When parallel conductors are required (for high current coils), then the conductors may need to be transposed, which may increase the effective space required for the conductor.

Information on transformer and inductor designs is in Appendices B.1 and B.3.

A.4 Capacitor Losses

For DC capacitors, the losses will be mostly due to leakage through the dielectric resistance. This can be estimated using datasheet information. The dielectric resistance (in MΩ x μF) of Vishay high voltage DC capacitors is shown in Figure A-10.

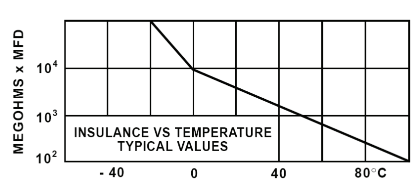

Figure A-10: Vishay high voltage DC capacitor dielectric resistance.

For AC capacitors and those used at higher frequencies such as resonant converters, a typical capacitor model consists of a series resistance and inductance. Since capacitor losses will often vary over the capacitor lifetime, the datasheet may list the power losses per kVAR over a period of time. The losses of Vishay ESTAfilm capacitors (capable of operating at medium frequencies) are shown in Figure A-11.

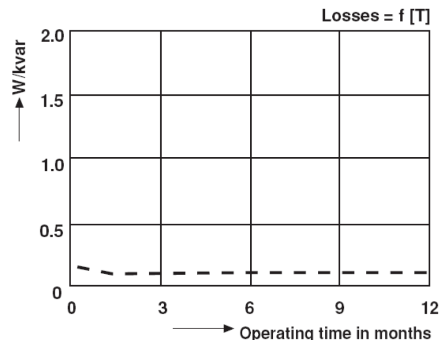

Figure A-11: Vishay medium frequency capacitor losses.

APPENDIX B. MAGNETIC DESIGN

B.1 Transformer Design

The most cost effective 3-phase transformer designs use a single 3-phase core, as shown in Figure B-1. Large transformers may be constrained by the height of the core (due to transportation difficulties), and sometimes require 5-leg designs or even separate single phase transformers; however, since the maximum power of a wind turbine is usually less than 5 MW, a three-phase design using three legs interconnected at the top and bottom by yokes of similar dimensions should be practical for most installations.

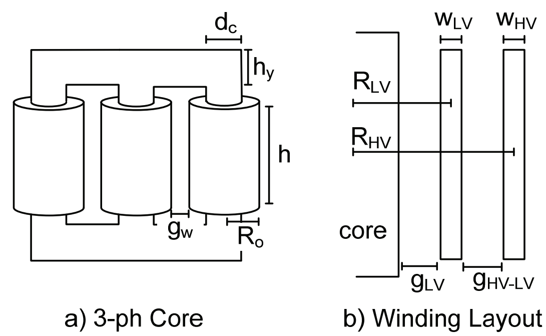

Figure B-1: 3-Leg transformer and winding layout.

The dimensions shown in Figure B-1 are the inter-winding gap (g_w), the core diameter (d_c), the yoke height (h_y), the LV gap (g_{LV}), the gap between the HV/LV windings ($g_{HV\text{-}LV}$), the LV winding width (w_{LV}), the HV winding width (w_{HV}), the height of the LV and HV windings (h), the outer wind radius (R_o), and the mean radius of the HV and LV windings (R_{LV} and R_{HV}).

The design of the transformer must ensure that the flux density of the core is below the saturation flux density of the core material. The flux in the core depends on the transformer magnetizing current, and using Faraday's law, can be related to the primary transformer voltage:

$$v_1 = n_1 \frac{d\Phi}{dt} = \frac{n_1}{R_{mag}} \frac{d\left(n_1 i_1 + n_2 i_2\right)}{dt} = L_{mag} \frac{di_{mag}}{dt} \tag{B1}$$

where v_1 is the primary voltage, n_1 and n_2 are the primary and secondary turns, Φ is the magnetizing flux through the core, R_{mag} is the magnetic reluctance, and L_{mag} is the magnetizing inductance related to the primary side. Using ampere's law, then the main transformer design equation, which relates the flux density in the core to the integral of the voltage (volt-seconds), can be obtained:

$$\int_T v_1 dt = L_{mag} i_{mag} = \frac{L_{mag} \Phi R_{mag}}{n_1} = n_1 B A_c \tag{B2}$$

where, B is the flux density, and A_c is the cross-sectional area of the core. The maximum flux density will occur over half of the period, so that:

$$B_{\max} = \frac{1}{\sqrt{2}\pi} \frac{V_w}{n A_c f} \tag{B3}$$

The maximum value of B depends on the permeability of the core material. The most common core material for distribution transformers is grain oriented silicon steel, which saturates at a flux density of around 2 T. From (B3), then choosing a core material with a high maximum flux density will allow a reduction in the product of the winding turns and the core area, the selection of which is a trade-off between the core and conductor size.

The winding material is usually copper, although aluminum can be beneficial to reduce the transformer weight and depending on the material cost [82]. The thickness of the winding will depend on the rated current as well as mechanical requirements. To reduce losses, the cross sectional area of the cable can be increased, although the maximum area is limited by the skin depth (especially at higher frequencies). To reduce skin effect losses, parallel wires or Litz wire can be used when the required cable diameter exceeds the skin depth (8.47 mm at 60 Hz). Parallel conductors may need to be transposed to avoid losses due to circulating currents, which will increase the effective conductor thickness.

The core losses consist of hysteresis losses and eddy current losses. To reduce eddy currents in the transformer core, it is normally composed of thin laminated sheets. Further reduction of the core losses requires decreasing the core length, operating at low flux densities, or with low loss materials.

The losses of different core materials vary depending on the frequency, maximum flux, and also between various manufacturers. Table B-1 shows a comparison of approximate losses at 60 Hz for different thicknesses of silicon steel and for Metglas amorphous steel [83-86]:

Table B-1: Core losses of various materials and saturation levels.

	B_{max} = 1.3 T	B_{max} = 1.5 T	B_{max} = 1.7T
M-2 (0.18 mm)	0.54 W/kg	0.89 W/kg	-
M-3 (0.23 mm)	0.58 W/kg	0.93 - 1.08 W/kg	1.19 - 1.54 W/kg
M-4 (0.27 mm)	0.67 W/kg	0.84 - 1.17 W/kg	1.25 - 1.72 W/kg
Metglas 2605SA1	0.16 W/kg	0.38 W/kg	-

Metglas is currently rated up to 1.65 T and other low loss alloys with higher saturation densities are being developed [87]. Amorphous core materials were usually only used in low power transformers, but higher powers are now offered (Hitachi offers 3.0 MW amorphous core transformers [88]).

The amount of leakage flux will influence the voltage regulation and fault current. High leakage flux can lead to voltage regulation problems leading to large voltage differences between no-load and full load operation; however, this may be required in some cases to limit the fault current. Generally the leakage flux is designed for around 10%. For two-winding transformers with primary and secondary windings wound around the same core, the leakage flux can be estimated as [68]:

$$X_{leakage} = \frac{2\pi f L}{X_B} = \frac{(2\pi)^2 \mu_0 n^2 f}{X_B (h+s)} \left(\frac{1}{3} \left(R_{HV} w_{HV} + R_{LV} w_{LV} \right) + R_{HV-LV} w_{HV-LV} \right) \tag{B4}$$

where X_B is the base reactance per phase of the transformer, n is the number of turns, and the other parameters are shown in Figure B-1. The fringing flux is accounted for with the parameter s, which is approximated as [68]:

$$s = 0.32(R_o - R_c) \tag{B5}$$

where R_o is the radius of the end of the HV coil and R_c is the radius of the core.

Insulation is required around the individual conductors in a coil, between the windings and the core, and between adjacent windings. The thickness and insulation type depends on the voltage of the winding, and thermal requirements. A transformer voltage rating at above 10% rated voltage is generally required to meet grid specifications, although the insulation must also be able to handle short term overvoltages. Normally a combination of oil and paper is used, with the oil increasing the electrical strength of the paper as well as providing improved cooling capabilities. It is common to use a distance of 1 kV/mm for the transformer design, although the actual insulation electrical strength is much higher [67].

The transformer must also be designed to be able to withstand short term surges and transients from switching and lightning. The structural design of the transformer must be able to withstand the various mechanical forces that occur during fault conditions. Overload and cooling should also be considered, although since it will only be connecting the wind turbine to the grid, then there may be minimal overload requirements.

An example design will be performed using a 3 MW turbine with a 1000 V output at 60 Hz (similar to the Vestas V90 asynchronous generator based wind turbine or the GE 3.0sl permanent magnet based wind turbine). The power output of the turbine is zero when the wind speed is below 4 m/s and is fixed at 3 kW when the wind speed is above 15 m/s and below 25 m/s. The power output of the wind turbine between 4 m/s and 15 m/s will be approximated using a cubic equation, given by:

$$P_T(U)=\begin{cases} 743.3-490.5U+90.3U^2-3.17U^3 & 4<U<15 \\ 3000 & 15<U<25 \end{cases} \tag{B6}$$

where U is the wind speed and the power is measured in kW. The resulting approximate power output of the wind turbine is shown in Figure B-2.

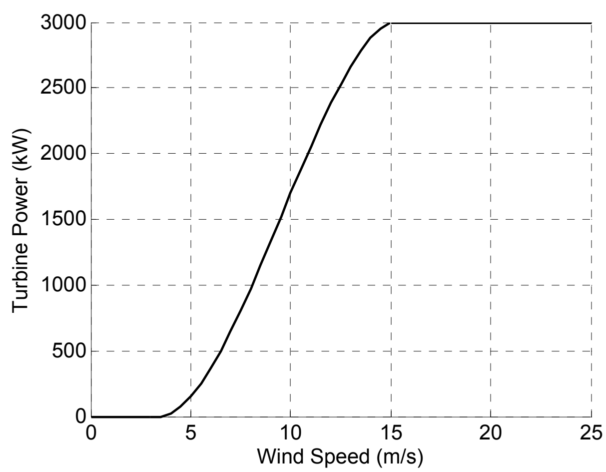

Figure B-2: Estimated wind turbine power curve.

The transformer will be designed to connect the wind turbine to a 30 kV medium voltage grid and will be rated for 3 MVA. To minimize the cost over the lifetime of the transformer, a cost function will be used that considers the material cost of the core and windings, and the cost of core and copper losses over the total lifetime of the wind turbine (assumed to be 20 years). Although other costs such as the transformer case, insulation, bushings, and maintenance will vary depending on the design, these will be assumed constant and will not be included in the cost function.

B.1.1 Conductor Design

The mass of the conductor is approximately:

$$M_{cu} = 3\left(d_{cu} MLT_{LV} n_{LV} A_{cuLV} + d_{cu} MLT_{HV} n_{HV} A_{cuHV}\right) \tag{B7}$$

where d_{cu} is the density of the copper winding, n is the number of turns, A_{cu} is the cross sectional area of the conductor, and MLT is the mean length per turn. The area of the LV conductor will be given by:

$$A_{cuLV} = \frac{I_{LV\max}}{J_{LV}} n_{LV} = h_{LVwind} w_{LVwind} \tag{B8}$$

where J_{LV} is the current density in the wire. The area of the high voltage conductor will evaluated similarly. The current density in the wire will be affected by the type of transformer cooling, but is generally between 2-4 A/mm^2 [83]. To limit losses due to the skin effect, multiple parallel conductors should be used for the LV winding, which will require transposition. If disk windings are used, appropriate spacing is required between the disks to improve the heat conduction and for insulation. To simplify the design equations, the length and width of both HV and LV coils will be increased by a factor of 1/0.6 to account for insulation and cooling duct space. In addition the insulation around the coils will be set to 35 mm around the HV winding, and 5 mm between the LV winding and the core.

Besides the resistivity and wire design, the wind turbine conduction losses will depend on the wind characteristics in the area and the wind turbine power output characteristics. The conduction losses are given by:

$$W_{conduction} = 3\rho_{cu}\left(\frac{\left(MLT_{LV} \cdot n_{LV}\right)}{A_{cuLV}} I_{LV}^2(t) + \frac{\left(MLT_{HV} \cdot n_{HV}\right)}{A_{cuHV}} I_{HV}^2(t)\right) \tag{B9}$$

where ρ_{cu} is the resistivity of copper. The current into the transformer is a function of time and will vary depending on the speed of the wind. The primary and secondary currents are related by the transformer turns ratio so that:

$$I_{LV}(t) = \frac{n_{HV}}{n_{LV}} I_{HV}(t) \tag{B10}$$

If the wind speed is estimated using a Rayleigh distribution, then the probability density function of the wind speed is given by:

$$p(U) = \frac{\pi}{2}\left(\frac{U}{\overline{\overline{U}}}\right) e^{-\frac{\pi}{4}\left(\frac{U}{\overline{\overline{U}}}\right)^2} \tag{B11}$$

where $\overline{U}$ is the mean velocity of the wind. Using (B6), the expected value of the square of the current will therefore be given by:

$$E_{I^2}(U) = \int_4^{25} I^2 p(U) dU = \int_4^{25} \left(\frac{P_T(U)}{\sqrt{3}V_{LV}}\right)^2 \frac{\pi}{2}\left(\frac{U}{\overline{\overline{U}}}\right) e^{-\frac{\pi}{4}\left(\frac{U}{\overline{\overline{U}}}\right)^2} dU \tag{B12}$$

This result of this integral can be used to determine the expected turbine losses depending on the wind characteristics.

B.1.2 Core Design

The mass of the core is given by:

$$M_{core} = M_{legs} + M_{yokes} \tag{B13}$$

where the mass of the legs and yokes can be approximated as:

$$M_{legs} = 3d_{fe}A_{core}(h_{LV} + 2h_{ins})$$
$$M_{yokes} = 2d_{fe}A_{core}(3d_{core} + 2g_{LV} + 2w_{LV} + 2g_{HVLV} + 2w_{HV} + g_w)$$

and where d_{fe} is the density of the steel in kg/m^2. The core losses are usually approximated by fitting the datasheet graph of the core losses vs. frequency and maximum flux density given by the Steinmetz equation:

$$W_{core} = Kf^{\alpha} B_{\max}^{\beta} \tag{B14}$$

where K, α, and β are constants. Despite higher losses at higher B_{max}, it is often advantageous to operate at higher saturation levels since this will allow minimization of the product of the turns and the core area, which will decrease material cost, core losses, and conduction losses. A comparison will be made of transformers operating at a set B_{max}, close to the saturation flux density, given in Table B-1. The frequency will also be assumed constant at 60 Hz.

B.1.3 Cost Function

The cost minimization function will be:

$$\underset{\underline{x}}{Min}\ \{Conductor\ Cost + Core\ Cost + Cost\ of\ Losses\} \tag{B15}$$

where the conductor cost is given by:

$$C_{cond} = C_{cu}M_{cu} \tag{B16}$$

The core cost is given by:

$$C_{core} = C_{fe} M_{fe} \tag{B17}$$

The cost of losses can be related to the material costs using the present value of an annuity:

$$C_{loss} = \frac{24 \cdot E_{loss(kWh)}}{i}\left(1 - \frac{1}{(1+i)^N}\right) \tag{B18}$$

where i is the interest rate and N is the time period. The minimization variable, $\underline{x}$, will be:

$$\underline{x} = \left[w_{LV} \;\; h_{LV} \;\; w_{HV} \;\; n_{LV} \;\; d_{core} \;\; J_{LV} \;\; J_{LV}\right] \tag{B19}$$

The current densities (J_{LV} and J_{HV}) will be constrained to be less than 4 A/mm^2. The height of the HV winding will be set to be $0.95h_{LV}$, as is recommended in [68]. The leakage reactance will be set to 10%.

B.2 Amorphous Core Transformer Comparison

For the base case, the electricity price will be set to \$0.10/kWh and the daily interest rate and time period for the annuity will be 5%/365 over 20 years. The material information, including estimated cost ranges for silicon and amorphous steel and copper, is in Table B-2.

Table B-2: Material information base case.

Grain Oriented Silicon Steel	Amorphous Steel (Metglas)	Copper
B_{max} = 1.7 T	B_{max} = 1.4 T	d_{cu}=8.94 g/cm^3
d_{fe}=7.65 g/cm^3	d_{fe}=7.18 g/cm^3	ρ_{cu}=1.72x10^{-8} Ω/m
Cost = \$4/kg	Cost: \$4/kg	Cost: \$8/kg
Losses: 1.2 W/kg	Losses: 0.4 W/kg	

The resulting material weight and losses for transformer designs optimized for a range of average wind speeds are shown in Figure B-3. The curves show losses and weights of the cores and conductors for transformers designed with amorphous steel and silicon steel cores.

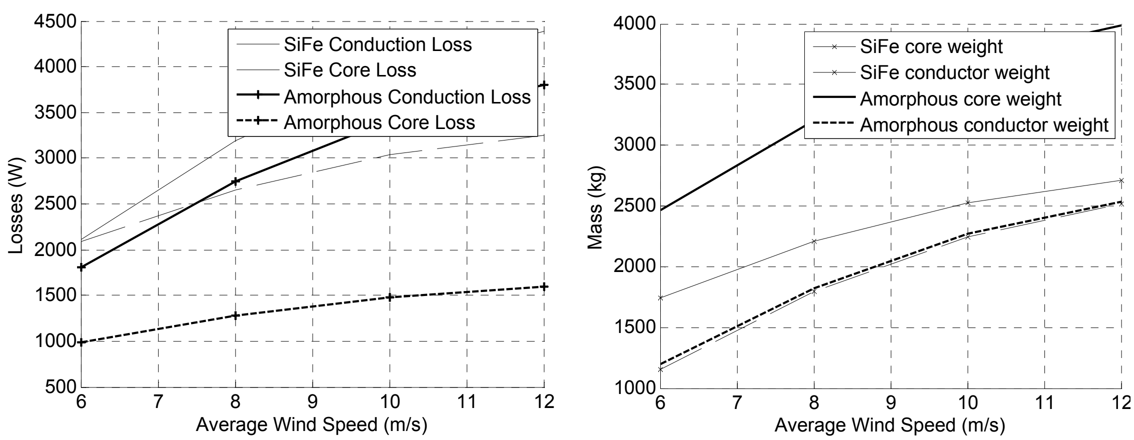

Figure B-3: Transformer core and conductor losses and material mass.

The overall present value of the cost of both the transformer core and conductor materials and the losses over the 20 year lifetime of the wind turbine are shown in Figure B-4 for transformer designs optimized for a range of average wind speeds.

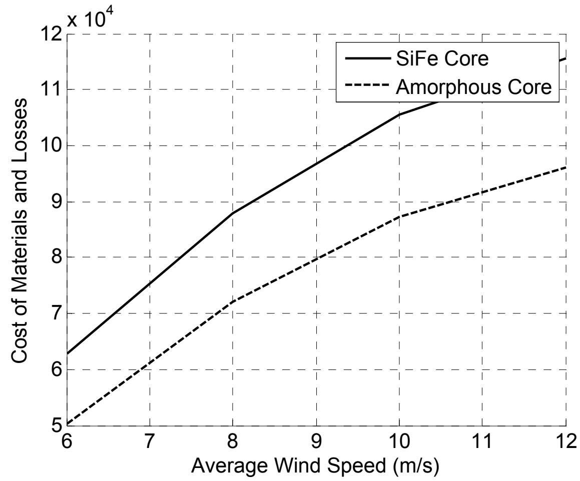

Figure B-4: Core and conductor material costs.

The efficiency of a transformer designed for a wind turbine in an area with an average wind speed of 8 m/s is shown for various loading levels (from 0.1 to 1 pu) in Figure B-5.

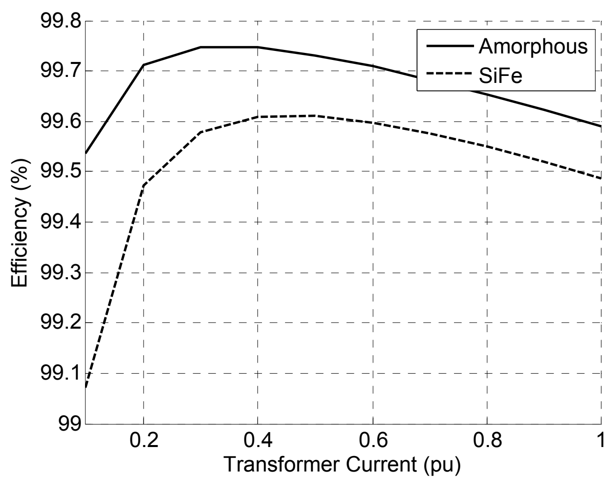

Figure B-5: Transformer efficiency for a design with an average wind speed of 8 m/s.

To show the effect of varying costs of core materials, the overall cost of materials and losses over the transformer lifetime is shown in Figure B-6 for designs based on core material prices ranging from 0.5-2.5 times the base costs (in Table B-2).

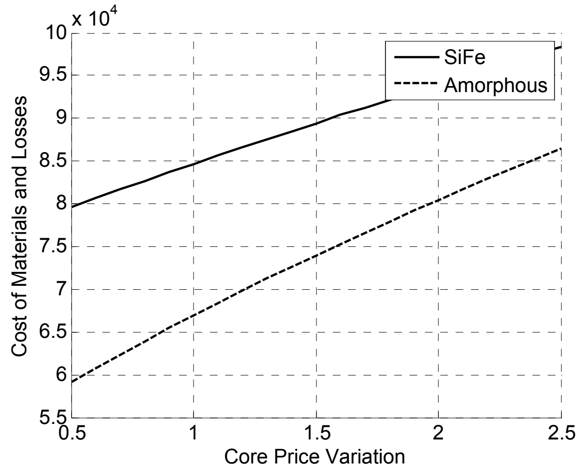

Figure B-6: Transformer cost at varying core price variation.

The core price variation is a multiple of the base case used in Table B-2. Figure B-6 shows that silicon steel cores are preferable at higher amorphous core prices and lower silicon steel prices (as in the past).

The losses and cost results demonstrate the cost benefits of amorphous core transformers, however it should be noted that this efficiency analysis does not take into account all the transformer losses (such as due to the skin effect and proximity effect), the structural design of the transformer, and the insulation and transformer externals. This analysis could be used as a basis for a more detailed design that includes the other components.

To show the effect of designing for the correct wind forecast, Figure B-7 shows the cost of the core and conductor and the cost of losses various transformers over a range of wind speeds. The transformers were designed for wind speeds of 6, 8, and 10 m/s.

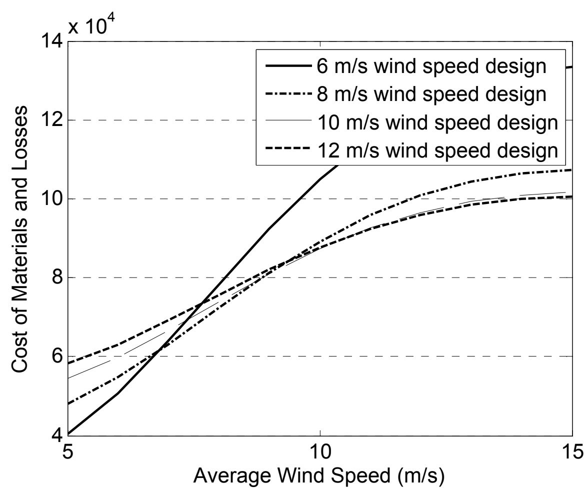

Figure B-7: Transformer designs for various mean wind speeds.

As can be seen from Figure B-7, the impact of designing the transformer for a specific wind speed is greatest when the average wind speed is low. When the wind speed is between 7-8 m/s, the cost variation is around 3-4%. Since these cost savings are small, individual transformer design may only be important when designing a large wind farm where many wind turbines will be operating at a similar average wind speed.

B.3 Inductor Design

The main inductor design equation is based on Ampere's law, so that:

$$nI = \Phi\left(\frac{l_c}{\mu A_c}\right) \tag{B20}$$

where n is the number of turns, I is the current flowing through the inductor, Φ is the flux in the core, l_c is the mean length around the core, μ is the permeability of the core, and A_c is the core area. Using Faraday's law then:

$$v(t) = n\frac{d\Phi(t)}{dt} = \frac{n^2}{\left(\frac{l_c}{\mu A_c}\right)}\frac{di(t)}{dt} \tag{B21}$$

The inductance is defined as:

$$L = \frac{n^2}{\left(\frac{l_c}{\mu A_c}\right)} \tag{B22}$$

The value of μ is equal to $\mu_0\mu_r$, where μ_0 is the permeability of free space and μ_r is dependent on the core material. For grain oriented silicon steels, μ_r can be around 50000, but it is highly dependent on the temperature of the core. Therefore to keep the inductance stable for varying temperatures, most inductors are designed with an air gap in the core, so that (B20) becomes:

$$nI = \Phi\left(\frac{l_c}{\mu A_c} + \frac{l_g}{\mu_0 A_c}\right) = \Phi\left(R_c + R_g\right) \cong \Phi R_g \tag{B23}$$

The maximum flux density will depend on the core material. The flux density in the inductor will be the sum of the AC and DC flux density. The AC flux density can be calculated similar to a transformer and will be given by:

$$B_{AC} = \frac{1}{nA_c} \int_T V_L(t) dt \tag{B24}$$

The maximum DC flux density can be obtained using (B23), is given by:

$$B_{DC} = \frac{nI_{\max}}{A_c\left(R_c + R_g\right)} \cong \frac{\mu_0 n I_{\max}}{l_g} \tag{B25}$$

In order to design the inductor, a similar minimization function can be used as in Appendix B.2, so that the cost of the core, conductor, and losses are minimized. This is given by:

$$\underset{\underline{x}}{Min} \left\{ Conductor\,Cost + Core\ Cost + Cost\ of\ Losses \right\} \tag{B26}$$

where the conductor cost is given by:

$$C_{cond} = C_{cu} M_{cu} \tag{B27}$$

The core cost is given by:

$$C_{core} = C_{fe} M_{fe} \tag{B28}$$

The cost of losses can be related to the material costs using the present value of an annuity, so that:

$$C_{loss} = \frac{24 \cdot E_{loss(kWh)}}{i} \left(1 - \frac{1}{(1+i)^N} \right) \tag{B29}$$

where i is the interest rate and N is the time period. The minimization variable, $\underline{x}$, will be:

$$\underline{x} = \left[w_w \ \ l_w \ l_g \ \ d_{core}\, n \ \ J \ \ B \right] \tag{B30}$$

where w_w is the width of the coil, l_w is the length of the coil, l_g is the length of the airgap, d_{core} is the diameter of the core, n is the number of turns, and J is the current density.

Similar to the transformer design, the losses are dependent on the core and copper losses. If the inductor design is similar to Figure B-1, but only consisting of one vertical core with a single winding around it, then if l_{wg} is the length of the insulation between the coil and the core, the mass of the core can be approximated as:

$$M_{fe} = d_{fe} \pi \left(\frac{d_{core}}{2} \right)^2 \left(2w_w + 2l_w + 8l_{wg} + 4d_{core} - l_g \right) \tag{B31}$$

where d_{fe} is the density of the steel. The mass of the conductor can be approximated as:

$$M_{cu} = d_{cu} \pi \left(d_{core} + 2l_{wg} + \frac{w_w}{k} \right) n A_{cu} = d_{cu} (MLT) n A_{cu} \tag{B32}$$

where d_{cu} is the density of copper, k is a constant dependent on the insulation, MLT is the mean length per turn, and A_{cu} is the area of the copper wire, given by:

$$A_{cu} = \frac{I}{J} \tag{B33}$$

where J is the current density in the wire. The maximum current density will be dependent on the type of insulation and cooling. The conductor losses can be approximated as:

$$P_{conduction} = \rho_{cu}\left[\frac{(MLT \cdot n)}{A_{cu}} I^2(t)\right] \tag{B34}$$

where ρ_{cu} is the resistivity of copper. Depending on the frequency of operation, the resistance of the wires will vary due to the skin effect and the proximity effect. To avoid high losses at higher frequencies, parallel conductors or Litz wire may be required, which will increase the cost and amount of insulation. These effects will need to be considered in a detailed design, but will not be modeled in this analysis.

Similar to transformers, the losses can be approximated using the Steinmetz equation:

$$P_{core} = Kf^{\alpha} B_{\max}^{\beta} M_{fe} \tag{B35}$$

Estimating based on Figure 18, the core loss for Nippon 0.23 mm steel and Metglas 2605SA1 amorphous steel, the parameters will be approximately:

Table B-3: Core parameter estimation.

	K	α	β
Nippon 0.23 mm steel	0.00051	1.615	1.844
Metglas 2605SA1 amorphous steel	0.00011	1.554	1.486

As mentioned in Section A.3.1, since the flux will be unipolar, then the core losses should be approximately half of what is expected based on the estimated formula. In order to limit the weight of the inductor, the maximum flux density will be set between 1.2-1.7 T.

B.3.1 Air Core Inductors

Air core inductors may offer advantages in some designs. These inductors have no core losses, do not risk core saturation during fault conditions, and may be lighter and smaller. The conduction losses will be higher since the coil will require more turns to achieve the same inductance as a steel core transformer.

The most basic air core inductor design is a toroid, where similar design equations can be used as in Appendix B.3. A section of the toroid is shown in Figure B-8, where w_{cui} and w_{cuo} are the widths of the winding on the inside and outside of the core, l_{cu} is the circumference of the inner part of the winding and d_c is the diameter of the core. For the minimization function, only the width of the winding on the inside of the core will be used.

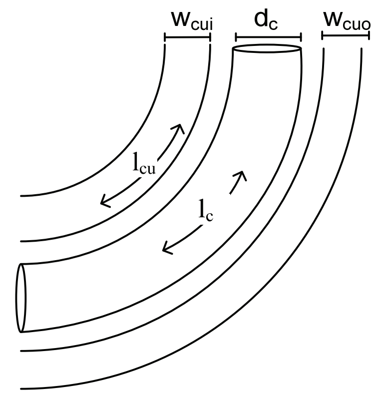

Figure B-8: Section of a toroid inductor.

Similarly to the transformer design, the actual conductor width and length will be increased to account for insulation. The mean circumference of the core is given by:

$$l_c = 2\pi\left(\frac{l_{cu}}{2\pi k} + \frac{d_c}{2}\right) \tag{B36}$$

where k is the insulation factor for the winding. The mass of the conductor can be approximated as:

$$M_{cu} = d_{cu}\pi(w_{cui} + d_c)nA_{cu} = d_{cu}(MLT)nA_{cu} \tag{B37}$$

Similar design steps to those in Appendix B.3 can then be used to design the toroid air core inductor to minimize cost.

APPENDIX C. RESONANT CONVERTER ANALYSIS

C.1 External Inductance Resonant Converter

The main converter design equations and converter characteristics are given in Section 4.1. This appendix contains further details of the converter operation.

C.1.1 Converter Peak and Average Input Current

In order to evaluate the current, as well as the power transfer where $t = t_0$ is the initial switching time, $t = t_B$ is the time when the voltage of the resonant capacitor is equal to the voltage at Terminal 2, $t = t_C$ is the time for the resonant current decreases to zero (for discontinuous mode operation) or the beginning of the next switching cycle (for continuous mode operation).

The time to the peak current into the converter can be obtained using the derivative of the resonant current with an initial condition of I_0=0. For discontinuous operation:

$$\frac{di(t)}{dt} = \frac{V_1 - V_{cr0}}{Z_0}\cos(\omega_0 t) = 0 \tag{C1}$$

$$t = \frac{T_0}{4} \tag{C2}$$

where:

$$V_{cr} = V_1$$
$$V_{cr0} = -V_2$$

Therefore:

$$I_{1peak} = \frac{V_1 + V_2}{Z_0} \tag{C3}$$

For the continuous operation then I_0 is non-zero and therefore:

$$\frac{di(t)}{dt} = -I_0 w_0 \sin(\omega_0 t) + \frac{V_1 - V_{cr0}}{Z_0} w_0 \cos(\omega_0 t) = 0 \tag{C4}$$

$$\tan(\omega_0 t) = \frac{V_1 - V_{cr0}}{I_0 Z_0} \tag{C5}$$

Since the current operation changes depending on when the voltage reaches the terminal voltage, then an estimate of the minimum current value (I_0) and the peak current value (I_p) depending on the converter and the switching frequency can be made by estimating that the current is symmetric around the peak current. Therefore:

$$t_p = \frac{t_s}{2} \tag{C6}$$

and:

$$I(t_s) = I_0 = I_0 \cos\left(\omega_0 \frac{t_s}{2}\right) + \frac{V_1 + V_2}{Z_0} \sin\left(\omega_0 \frac{t_s}{2}\right) \tag{C7}$$

and:

$$I_0 = \frac{V_1 + V_2}{Z_0} \frac{\sin\left(\omega_0 \frac{t_s}{2}\right)}{1 - \cos\left(\omega_0 \frac{t_s}{2}\right)} \tag{C8}$$

Therefore:

$$I(t_p) = I_0 \cos(\omega_0 t_p) + \frac{V_1 + V_2}{Z_0} \sin(\omega_0 t_p) \tag{C9}$$

Squaring $I(t_p)$ and subbing in for I_0 and using the estimate that $t_p = ½t_s$ results in:

$$I(t_p) = \left(\frac{V_1 + V_2}{Z_0}\right)\left[\frac{2}{1 - \cos(\omega_0 t_s)}\right]^{0.5} \tag{C10}$$

This value will always be greater than the peak current below the resonance frequency, although the difference between the peak value and the minimum current (I_p-I_0) will decrease.

The average current will be the integral of the current over one switching cycle, divided by the switching time. For operation below resonance where I_0=0, the average current is:

$$I_{ave} = \frac{2}{T_s} \int_0^{\frac{T_0}{2}} \left(\frac{V_1 + V_2}{Z_0} \sin(\omega_0 t)\right) dt = \frac{4}{T_s \omega_0}\left(\frac{V_1 + V_2}{Z_0}\right) = \frac{4(V_1 + V_2)C_r}{T_s} \tag{C11}$$

For operation above resonance, the average current is:

$$\begin{aligned} I_{ave} &= \frac{2}{T_s} \int_0^{\frac{T_s}{2}} \left(I_0 \cos(\omega_0 t) + \frac{V_1 + V_2}{Z_0} \sin(\omega_0 t)\right) dt \\ &= \frac{2}{T_s}\left[\frac{I_0}{\omega_0} \sin\left(\omega_0 \frac{T_s}{2}\right) + (V_1 + V_2)C_r\left(1 - \cos\left(\omega_0 \frac{T_s}{2}\right)\right)\right] \end{aligned} \tag{C12}$$

C.1.2 Maximum Power Transfer

Power transfer into the resonant converter will occur when current is flowing through the thyristor switches. Power flow out of the converter will occur when the peak voltage across the resonant capacitor is greater than the DC voltage of the second terminal. The converter input and output currents, as well as the capacitor voltage are shown in Figure C-1 for a converter operating at resonant frequency. The current into the HV terminal (I_2) does not equal the current from the LV terminal (I_1) due to the HV inductor.

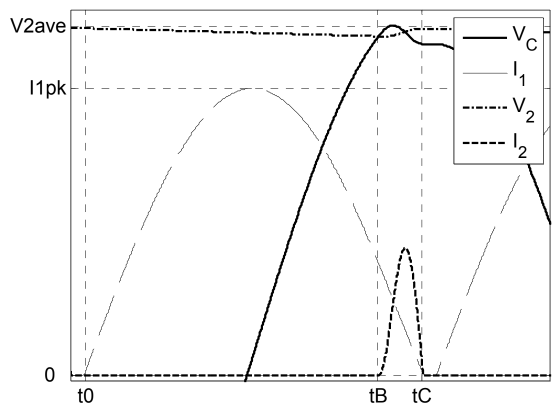

Figure C-1: Converter input and output currents at resonant frequency

The energy flows out of the converter between t_B and t_C (in Figure C-1) where the voltage of the resonant capacitor is equal to the voltage across terminal 2 (assuming the diode resistance is small). In this case the current through the resonant inductor can be obtained from:

$$V_1 - V_2 = L\frac{di_L(t)}{dt} \tag{C13}$$

$$i_L(t) = I_L(t_B) + \int_{t_B}^{t} \frac{V_1 - V_2}{L} dt = I_L(t_B) + \frac{V_1 - V_2}{L}(t - t_B) \tag{C14}$$

At time $t_{B,}$ $V_{cr} = V_2$ therefore:

$$V_C(t_B) = V_2 = V_1 - (V_1 - V_2)\cos(\omega_0 t_B) \tag{C15}$$

$$\frac{V_1 - V_2}{V_1 + V_2} = \cos(\omega_0 t_B) \tag{C16}$$

therefore:

$$\sin(\omega_0 t_B) = \frac{\sqrt{4V_1V_2}}{V_1 + V_2} \tag{C17}$$

and:

$$I(t_B) = \frac{V_1 + V_2}{Z_0}\sin(\omega_0 t_B) = \frac{\sqrt{4V_1V_2}}{Z_0} \tag{C18}$$

At time t_C, $I(t_C) = 0$ therefore:

$$I(t_C) = 0 = I(t_B) + \frac{V_1 - V_2}{L}(t_C - t_B) \tag{C19}$$

and if t_B is set to 0 then:

$$t_C = -I(t_B)\frac{L}{V_1 - V_2} \tag{C20}$$

Since the energy flowing out of the converter is given by:

$$E_{out} = \int_{t_B}^{t_C} V_2 I_1(t)dt = V_2 \cdot \int_{t_B}^{t_C} \left[I(t_B) + \frac{(V_1 - V_2)}{L}(t - t_B) \right] dt \tag{C21}$$

then setting t_B to 0:

$$E_{out} = V_2 \cdot \left[\frac{\sqrt{4V_1V_2}}{Z_0}(t_C) + \frac{(V_1 - V_2)}{L}\frac{1}{2}t_C^2 \right] = V_2 \cdot \left[-\frac{4V_1V_2L}{Z_0^2(V_1 - V_2)} + \frac{2V_1V_2L}{Z_0^2(V_1 - V_2)} \right] = 2\frac{V_1V_2^2C}{V_2 - V_1} \tag{C22}$$

In continuous mode operation the switching frequency is greater than the resonant frequency, resulting in a waveform as shown in Figure 26(b).

Assuming steady state conditions where the current at all switching times is equal, then the resulting converter equations at time $t = t_B$, when the voltage across the converter is equal to the output voltage V_2, are given by:

$$I(t_B) = I_0 \cos(w_0 t_B) + \frac{V_1 + V_2}{Z_0}\sin(w_0 t_B) \tag{C23}$$

$$V_{cr}(t_B) = V_2 = V_1 - (V_1 + V_2)\cos(w_0 t_B) + Z_0 I_0 \sin(w_0 t_B) \tag{C24}$$

Since during steady state operating the voltages at the switching time are equal, if the initial time is set to zero then at $T_s/2 = t_C$, the current is given by:

$$L\frac{dI(t)}{dt} = V_1 - V_2 \tag{C25}$$

$$I(t_C) = I_0 = I(t_B) + \frac{V_1 - V_2}{L_r}(t_C - t_B) \tag{C26}$$

and the energy transferred in one half cycle is:

$$E_{out} = \int_{t_B=0}^{t_C} V_2 I_1(t)dt = V_2 \cdot \int_{t_B}^{t_C} \left[I(t_B) + \frac{(V_1 - V_2)}{L}(t) \right] dt$$

$$= V_2 \left[I(t_B)(I_0 - I(t_B)) \frac{L}{(V_1 - V_2)} + \frac{(V_1 - V_2)}{L} \frac{1}{2} (I_0 - I(t_B))^2 \frac{L^2}{(V_1 - V_2)^2} \right] = \frac{V_2}{2} \frac{L}{(V_1 - V_2)} \left[I_0^2 - I(t_B)^2 \right] \quad \text{(C27)}$$

By squaring the resonant voltage and current and summing then:

$$I_B^2 - I_0^2 = \frac{(V_1 + V_2)^2}{Z_0^2} - \frac{(V_2 - V_1)^2}{Z_0^2} = 4 \frac{V_1 V_2}{Z_0^2} \quad \text{(C28)}$$

Therefore:

$$E_{out} = \frac{V_2}{2} \frac{L}{(V_1 - V_2)} \left[4 \frac{V_1 V_2}{Z_0^2} \right] = \frac{2 V_1 V_2^2 C_r}{(V_1 - V_2)} \quad \text{(C29)}$$

Since losses were ignored, then this will also be equal to the power into the converter. This result is the same as for the discontinuous operation and therefore the maximum power output of the converter will be:

$$P_{\max} = E_{in} \cdot 2 f_s = \frac{2 V_1 V_2^2 C}{V_2 - V_1} 2 f_s \quad \text{(C30)}$$

Therefore for fixed voltages at the terminals of the converter, the power output can be varied by adjusting the frequency of the converter. Both converters have the same result, however since the parallel resonant converter does not allow operation above the resonant frequency then the maximum power output will be:

$$P_{\max} = \frac{2 V_1 V_2^2 C}{V_2 - V_1} 2 f_0 \quad \text{(C31)}$$

The voltage ripple on the output capacitor can be obtained using (C29). Assuming a very low load, then the maximum voltage ripple for one pulse will be given by:

$$\Delta V_2 = -1 + \sqrt{\frac{4 V_1 C_r}{(V_2 - V_1) C_2} + 1} \quad \text{(C32)}$$

where C_2 is the output voltage capacitor and ΔV_2 is in pu. This can be used to design the output capacitor depending on the allowable output voltage variation. The output capacitor size will be given by:

$$C_2 = \frac{4 V_1 C_r}{(V_2 - V_1) \Delta V_2 (\Delta V_2 + 2)} \quad \text{(C33)}$$

The LV capacitor can be obtained based on the allowed LV variation and will be given by:

$$C_1 = \frac{1}{\Delta V_1} \int_0^{T_0/2} I_1(t) dt = \frac{1}{\Delta V_1} 2 C_r (V_1 + V_2) \quad \text{(C34)}$$

C.1.3 Converter Input Current and Maximum Power with Parameter Variation

Using the formulas derived for the maximum power and the current variation, the effect due to variation of the converter properties is shown in Figure C-2 to Figure C-5. The resonant capacitance and inductance, as well as the terminal voltages are varied on a base case converter with the following properties:

HV Terminal Voltage	500 kV
LV Terminal Voltage	35 kV
Resonant Capacitance	2.3 μF
Resonant Inductance	3.6 mH
Resonant Frequency	1750 Hz

Each figure shows the input current range into the converter and the maximum output power for fixed terminal voltages. The average current is a dotted line (if shown).

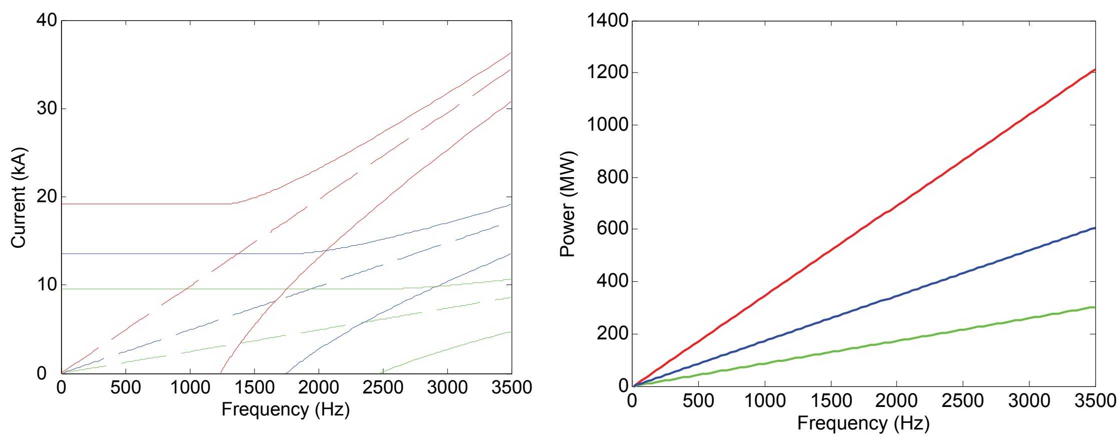

Figure C-2: Effect of capacitor variation on the current and power; blue: base case; red: 2xbase case; green: 0.5xbase case.

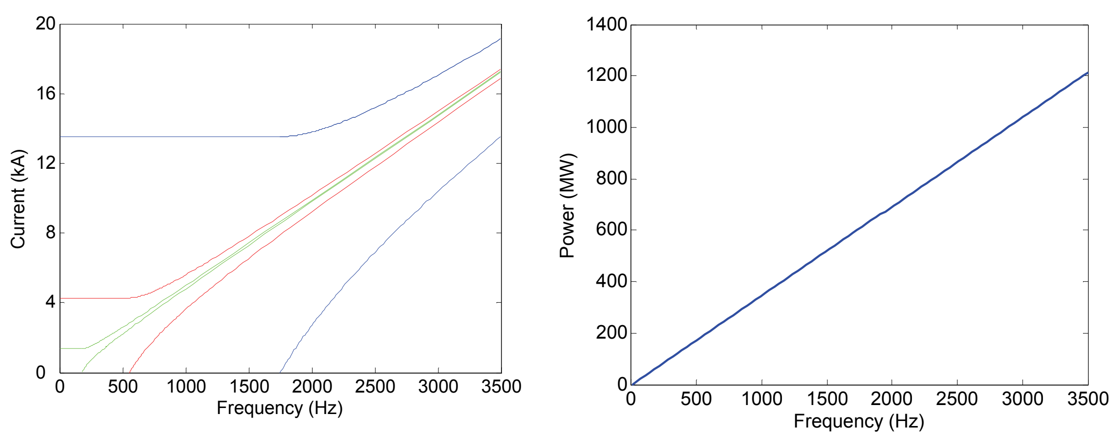

Figure C-3: Effect of inductor variation on the current and power; blue: base case; red: 10xbase case; green: 100xbase case.

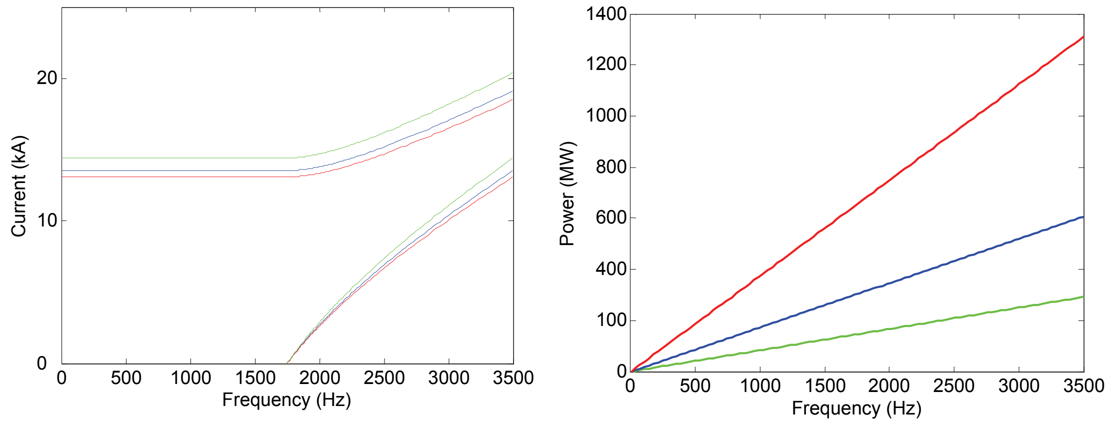

Figure C-4: Effect of varying the low voltage terminal voltage on the current and power; blue: base case; red: 0.5xbase case; green: 2xbase case.

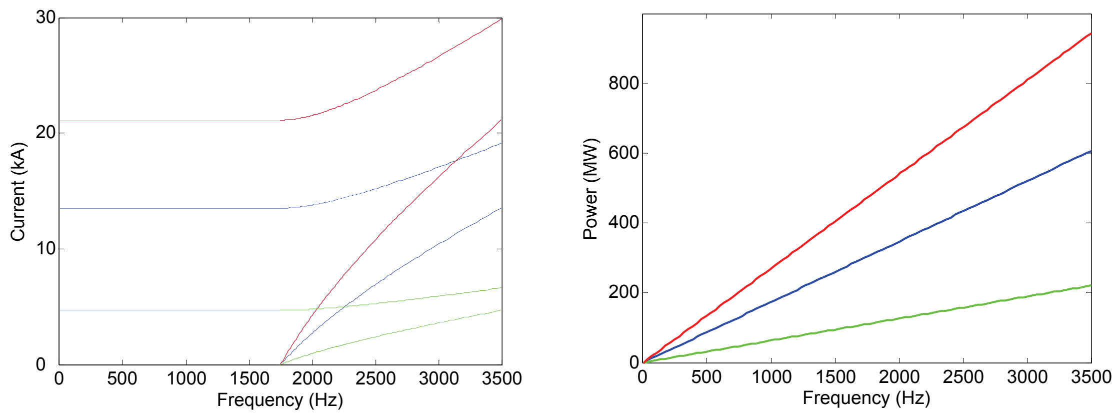

Figure C-5: Effect of varying the high voltage terminal voltage on the current and power; blue: base case; red: 1.6xbase case; green: 0.3xbase case.

The following conclusions can be made:

- Increasing the power output by increasing the size of the resonant capacitor or reducing the gain (either by reducing the voltage at the high voltage terminal or increasing the voltage at the low voltage terminal) will result in higher peak current into the converter
- Increasing the size of the inductor will result in a current approaching the average current and will reduce the peak inductor current without changing the maximum power of the converter. This will increase the cost of the low voltage terminal inductor.

Increasing the magnitude of the lower terminal voltage will result in high increase in power with only a small change in the peak current. Therefore multiple levels of converters may be advantageous in some situations.

C.2 Comparison with Parallel Resonant Converter

The resonant converter analyzed in Section 4.1 has a number of advantages over the similar parallel loaded resonant converter topology, shown in Figure C-6.

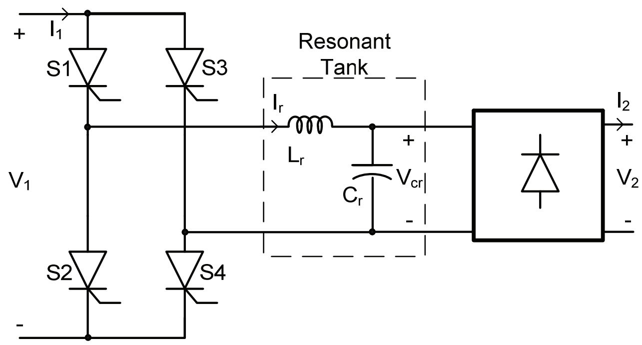

Figure C-6: Parallel Loaded Resonant Converter (PRC)

This type of converter can be used with both thyristor switches and IGBT switches (that do not have reverse blocking).

C.2.1 Parallel Resonant Converter with Thyristor Switches

When thyristor switches are used, then during discontinuous mode the resonant current and voltages are the similar to when the inductor is on the DC side of the converter. The switch characteristics are different though, and this design cannot be operated above the resonant frequency and will have in low turn-off times in the discontinuous mode. The switch voltage and current waveforms are shown in Figure C-7.

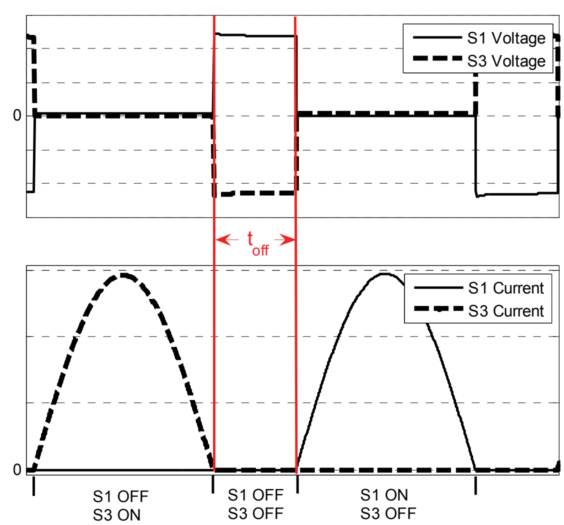

Figure C-7: Discontinuous mode switch characteristics of a Parallel Loaded Resonant Converter

After the switch S_3 turns off, the voltage across it is negative only until S_1 starts conduction, a time which is given by:

$$t_{off} = \frac{T_s - T_0}{2} \tag{C35}$$

As the switching frequency approaches the converter's resonant frequency, the turn-off time approaches zero and therefore even a Parallel Resonant Converter with ideal Thyristor switches cannot operate above the resonant frequency.

The maximum switching frequencies for different maximum turn-off times of both types of converters is shown in Figure C-8 below.

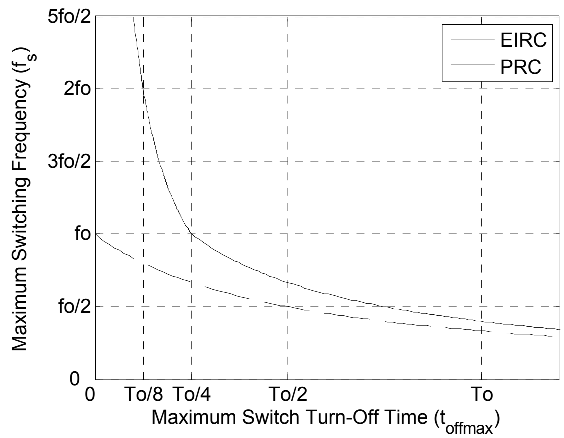

Figure C-8: Maximum switching frequency for changing switch turn-off times.

C.2.2 Parallel Resonant Converter with IGBT Switches

If IGBT switches are used then there will be no reverse blocking (unless diodes are connected in series) which will vary the output and operating ranges. The equations for the resonant converter are given by:

$$i_L(t) = I_{L0}\cos(\omega_0(t-t_0)) + \frac{V_s - V_{C0}}{Z_0}\sin(\omega_0(t-t_0)) \tag{C36}$$

$$v_C(t) = V_s - (V_s - V_{C0})\cos(\omega_0(t-t_0)) + Z_0 I_{L0}\sin(\omega_0(t-t_0)) \tag{C37}$$

In steady state conditions, the switching will occur at V_{c0}=0 and the current through the inductor is inverted every switching cycle. Therefore if the initial current is defined as I_0 then at the switching time $t_s = T_s/2$:

$$-I_0 = I_0 \cos(\omega_0 t_s) + \frac{V_1}{Z_0}\sin(\omega_0 t_s) \tag{C38}$$

$$I_0 = -\frac{V_1}{Z_0}\frac{\sin(\omega_0 t_s)}{1+\cos(\omega_0 t_s)} \tag{C39}$$

The range of I_0 is from $(0,\infty)$, depending on the switching frequency. I_0 is shown below for the range of switching frequencies $\omega_0/2 \le \omega_s \le 2\omega_0$.

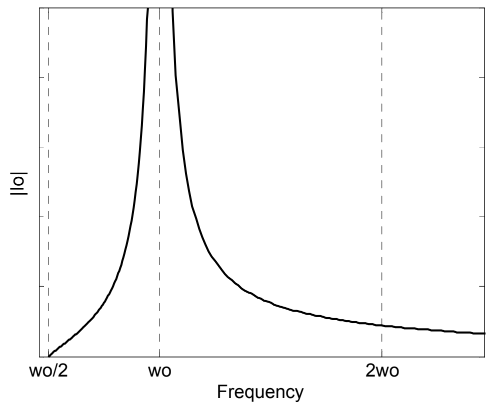

Figure C-9: I_0 for different switching frequencies.

The different modes of operation are the following:

a) Discontinuous mode: $\omega_s = \omega_0/2$
b) Continuous Mode: $\omega_0/2 < \omega_s < \omega_0$
c) Continuous Mode: $\omega_s = \omega_0$
d) Continuous Mode: $\omega_s > \omega_0$

The output voltage depending on the input voltage and frequency is shown below:

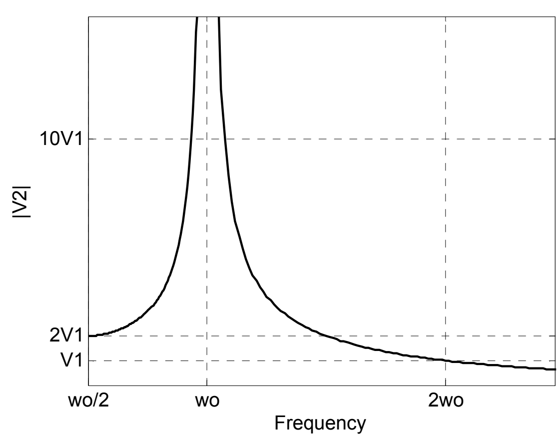

Figure C-10: Maximum V_2 for different switching frequencies.

At the maximum current then:

$$\frac{dI(t)}{dt} = -\omega_0 I_0 \sin\left(\omega_0 t_{I_{\max}}\right) + \omega_0 \frac{V_1}{Z_0}\cos\left(\omega_0 t_{I_{\max}}\right) = 0 \tag{C40}$$

$$Z_0 I_0 \sin\left(\omega_0 t_{I_{\max}}\right) - V_1 \cos\left(\omega_0 t_{I_{\max}}\right) = 0$$

Therefore at $I(t)=I_{max}$:

$$V(t) = V_1 - V_1\cos\left(\omega_0 t_{I_{\max}}\right) + Z_0 I_0 \sin\left(\omega_0 t_{I_{\max}}\right) = V_1 \tag{C41}$$

By squaring the resonant voltage and current equations at maximum current and summing:

$$I_{\max}^2 = I_0^2 + \left(\frac{V_1}{Z_0}\right)^2 \tag{C42}$$

As the frequency approaches resonant frequency then $I_0^2 >> \frac{V_1^2}{Z_0^2}$ and the maximum current will approach I_0. Also, the maximum current into the converter independent of the voltage at the secondary terminal and is therefore independent of the converter gain.

<u>Discontinuous mode</u>: $\omega_s = \omega_0/2$

As can be seen in Figure 13, when $\omega_s = \omega_0/2$ then the initial current I_0=0. Therefore

$$i(t) = \frac{V_1}{Z_0}\sin\left(\omega_0 t\right) \tag{C43}$$

$$v(t) = V_1 - V_1\cos\left(\omega_0 t\right) \tag{C44}$$

and the maximum current is V_1/Z_0 and the maximum voltage is V_1.

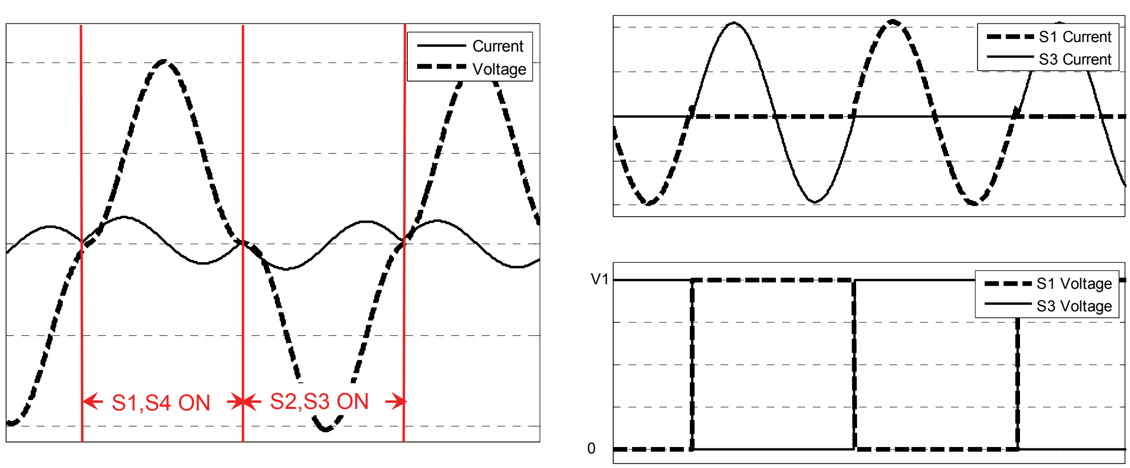

Figure C-11: Converter operation for $\omega_s = \omega_0/2$.

To calculate the maximum power, assume that the voltage at the second terminal V_2 is constant and is:

$$V_2 = \alpha V_1 \tag{C45}$$

When the voltage on the resonant capacitor is equal to V_2 then the equivalent circuit will be:

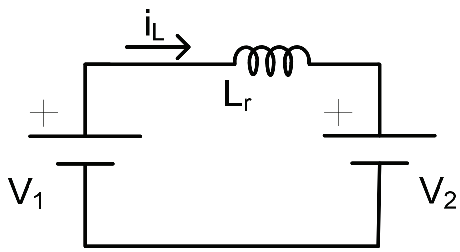

Figure C-12: Simplified circuit after V_C=V_2

If the time for V_C to reach V_2 is equal to t_B, then at time t_B:

$$I(t_B) = \frac{V_1}{Z_0}\sin(\omega_0 t_B) \tag{C46}$$

$$V(t_B) = V_2 = \alpha V_1 = V_1 - V_1\cos(\omega_0 t_B) \tag{C47}$$

Squaring both equations and summing, then:

$$i(t_B)^2 = \alpha(2-\alpha)\left(\frac{V_1}{Z_0}\right)^2 \tag{C48}$$

Using the circuit in Figure 15, then the current through the resonant inductor is given by:

$$i(t) = I(t_B) + \frac{V_1 - V_2}{L}(t - t_B) \tag{C49}$$

The zero crossing of the current occurs at time t_C, which is equal to:

$$t_C = t_B - \frac{I(t_B)L}{(1-\alpha)V_1} \tag{C50}$$

Setting t_B=0, the power transferred from the resonant converter to the second terminal during a half switching cycle is given by:

$$\begin{aligned}
P &= V_2\int_{t_B}^{t_c} i(t)dt = \alpha V_1\int_0^{t_c}\left(I(t_B) + \frac{V_1 - V_2}{L}t\right)dt = \alpha V_1 I(t_B)(t_C) + \alpha V_1\frac{(1-\alpha)V_1}{L}\frac{(t_C^2)}{2} \\
&= \alpha V_1 I(t_B)\left(-\frac{I(t_B)L}{(1-\alpha)V_1}\right) + \alpha V_1\frac{(1-\alpha)V_1}{2L}\left(\frac{I(t_B)L}{(1-\alpha)V_1}\right)^2 \\
&= \frac{1}{2}\frac{-\alpha}{(1-\alpha)}I(t_B)^2 L = \frac{1}{2}\frac{-\alpha}{(1-\alpha)}\alpha(2-\alpha)\left(\frac{V_1}{Z_0}\right)^2 L = \frac{1}{2}\frac{\alpha^2(\alpha-2)}{(1-\alpha)}\left(\frac{V_1}{Z_0}\right)^2 L
\end{aligned} \tag{C51}$$

The maximum power is shown below for the gain varying from 1 < α ≤ 2.

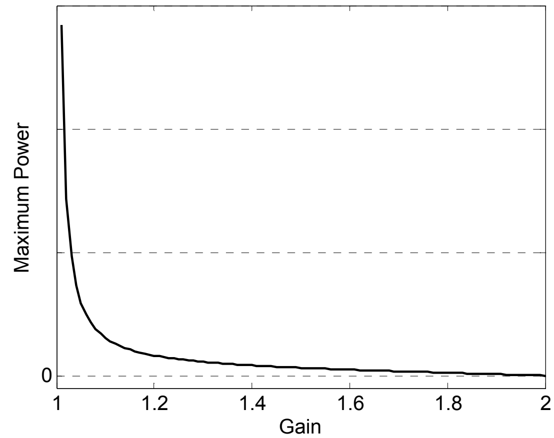

Figure C-13: Maximum power for different converter gains

As can be seen from this figure, the maximum power drops sharply as the gain is increased.

<u>Continuous Mode</u>: $\omega_s > \omega_0/2$

When the converter operates in continuous mode, the switching frequency is greater than $\omega_0/2$. The resonant current and voltage waveforms, with the current and voltage of the switches for three different continuous modes are shown below:

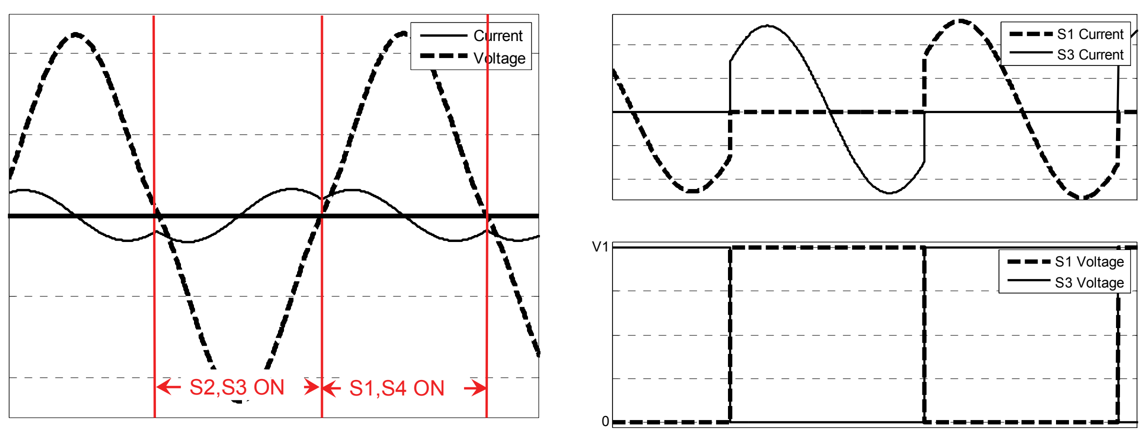

Figure C-14: Continuous Mode: $\omega_0/2 < \omega_s < \omega_0$

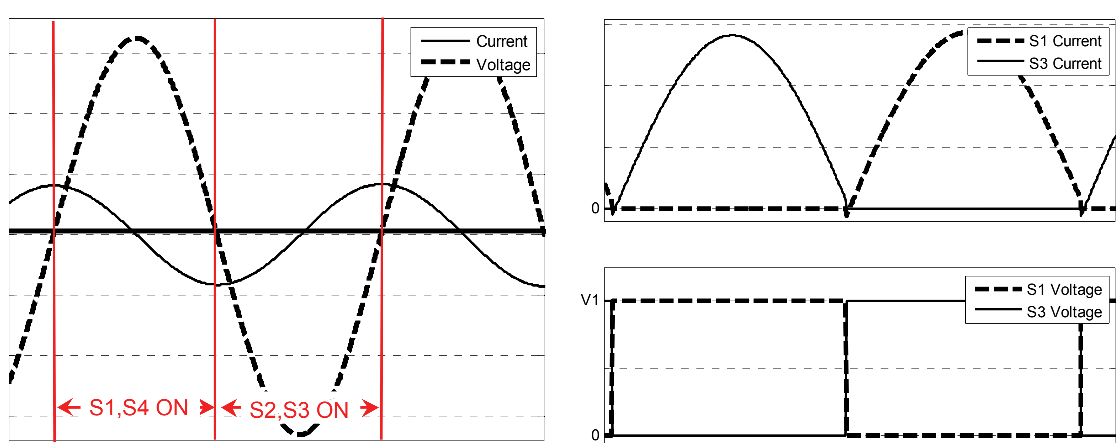

Figure C-15: Continuous Mode: $\omega_s = \omega_0$

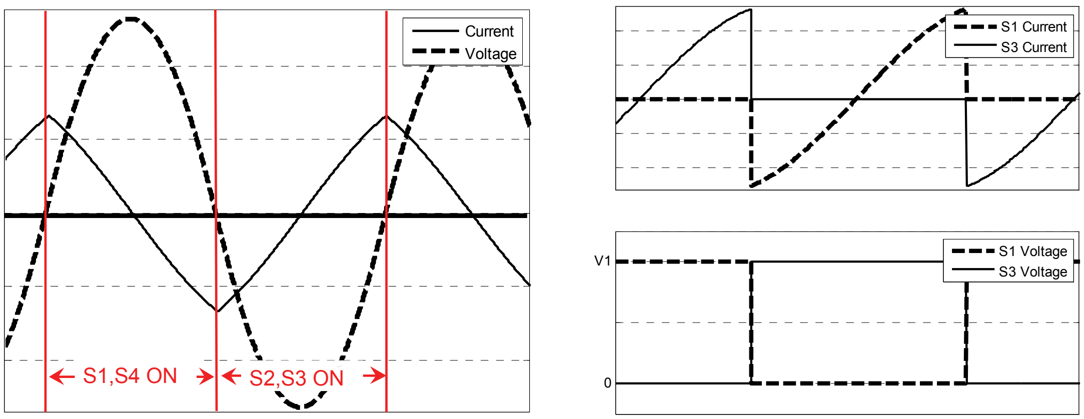

Figure C-16: Continuous Mode: $\omega_s > \omega_0$

If the time for V_C to reach V_2 is equal to t_B, then at time t_B:

$$I(t_B) = I_0 \cos(\omega_0 t_B) + \frac{V_1}{Z_0}\sin(\omega_0 t_B) \tag{C52}$$

$$V(t_B) = V_2 = \alpha V_1 = V_1 - V_1\cos(\omega_0 t_B) + Z_0 I_0 \sin(\omega_0 t_B) \tag{C53}$$

Squaring both sides and summing results in:

$$I(t_B)^2 = I_0^2 + \alpha(2-\alpha)\left(\frac{V_1}{Z_0}\right)^2 \tag{C54}$$

Similar to the discontinuous case, the power transferred from the converter to terminal 2 per cycle is:

$$\begin{aligned} P &= V_2 \int_{t_B}^{t_c} i(t)dt = \alpha V_1 \int_0^{t_c}\left(I(t_B) + \frac{V_1 - V_2}{L}t\right)dt = \frac{1}{2}\frac{-\alpha}{(1-\alpha)} I(t_B)^2 L \\ &= \frac{1}{2}\frac{\alpha}{(\alpha-1)} I_0^2 L + \frac{1}{2}\frac{\alpha^2(2-\alpha)}{(\alpha-1)}\left(\frac{V_1}{Z_0}\right)^2 L \end{aligned} \tag{C55}$$

where:

$$I_0 = -\frac{V_1}{Z_0}\frac{\sin(\omega_0 t_s)}{1+\cos(\omega_0 t_s)} \tag{C56}$$

The characteristic of the converter power for various gains and switching frequencies is shown in Figure C-17:

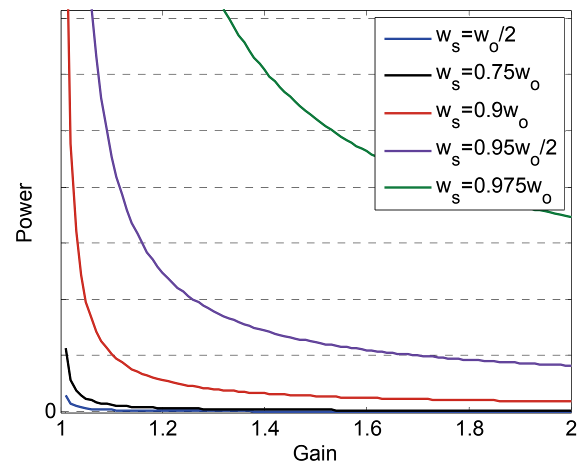

Figure C-17: Maximum power for different converter gains and switching frequencies

As can be seen in Figure C-17, as the switching frequency approaches the resonant frequency then both the maximum power and the maximum gain increase. As the switching frequency increases above the resonant frequency, the maximum power and gain will decrease as shown in Figure C-18.

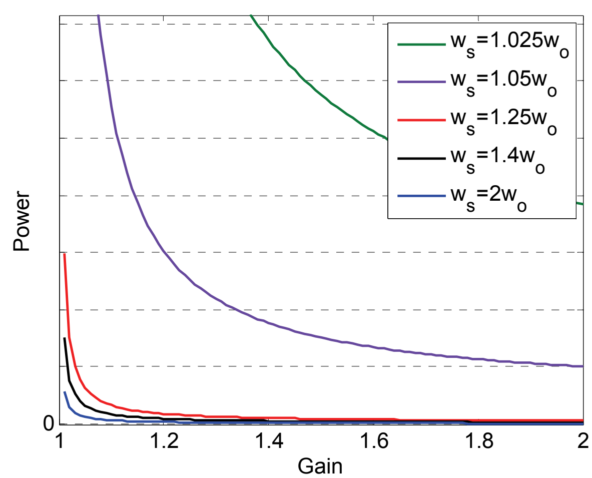

Figure C-18: Maximum power for switching frequency above resonant

Using similar ratings as the previous resonant converters where V_1=35 kV, V_2=500 kV, C_r=2.3 uF, and L_r=3.6 mF, then the peak current is much higher for an equivalent converter operating power. This is shown in Figure C-19.

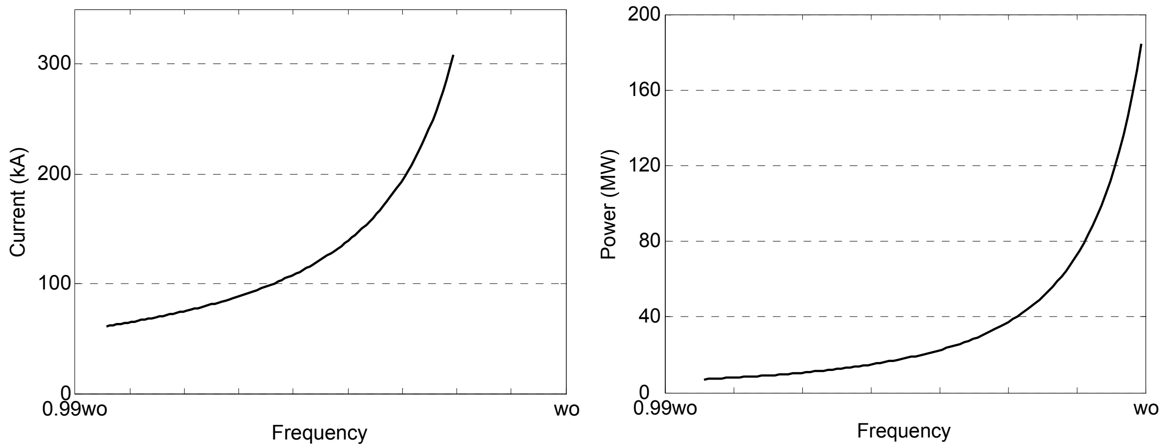

Figure C-19: Peak current and power for varying frequency with V_1=35 kV, V_2=500 kV

Overall, using IGBTs without reverse blocking has the following disadvantages:

- more limited control over the maximum gain and power of the converter,
- high switching losses when operating in the continuous mode since switching is done at non-zero voltage and current,
- high conduction losses since the current from Terminal 1 into the converter is both positive and negative,

longer settling times to achieve steady state operation for continuous operating modes.

APPENDIX D. THREE PHASE RESONANT CONVERTER

The 3-phase resonant converter operation achieves similar functionality to the single phase resonant converter, but has a smoother input current and lower peak current and current gradient, reducing on-state losses and reverse recovery losses. The 3-phase resonant converter is shown in Figure D-1.

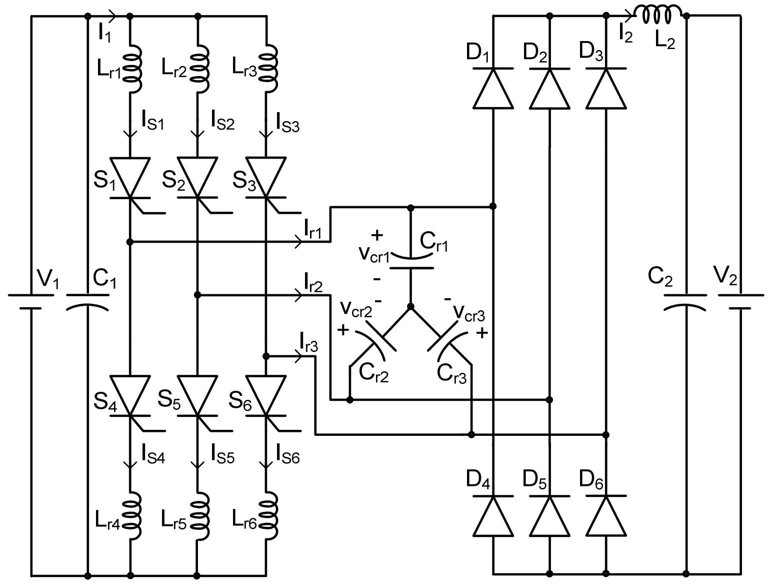

Figure D-1: 3-Phase Resonant Converter

At low switching frequencies, the converter will operate in discontinuous mode. After each switching operation, current will flow from the LV terminal, through the turned on thyristors, and charge the resonant capacitors. When the charge across the resonant capacitors is greater than the HV terminal voltage, then current will also flow into the HV side. The overall input and output current will be a series of pulses. Changing the converter power is controlled by changing the switching frequency.

The discontinuous mode operation will be analyzed in detail in Section D.1. The advantages of this converter during discontinuous mode are longer turn-off times (allowing higher frequency operation and possibly smaller component sizes) and lower reverse recovery losses (since only one thyristor turns-off after each current pulse). For a 3-phase resonant converter operating only in discontinuous mode, a better design would use only a single inductor.

As the switching frequency increases, the converter will enter continuous mode, where switching occurs before the current in the previously conducting thyristors has decreased to zero. The main advantages of this converter occur when operating in continuous mode. The input current will be close to constant, eliminating the high peak currents of the single phase resonant converter. The resonant inductors will also limit the rate-of-change of current during turn-on and turn-off, reducing the thyristor reverse recovery losses. A detailed analysis of continuous mode operation is in Section D.2.

D.1 Discontinuous Current Mode

In discontinuous mode, the current will increase from zero after every switching operation, then decrease to zero before the beginning of the next switching operation. A Matlab Simulink plot of the resonant current and voltages during discontinuous mode operation is shown in Figure D-2.

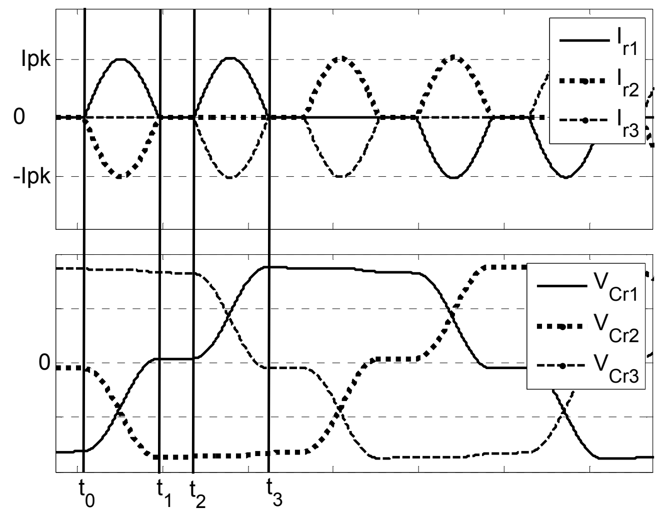

Figure D-2: Converter current and voltage during discontinuous mode operation

In Figure D-2, one-third of a switching cycle is represented as the time between t_0 and t_3, during which the voltage across the capacitor C_{r1} increases during two switching operations. Between t_0 and t_1, switches S_1 and S_5 are on, and between t_2 and t_3, switches S_1 and S_6 are on. The equivalent circuits during the two time periods are shown in Figure D-3.

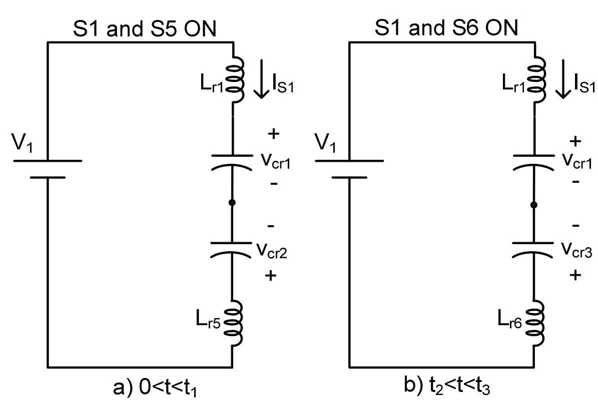

Figure D-3: Equivalent circuits during 1/3 of a cycle in discontinuous mode operation

To analyze the converter operation during discontinuous mode, the capacitor voltages are shown in Figure D-4 at the beginning of a switching cycle.

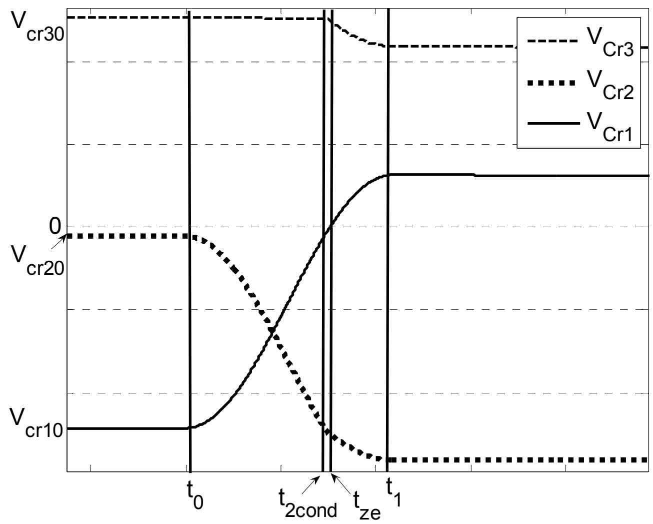

Figure D-4: Discontinuous mode voltages at the beginning of a switching cycle.

Current starts to flow into the diode bridge at time t_{2cond} and the voltage of capacitor C_{r1} equals zero at time t_{ze}. The main converter equations are:

$$I_1(t) = \frac{V_1 + \left(-V_{cr10} + V_{cr20}\right)}{2Z_0}\sin\left(\omega_0 t\right) \tag{D1}$$

$$V_{cr1}(t) - V_{cr2}(t) = V_1 - \left[V_1 + \left(-V_{cr10} + V_{cr20}\right)\right]\cos\left(\omega_0 t\right) \tag{D2}$$

for t_0=0 and where:

$$\omega_0 = \frac{1}{\sqrt{L_r C_r}} \tag{D3}$$

$$Z_0 = \sqrt{\frac{L_r}{C_r}} \tag{D4}$$

and

$$V_{cr1}(0) = V_{cr10} \quad , \quad V_{cr2}(0) = V_{cr20} \quad , \quad V_{cr3}(0) = V_{cr30}$$

(a) Time interval $0<t<t_1$

During this time interval the voltages across capacitors C_{r1} and C_{r2} (measured from the terminal connected to the thyristor switches to the common between the capacitors) are:

$$V_{cr1}(t) = \frac{1}{C_r}\int_0^t I_{S1}dt + V_{cr10} = \frac{V_1 + \left(-V_{cr10} + V_{cr20}\right)}{2}\left[1 - \cos\left(\omega_0 t\right)\right] + V_{cr10} \tag{D5}$$

$$V_{cr2}(t) = -\left[\frac{\left[V_1 + \left(-V_{cr10} + V_{cr20}\right)\right]}{2}\left[1 - \cos\left(\omega_0 t\right)\right]\right] + V_{cr20} \tag{D6}$$

Since the converter is operating in discontinuous mode, at time t_1 then $I_{S1}=0$ and therefore the final capacitor voltages will be:

$$V_{cr1}(t_1) = V_1 + V_{cr20} \tag{D7}$$

$$V_{cr2}(t_1) = -V_1 + V_{cr10} \tag{D8}$$

$$V_{cr3}(t_1) = V_{cr30} \tag{D9}$$

If the sum of V_{cr2} and V_{cr3} at time t_1 is greater then V_2 (as will be the case except during start-up), then current will flow into the diode bridge. The current flow will be equal in C_{r2} and C_{r3}, and therefore the voltage drop will be the same. The voltage drop across both capacitors at time t_1 will be:

$$V_d = V_2 - \left[-V_{cr2}(t_1) + V_{cr3}(t_1)\right] = -V_1 \tag{D10}$$

Therefore the final capacitor voltages of C_{r2} and C_{r3} at time t_1 will be given by:

$$V_{cr2}(t_1) = V_{cr10} - \frac{V_1}{2} \tag{D11}$$

$$V_{cr3}(t_1) = V_{cr30} - \frac{V_1}{2} \tag{D12}$$

(b) Time interval $t_2<t<t_3$

At time t_2, switch S_6 will turn on and current will flow through capacitors C_{r1} and C_{r3}. The inductor current and total capacitor voltage as shown in Circuit (b) of Figure D-3 is given by:

$$I_1(t) = \frac{V_{cr30} - V_{cr20} - \frac{V_1}{2}}{2Z_0}\sin(\omega_0 t) \tag{D13}$$

$$V_{cr1}(t) - V_{cr3}(t) = V_1 - \left[V_{cr30} - V_{cr20} - \frac{V_1}{2}\right]\cos(\omega_0 t) \tag{D14}$$

The individual capacitor voltages are given by:

$$V_{cr1}(t) = \frac{1}{2}\left[V_{cr30} - V_{cr20} - \frac{V_1}{2}\right]\left[1 - \cos(\omega_0 t)\right] + \left(V_1 + V_{cr20}\right) \tag{D15}$$

$$V_{cr3}(t) = \frac{1}{2}\left[V_{cr30} - V_{cr20} - \frac{V_1}{2}\right]\left[1 - \cos(\omega_0 t)\right] - \left(V_{cr30} - \frac{V_1}{2}\right) \tag{D16}$$

The final capacitor voltages of C_{r1} and C_{r3} at time t_3 when $I_L = 0$, will be:

$$V_{cr1}(t_3) = V_{cr30} + \frac{V_1}{2} \tag{D17}$$

$$V_{cr3}(t_3) = -V_{cr20} \tag{D18}$$

If the sum of V_{cr1} and V_{cr2} at time t_3 is greater then V_2, then current will flow in the diode bridge. The current flow will be equal in C_{r1} and C_{r2} and therefore the voltage drop will be the same. The voltage drop across both capacitors will be:

$$V_d = V_2 - \left(V_{cr1}(t_3) + V_{cr2}(t_3)\right) = V_2 - \left(V_{cr30} + \frac{V_1}{2} + V_{cr20} + \frac{V_1}{2}\right) = -V_1 \tag{D19}$$

Therefore the final voltages across capacitors C_{r1} and C_{r2} will be:

$$V_{cr1}(t_3) = V_{cr30} \tag{D20}$$

$$V_{cr3}(t_3) = V_{cr10} \tag{D21}$$

As can be seen, the next third of the switching cycle will have the same initial capacitor voltages only across different capacitors.

(c) Solving for steady state initial values

When I_2 starts conducting at t_{2cond}, the voltages of the different capacitors will be equal to:

$$V_{cr1}(t_{2cond}) = V_{cr20} \tag{D22}$$

$$V_{cr2}(t_{2cond}) = V_{cr10} \tag{D23}$$

$$V_{cr3}(t_{2cond}) = V_{cr30} \tag{D24}$$

Therefore at t_{2cond}:

$$V_{cr1}(t_{2cond}) = \frac{V_1 + (-V_{cr10} + V_{cr20})}{2}\left[1 - \cos(\omega_0 t_{2cond})\right] + V_{cr10} = V_{cr20} \tag{D25}$$

$$\cos(\omega_0 t_{2cond}) = \frac{V_1 - (-V_{cr10} + V_{cr20})}{V_1 + (-V_{cr10} + V_{cr20})} \tag{D26}$$

If the inductor on the high-voltage terminal is assumed to be small then the current through capacitor C_{r1} is divided evenly through capacitors C_{r2} and C_{r3}. This is shown in Figure D-5.

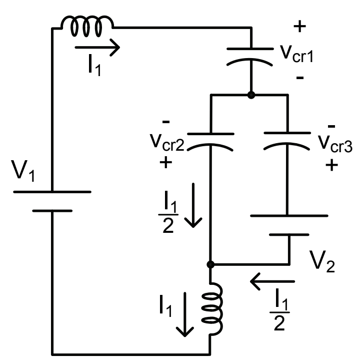

Figure D-5: Equivalent circuits when current flows into the high voltage side.

Therefore the capacitor voltages after the high voltage terminal is conducting can be evaluated as:

$$V_{cr1}(t) = \frac{1}{C_r}\int_{t_{2cond}}^{t} I_1 dt = \frac{V_1 + (-V_{cr10} + V_{cr20})}{2}\left[\cos(\omega_0 t_{2cond}) - \cos(\omega_0 t)\right] + \frac{I_{t_{2cond}}}{C_r}(t - t_{2cond}) + V_{cr20} \quad \text{(D27)}$$

$$V_{cr2}(t) = -\frac{\left[V_1 + (-V_{cr10} + V_{cr20})\right]}{4}\left[\cos(\omega_0 t_{2cond}) - \cos(\omega_0 t)\right] - \frac{I_{t_{2cond}}}{2C_r}(t - t_{2cond}) + V_{cr10} \quad \text{(D28)}$$

$$V_{cr3}(t) = -\frac{\left[V_1 + (-V_{cr10} + V_{cr20})\right]}{4}\left[\cos(\omega_0 t_{2cond}) - \cos(\omega_0 t)\right] - \frac{I_{t_{2cond}}}{2C_r}(t - t_{2cond}) + V_{cr30} \quad \text{(D29)}$$

At time t_{ze} the voltage across capacitor C_{r1} will cross zero and the voltage V_2 will be evenly divided across capacitors C_{r2} and C_{r3} and therefore:

$$V_{cr2}(t_{ze}) = \frac{V_{cr20}}{2} + V_{cr10} = -\frac{V_2}{2} \quad \text{(D30)}$$

Using these results, the voltage V_{cr20} can be evaluated as:

$$-V_{cr20} = V_2 + 2V_{cr10} \quad \text{(D31)}$$

As the converter operation approaches steady state, the positive and negative peak voltages will be equal. Therefore:

$$-V_{cr10} + \frac{V_1}{2} = V_{cr30} = V_2 + V_{cr10} \quad \text{(D32)}$$

$$V_{cr10} = -\frac{V_2}{2} + \frac{V_1}{4} \quad \text{(D33)}$$

and therefore:

$$V_{cr20} = -\frac{V_1}{2} \quad \text{(D34)}$$

D.1.1 Energy Transfer and Peak Input Current

Using the switching analysis in Section D.1, the converter power can be obtained using the energy transferred to the HV terminal during each switching cycle. Using 1/3 of the switching cycle, then during time t_0 to t_1 the energy transferred is the difference in capacitor energy depending on whether current flows to the diode bridge. This energy is given by:

$$E_{01} = \frac{1}{2}C_r\left(V_1 - V_{cr10}\right)^2 - \frac{1}{2}C_r\left(\frac{V_1}{2} - V_{cr10}\right)^2 + \frac{1}{2}C_r V_{cr30}{}^2 - \frac{1}{2}C_r\left(V_{cr30} - \frac{V_1}{2}\right)^2$$
$$= \frac{1}{2}C_r\left[\left(\frac{V_1}{2}\right)^2 - V_1 V_{cr10} + V_1 V_{cr30}\right] \tag{D35}$$

The energy transferred between time t_2 to t_3 is:

$$E_{23} = \frac{1}{2}C_r\left(V_{cr30} + \frac{V_1}{2}\right)^2 - \frac{1}{2}C_r V_{cr30}{}^2 + \frac{1}{2}C_r\left(-V_{cr10} + \frac{V_1}{2}\right)^2 - \frac{1}{2}C_r V_{cr10}{}^2$$
$$= \frac{1}{2}C_r\left[\left(\frac{V_1}{2}\right)^2 - V_1 V_{cr10} + V_1 V_{cr30}\right] \tag{D36}$$

Therefore the total energy transferred during 1/3 of a switching cycle is:

$$E = \frac{1}{2}C_r\left(V_1^2 - 2V_1 V_{cr10} + 2V_1 V_{cr30}\right) = \frac{1}{2}C\left(V_1^2 + 2V_1 V_2\right) \tag{D37}$$

The converter power is then:

$$P = \frac{1}{2}C\left(V_1^2 + 2V_1 V_2\right) \cdot 3 \cdot f_s \tag{D38}$$

The maximum input current in discontinuous mode is the maximum current through the inductors derived in Section D.1. Therefore during time t_0 to t_1 the maximum current is:

$$I_1(t) = \frac{V_1 + \left(-V_{cr10} + V_{cr20}\right)}{2Z_0} \tag{D39}$$

During time t_2 to t_3 the maximum input current is:

$$I_1(t) = \frac{V_{cr30} - V_{cr20} - \frac{V_1}{2}}{2Z_0} \tag{D40}$$

In steady state, the maximum current will be:

$$I_{pk} = \frac{\frac{V_2}{2} + \frac{V_1}{4}}{2Z_0} \tag{D41}$$

Therefore increasing the size of the inductor will reduce the current peak and increasing capacitor size will increase the current peak.

The voltage increase on the capacitor for each current pulse on the HV side can be obtained using (D38). Since there will be 6 current pulses per cycle, then the maximum voltage variation per pulse (at low power levels) is:

$$\Delta V_2 = -1 + \frac{1}{V_2}\sqrt{\frac{C_r}{2C_2}\left(V_1^2 + 2V_1V_2\right) - V_2^2} \tag{D42}$$

where C_2 is the capacitor on the HV side and ΔV_2 is in pu. When designing for a set voltage variation per current pulse, then size of the HV side capacitor will be given by:

$$C_2 = \frac{C_r\left(V_1^2 + 2V_1V_2\right)}{2V_2^2\Delta V_2\left(2 + \Delta V_2\right)} \tag{D43}$$

Similarly, the input DC capacitor will be:

$$C_1 = \frac{C_r\left(V_1^2 + 2V_1V_2\right)}{2V_1^2\Delta V_1\left(2 + \Delta V_1\right)} \tag{D44}$$

D.1.2 Discontinuous Mode Switch Voltage

The switch voltages and currents are shown in Figure D-6.

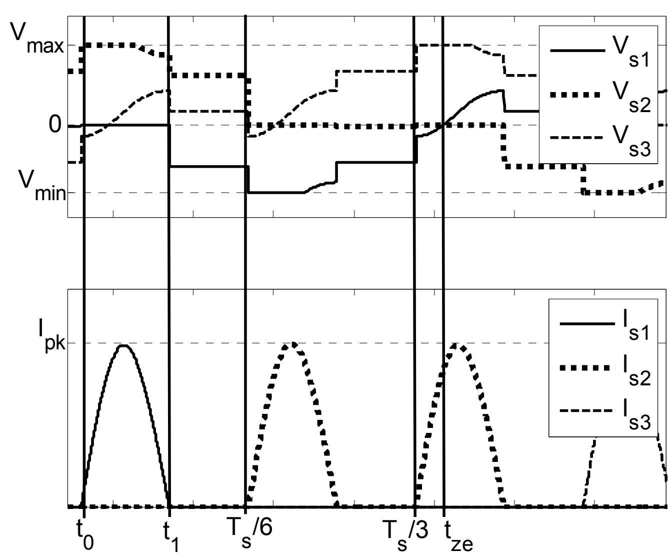

Figure D-6: Switch voltages and currents during discontinuous mode operation

The minimum voltage across a thyristor switch occurs after the next switching action after it has been switched off. For the case where switch S_1 is off and switch S_2 and S_6 are on is shown in Figure D-7.

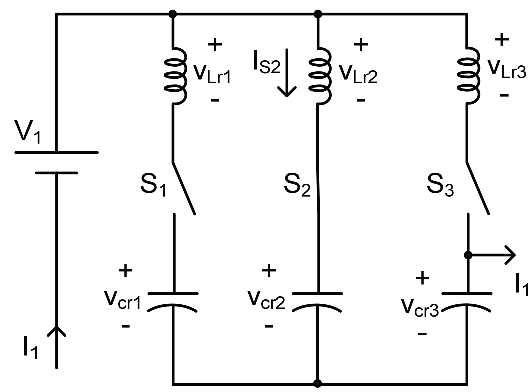

Figure D-7: Partial converter circuit after S2 switches ON.

The voltage across the switch S_1 will be equal to:

$$V_{s1}(t) = \left(L_r \frac{dI_{Lr}}{dt} + V_{cr2}\right) - V_{cr1} = \left(\frac{V_1 + V_{cr10} + V_{cr20}}{2}\right) - \left(V_2 + V_{cr10}\right)$$
$$= -V_2 - \frac{V_{cr10}}{2} + \frac{V_1}{2} + \frac{V_{cr20}}{2} \tag{D45}$$

During steady state conditions the minimum voltage across S_1 will be equal to:

$$V_{sw\_\min} = -\frac{3}{4}V_2 + \frac{V_1}{8} \tag{D46}$$

During the next switching operation, S_2 and S_4 will be on and S_6 will be off and the maximum voltage will be across switch S_3 and is given by:

$$V_{s3}(t) = \left(L_r \frac{dI_{Lr}}{dt} + V_{cr2}\right) - V_{cr3} = \frac{3V_1}{2} - \frac{V_{cr10}}{2} + \frac{3V_{cr20}}{2} + V_{cr30} \tag{D47}$$

Under steady state conditions the maximum switch voltage will be:

$$V_{sw\_\max} = \frac{3}{4}V_2 + \frac{7}{8}V_1 \tag{D48}$$

The rate of change of current is limited by the series inductances, however parallel RC snubbers will normally be required to limit the rate of change of voltage. Using Figure D-6, the switch turn-off time will be equal to:

$$t_{turnoff} = \left(\frac{T_s}{6} - t_1\right) + \left(\frac{T_s}{6}\right) + \left(t_{ze}\right) \tag{D49}$$

The time for the current to cross zero after a switching operation can be found using the inductor current equation from Section D.1. Therefore:

$$I_1(t_1) = \frac{V_1 + \left(-V_{cr10} + V_{cr20}\right)}{Z_0} \sin\left(\omega_0 t_1\right) = 0$$

$$t_1 = \frac{1}{2 f_0} \tag{D50}$$

The voltage across switch S_1 between $T_s/3 < t < t_{ze}$ is equal to:

$$\begin{aligned} V_{s1}(t) &= \left(L_r \frac{dI_{Lr}}{dt} + V_{cr2}(t)\right) - V_{cr1}(t) \\ &= \frac{\left[V_1 + \left(-V_{cr10} + V_{cr20}\right)\right]}{2}\left[2 - \cos(\omega_0 t)\right] - V_{cr30} + \frac{3}{2}V_1 + 2V_{cr20} \end{aligned} \tag{D51}$$

At time t_{ze}, $V_{s1} = 0$ and therefore:

$$\cos\left(\omega_0 t_{ze}\right) = \frac{-2V_{cr10} - 2V_{cr30} + 5V_1 + 6V_{cr20}}{V_1 + \left(-V_{cr10} + V_{cr20}\right)}$$

$$t_{ze} = \frac{1}{\omega_0} \cos^{-1}\left(\frac{V_1}{V_2 + \frac{V_1}{2}}\right) \tag{D52}$$

Therefore the total turn-off time in discontinuous mode is:

$$t_{turnoff} = \frac{T_s}{3} - \frac{1}{2 f_0} + \frac{1}{\omega_0} \cos^{-1}\left(\frac{V_1}{V_2 + \frac{V_1}{2}}\right) \tag{D53}$$

D.2 Continuous Mode Operation

Continuous mode operation occurs when the input current does not decrease to zero before the next switching operation, which will occur when:

$$f_s > \frac{f_0}{3} \tag{D54}$$

It should be noted that the individual current through the thyristor switches will decrease to zero each cycle, even though the input current is always greater than zero. The continuous mode operation can be analyzed by considering 1/6$^{\text{th}}$ of a cycle, shown in Figure D-8.

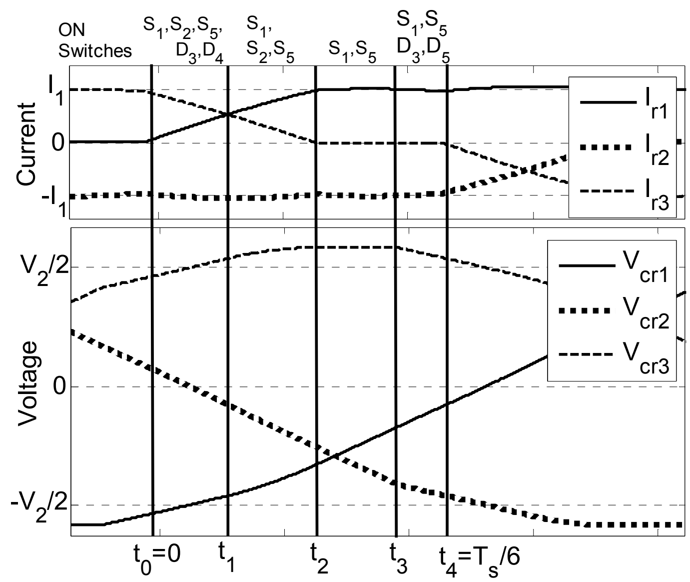

Figure D-8: Current and voltage during 1/6th of a cycle in continuous mode operation.

The circuits for each of the four time sections in Figure D-8 are shown in Figure D-9.

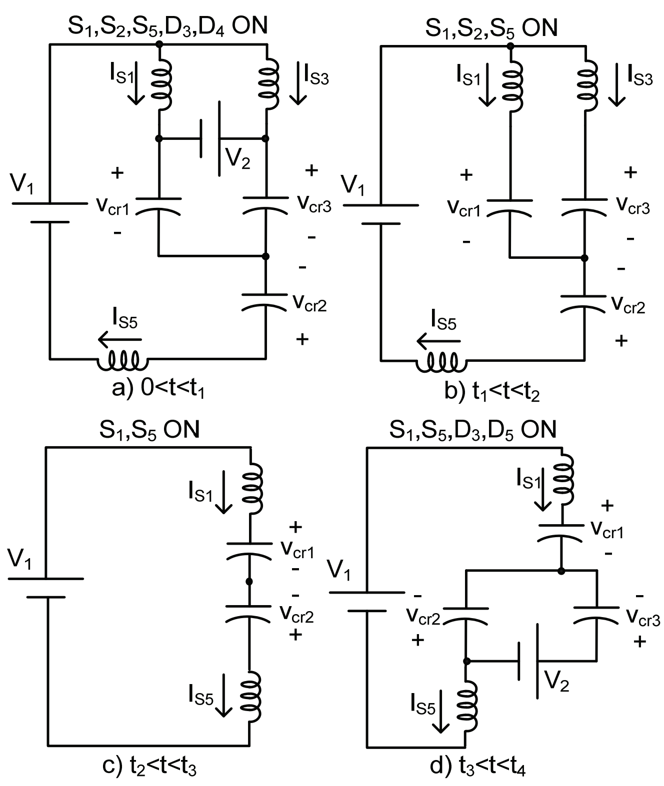

Figure D-9: Equivalent circuits for 1/6th of a cycle in continuous mode operation.

(a) Time interval $0<t<t_1$

For circuit (a) in Figure D-9 the current I_{S5} will be equal to the input current I_1. When $t<t_1$ current will flow into the high voltage side of the converter and therefore the voltage across

V_{cr1} and V_{cr3} will be equal to V_2 and the current through both capacitors will be equal to half the input current. Using circuit equations, the voltage across the V_{cr2} and L_5 for both circuits (a) and (b) will be constant and equal to:

$$V_{Lr5} - V_{cr3} = \frac{2}{3}V_1 \tag{D55}$$

Therefore the input current I_1 will be given by:

$$I_1(t) = I_{S5}(t) = I_1(0)\cos(\omega_0 t) + \frac{\frac{2}{3}V_1 + V_{cr2}(0)}{Z_0}\sin(\omega_0 t) \tag{D56}$$

where $I_1(0)$ and $V_{cr2}(0)$ are the current from the LV terminal and voltage across C_{r2} at time t_0=0 (Figure D-8). Since the currents through V_{cr1} and V_{cr2} will be equal to half the input current, then the capacitor voltages will be given by:

$$-V_{cr2}(t) = \frac{1}{C_r}\int_0^t I_1(t)dt = I_0 Z_0 \sin(\omega_0 t) + \left(\frac{2}{3}V_1 + V_{cr2}(0)\right)(1-\cos(\omega_0 t)) - V_{cr2}(0) \tag{D57}$$

$$V_{cr3}(t) = \frac{1}{C_r}\int_0^t \frac{I_1(t)}{2}dt + V_{cr3}(0) = \frac{I_0 Z_0}{2}\sin(\omega_0 t) + \frac{\left(\frac{2}{3}V_1 + V_{cr2}(0)\right)}{2}(1-\cos(\omega_0 t)) + V_{cr3}(0) \tag{D58}$$

$$V_{cr1}(t) = \frac{I_0 Z_0}{2}\sin(\omega_0 t) + \frac{\left(\frac{2}{3}V_1 + V_{cr2}(0)\right)}{2}(1-\cos(\omega_0 t)) - V_{cr2}(0) \tag{D59}$$

The currents through switches S_1 and S_3 will be:

$$\begin{aligned} I_{S3} &= \frac{1}{L_r}\int_0^t \left(\frac{1}{3}V_1 - V_{cr3}(t)\right)dt + I_1(0) \\ &= \frac{-2V_{cr3}(0) - V_{cr2}(0)}{2L}t + \frac{I_1(0)}{2} + \frac{I_1(0)}{2}\cos(\omega_0 t) + \frac{\frac{2}{3}V_1 + V_{cr2}(0)}{Z_0}\sin(\omega_0 t) \\ &= \frac{-V_2}{2L}t + \frac{I_1(0)}{2} + \frac{I_1(0)}{2}\cos(\omega_0 t) + \frac{\frac{2}{3}V_1 + V_{cr2}(0)}{Z_0}\sin(\omega_0 t) \end{aligned} \tag{D60}$$

$$I_{S1} = \frac{V_2}{2L_r}t - \frac{I_1(0)}{2} + \frac{I_1(0)}{2}\cos(\omega_0 t) + \frac{\frac{2}{3}V_1 + V_{cr2}(0)}{Z_0}\sin(\omega_0 t) \tag{D61}$$

Since the current through the capacitors will be equal when current is flowing to the high voltage side of the converter, then the current I_2 will be:

$$I_2 = \frac{I_{S3} - I_{S1}}{2} = \frac{-V_2}{2L_r}t + \frac{I_1(0)}{2} \tag{D62}$$

The converter will stop transferring power to the high voltage side when the current I_2 falls to zero, which will occur at time:

$$t_1 = \frac{I_1(0)L_r}{V_2} \tag{D63}$$

When the times t_1 and t_2 are small, then the inductor currents can be approximated as:

$$I_{S5} = I_1 \tag{D64}$$

$$I_{S3} = -\frac{V_2}{2L_r}t + I_1 \tag{D65}$$

$$I_{S1} = \frac{V_2}{2L_r}t \tag{D66}$$

where I_1 represents a constant input current. This assumption is inaccurate at the border between continuous and discontinuous operation and at very high frequencies.

Since for $t<t_1$ the current through capacitors C_{r1} and C_{r3} are equal to half the input current then the capacitor voltages at t_1 will be:

$$V_{cr2}(t_1) = \frac{1}{C_r}\int_0^t I_{S5}dt + V_{cr2}(0) = -\frac{I_1}{C_r}t_1 + V_{cr2}(0) = -\frac{I_1^2 L_r}{C_r V_2} + V_{cr2}(0) \tag{D67}$$

$$V_{cr3}(t_1) = \frac{1}{C_r}\int_0^t \frac{I_{S5}}{2}dt + V_{cr3}(0) = \frac{I_1^2 L_r}{2C_r V_2} + V_{cr3}(0) \tag{D68}$$

$$V_{cr1}(t_1) = \frac{I_1^2 L_r}{2C_r V_2} + V_{cr1}(0) \tag{D69}$$

With an input current of I_1, the time for the current I_{L3} to fall to zero will be:

$$t_2 = \frac{2I_1 L_r}{V_2} \tag{D70}$$

(b) Time interval $t_1<t<t_2$

Since for $t_1<t<t_2$ the capacitor currents I_{cr1} and I_{cr3} will be equal to the inductor currents I_{L1} and I_{L3}, then the voltages of the converter capacitors at time t_2 will be:

$$V_{cr2}(t_2)=\frac{1}{C_r}\int_{t_1}^{t_2} I_{Lr5}dt+V_{cr}(t_1)=-\frac{I_1}{C_r}(t_2-t_1)+V_{cr2}(0)=-\frac{2I_1^2L_r}{C_rV_2}+V_{cr2}(0) \tag{D71}$$

$$\begin{aligned}V_{cr3}(t_2)&=\frac{1}{C_r}\int_{t_1}^{t_2} I_{Lr3}dt+V_{cr}(t_1)=\frac{1}{C_r}\int_{t_1}^{t_2}\left(-\frac{V_2}{2L_r}t+\frac{I_1}{2}\right)dt+\frac{I_1^2L_r}{2C_rV_2}+V_{cr3}(0)\\&=-\frac{V_2}{4L_rC_r}\left(\frac{I_1L_r}{V_2}\right)^2+\frac{I_1}{2}\left(\frac{I_1L_r}{V_2}\right)-\frac{V_2}{4L_rC_r}\left(\frac{I_1L}{V_2}\right)^2+\frac{I_1^2L_r}{2C_rV_2}+V_{cr3}(0)\\&=\frac{3}{4}\frac{I_1^2L_r}{C_rV_2}+V_{cr3}(0)\end{aligned} \tag{D72}$$

$$V_{cr1}(t_2)=\frac{5}{4}\frac{I_1^2L_r}{C_rV_2}+V_{cr1}(0) \tag{D73}$$

(c) Time interval $t_2<t<t_3$

After the current I_{S3} falls to zero, the current through capacitors C_{r1} and C_{r3} will be equal. Therefore the capacitors' voltages at time t_3 will be given by:

$$V_{cr2}(t_3)=-\frac{I_1}{C_r}(t_3-t_2)+V_{cr2}(t_2)=-\frac{I_1}{C_r}(t_3-t_2)-\frac{2I_1^2L_r}{C_rV_2}+V_{cr2}(0) \tag{D74}$$

$$V_{cr1}(t_3)=\frac{I_1}{C_r}(t_3-t_2)+V_{cr1}(t_2)=\frac{I_1}{C_r}(t_3-t_2)+\frac{5}{4}\frac{I_1^2L_r}{C_rV_2}+V_{cr1}(0) \tag{D75}$$

(d) Time interval $t_3<t<t_4$

When $t_3<t<t_4$ then current will be flowing into the high voltage terminal of the converter equal to half the input current. Both capacitors will have half the input current flowing through them and therefore the final capacitor voltages will be:

$$\begin{aligned}V_{cr2}(t_4)&=-V_{cr3}(0)=-\frac{I_1}{2C_r}(t_4-t_3)+V_{cr2}(t_3)\\&=-\frac{I_1}{2C_r}(t_4-t_3)-\frac{I_1}{C_r}(t_3-t_2)-\frac{2I_1^2L_r}{C_rV_2}+V_{cr2}(0)\end{aligned} \tag{D76}$$

$$V_{cr1}(t_4)=-V_{cr2}(0)=\frac{I_1}{C_r}(t_4-t_3)+\frac{I_1}{C_r}(t_3-t_2)+\frac{5}{4}\frac{I_1^2L_r}{C_rV_2}+V_{cr1}(0) \tag{D77}$$

$$V_{cr3}(t_4)=-V_{cr1}(0)=-\frac{I_1}{2C_r}(t_4-t_3)+\frac{3}{4}\frac{I_1^2L_r}{C_rV_2}+V_{cr3}(0) \tag{D78}$$

Using the capacitor voltage equations, the initial voltages across the converter capacitors can be obtained:

$$-V_{cr2}(0)-V_{cr1}(0)=\frac{I_1}{C_r}t_4-\frac{I_1}{C_r}\left(\frac{2I_1L_r}{V_2}\right)+\frac{5}{4}\frac{I_1^2L_r}{C_rV_2} \tag{D79}$$

$$V_{cr3}(0)=\frac{I_1}{C_r}t_4-\frac{3}{4}\frac{I_1^2L_r}{C_rV_2} \tag{D80}$$

$$V_{cr1}(0)=-(V_2-V_{cr3}(0))=\frac{I_1}{C_r}t_4-\frac{3}{4}\frac{I_1^2L_r}{C_rV_2}-V_2 \tag{D81}$$

$$V_{cr2}(0)=-V_{cr1}-V_{cr3}=V_2-\frac{2I_1}{C_r}t_4+\frac{3}{2}\frac{I_1^2L_r}{C_rV_2} \tag{D82}$$

The time (t_4-t_3) will be equal to:

$$-V_{cr1}(0)-V_{cr3}(0)=V_{cr2}(0)=-\frac{I_1}{2C_r}(t_4-t_3)+\frac{3}{4}\frac{I_1^2L}{C_rV_2}=V_2-\frac{2I_1}{C_r}t_4+\frac{3}{2}\frac{I_1^2L_r}{C_rV_2}$$

$$(t_4-t_3)=-\frac{2V_2C_r}{I_1}+4t_4-\frac{3}{2}\frac{I_1L_r}{V_2} \tag{D83}$$

Therefore:

$$t_3=\frac{2V_2C_r}{I_1}-3t_4+\frac{3}{2}\frac{I_1L_r}{V_2} \tag{D84}$$

The peak capacitor voltage occurs at time t_2 when the voltage across C_{r3} is given by:

$$V_{cr3}(t_2)=\frac{3}{4}\frac{I_1^2L_r}{C_rV_2}+V_{cr3}(0)=\frac{I_1}{C_r}t_4 \tag{D85}$$

The current into the converter can be obtained by assuming zero losses and setting the power into the converter equal to the power out. Using the circuits from Figure D-9, then current only flows out of the converter for $0<t<t_1$ and $t_3<t<t_4$ and therefore during 1/6th of a switching cycle:

$$\begin{aligned} I_1V_1t_4 &= V_2\int_0^{t_1}\left(-\frac{V_2}{2L}t+\frac{I_1}{2}\right)dt+\frac{V_2I_1}{2}(t_4-t_3) \\ &= V_2\left(-\frac{V_2}{4L}\left(\frac{I_1L}{V_2}\right)^2+\frac{I_1}{2}\left(\frac{I_1L}{V_2}\right)\right)+\frac{V_2I_1}{2}(t_4-t_3) \end{aligned} \tag{D86}$$

$$I_1=\frac{4V_1t_4}{L_r}-\frac{2V_2}{L_r}(t_4-t_3) \tag{D87}$$

Using the time (t_4-t_3) from (D83) then:

$$I_1=\frac{4V_1t_4}{L_r}-\frac{2V_2}{L_r}\left(-\frac{2V_2C_r}{I_1}+4t_4-\frac{3}{2}\frac{I_1L_r}{V_2}\right)$$

$$I_1^2 + \frac{2t_4}{L_r}(V_1 - 2V_2)I_1 + \frac{2V_2^2 C_r}{L_r} = 0$$

$$I_1 = \frac{1}{6 f_s L_r}(2V_2 - V_1) - \sqrt{\left(\frac{1}{6 f_s L_r}(V_1 - 2V_2)\right)^2 - \frac{2V_2^2 C_r}{L_r}} \tag{D88}$$

The total converter power in continuous mode operation will be given by:

$$P_{conv} = V_1 I_1 = V_1 \left[\frac{1}{6 f_s L_r}(2V_2 - V_1) - \sqrt{\left(\frac{1}{6 f_s L_r}(V_1 - 2V_2)\right)^2 - \frac{2V_2^2 C_r}{L_r}}\right] \tag{D89}$$

D.2.1 Continuous Mode Switch Voltage and Current

The switching characteristics for continuous mode operation are shown in Figure D-10.

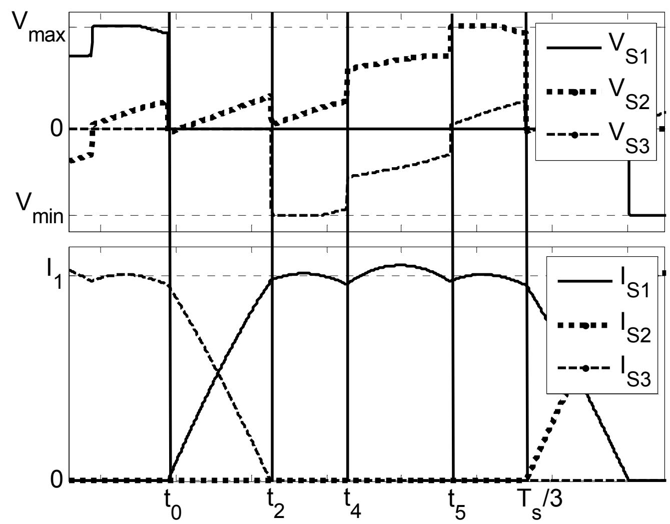

Figure D-10: Switch voltages and currents during continuous mode operation.

In Figure D-10, switch S_1 turns on at time t_0 and switch S_3 turns off at time t_1. The minimum switch voltage occurs after the switch S_3 turns off. The maximum switch voltage will occur across S_2 at time t_5 when S_1 is on and S_5 turns off.

Using a constant input current then the magnitudes of the maximum switch voltage and minimum switch voltage will be equal and will be given by:

$$V_{\min} = V_{cr2}(t) + V_{Lr2}(t) - V_{cr1} = \frac{1}{2}\frac{I_1^2 L_r}{C_r V_2} + \frac{I_1}{C_r}t_4 - V_2 + 0 - \frac{I_1}{C_r}t_4 = \frac{1}{2}\frac{I_1^2 L_r}{C_r V_2} - V_2 \tag{D90}$$

The maximum voltage will approach V_2 at low converter power levels. The total turn-off time will be from t_3 to t_5 in Figure D-10, which is 1/6^th^ of the switching time.

In continuous mode operation, the slope of the switch current can be estimated as $V_2/2L$. At high switching frequencies switch S_1 may be turned on before the current I_{S3} has gone to zero (in Fig. 7, if $T_s/3 \leq t_2$) and therefore the average current into the converter will be greater than the peak switch current. The maximum switch current can then be estimated using (D65) and a current rise time of $T_s/3$, so that:

$$I_{peakcont} = \frac{V_2}{2L_r}\frac{T_s}{3} \tag{D91}$$

Operating in this region will reduce switching losses (since the peak switch current does not increase at high powers); however the ability of the converter to operate in this region will depend on the thyristor turn-off time.